THESE DE DOCTORAT DE

L'ÉCOLE CENTRALE DE NANTES

ECOLE DOCTORALE N° 602
Sciences pour l'Ingénieur
Spécialité : Génie Civil

Par
Yuliang ZOU

Modelling of the dynamic effects in capillary pressure in coupling with deformation on the desiccation of porous materials

Thèse présentée et soutenue à NANTES, le 10/12/2020
Unité de recherche : UMR 6183, Institut de Recherche en Génie Civil et Mécanique (GeM)

Rapporteurs avant soutenance :

Didier LASSEUX	Directeur de Recherche, CNRS, Université Bordeaux, Talence
Christelle MIQUEU	Maître de Conférences HDR, Université de Pau et des Pays de L'Adour, Anglet

Composition du Jury :

Président :	Gawtum NAMAH	Professeur des Universités, Université de Franche-Comté, Besançon
Examinateurs :	Matthieu VANDAMME	Maître de Conférences HDR, Ecole des Ponts ParisTech, Champs-sur-Marne
Dir. de thèse :	Frédéric GRONDIN	Professeur des Universités, Ecole Centrale de Nantes
Co-dir. de thèse :	Mazen SAAD	Professeur des Universités, Ecole Centrale de Nantes

Acknowledgements

I would like to express my sincere gratitude to Prof. GRONDIN and Prof. SAAD. Without their guidance, it is impossible for me to finish my Ph.D. study. Their suggestions have greatly shaped my view on research work and life. Prof. GRONDIN. is patient and offers me endless support and encouragement in these three years. Once I make a little progress or have some new results, he never miss the opportunity to praise me. Indeed, his encouragement gives me confidence and makes me full of motivation. In addition, his optimism and rigorous attitude toward life and academic research impressed me most and will benefit me a lot for a lifetime. My co-supervisor Prof. SAAD also provides me with constructive advice and scientific support. I am very grateful for spending time on my model improvement and article correction.I would also like to appreciate the jury committee members,Prof. MIQUEU, LASSEUX, VANDAMME and NAMAH for providing insightful comments and advice to refine my thesis.

Then thanks a lot all my colleagues of GeM lab. Thanks to them, I have the chance to work in a very good atmosphere. Many thanks to ZHU Ran, WANG Huang, YIN Kexin, LIU Xiaodong, WU Shaoqi, Aliénor POUYANNE, Faten SOUAYFAN and Quentain ROUSSEAU. Thank them all for their enthusiasm and help.

I also appreciate the continuous support and understanding of my girlfriend. It's hard to remember how many times back and forth between Nantes and Lille. But I will never forget our story happened in these two cities. You said that you can see the future in my eyes. In fact, you are all in my eyes.

Finally and most importantly, I would like to express my deepest gratitude to my father and mother. Thanks a lot for their selfless love. Their love lights up my way forward. My father is a man who values education very much. He is the best mentor in my life. I am very proud to be able to meet his expectation.

Abstract

The durability of infrastructure made of porous materials such as soil, sand and cement-based materials is closely related to the environmental conditions. Most of the mechanisms of deterioration are governed by moisture state in porous materials. Indeed, the moisture state determines the distribution of capillary pressure which is an important driving force for solid deformation and could increase cracking risk. However, most of fluid-solid interaction models used to predict moisture transport and solid deformation have ignored the existing physical phenomenon dynamic effects on capillary pressure. This thesis aims to refine the fluid-solid interaction model with the consideration of this dynamic capillarity effect. Three dynamic models corresponding to various types of porous materials have been developed. The first model is available for porous materials with relative high permeability such as sand and soil. The second model is used for mature cement-based materials with low permeability. The third model is developed for hardening cement-based materials exposed to extremely low relative humidity condition. Each dynamic model and corresponding non-dynamic model have been implemented to simulate documented drying (drainage) experiments for sand, mature cement paste and hardening concrete, respectively. Compared with experimental data, the numerical simulations show that modeling with dynamic effects gives better results than non-dynamic modeling. All comparisons and investigations enhanced the necessity of considering dynamic capillarity effect to predict the moisture transport and solid deformation for fast drying (drainage) of porous materials.

Key words: Dynamic effects; Capillary pressure; Porous mechanics; Moisture transport; Drying shrinkage; Numerical simulation; Fluid-solid interaction

Résumé

La durabilité des infrastructures constituées de matériaux poreux, tels que le sol, le sable et les matériaux cimentaires, est étroitement liée aux conditions environnementales. La plupart des mécanismes de détérioration sont régis par l'état d'humidité des matériaux poreux. En effet, l'état d'humidité détermine la répartition de la pression capillaire qui est une force importante pour la déformation solide et pourrait augmenter le risque de fissuration. Cependant, la plupart des modèles d'interaction fluide-solide utilisés pour prédire le transport de l'humidité et de la déformation solide ont ignoré le phénomène physique existant, qui est les effets dynamiques sur la pression capillaire. Cette thèse vise à améliorer le modèle d'interaction fluide-solide avec la prise en compte de cet effet de capillarité dynamique. Trois modèles dynamiques correspondant à différents types de matériaux poreux ont été développés. Le premier modèle est disponible pour les matériaux poreux à perméabilité relativement élevée, tels que le sable et le sol. Le deuxième modèle est utilisé pour les matériaux à base de ciments matures à faible perméabilité. Le troisième modèle est développé pour les matériaux cimentaires durcissant exposés à des conditions d'humidité relative extrêmement faibles. Chaque modèle dynamique et le modèle non dynamique correspondant ont été utilisés pour simuler des expériences de séchage (drainage) documentées pour le sable, la pâte de ciment mature et le béton durcissant, respectivement. En comparant avec des données expérimentales, les simulations numériques montrent que la modélisation avec effets dynamiques donne de meilleurs résultats que la modélisation non dynamique. Toutes les comparaisons et investigations ont renforcé la nécessité de considérer l'effet de la capillarité dynamique pour prédire le transport d'humidité et la déformation solide pour un séchage rapide (drainage) des matériaux poreux.
Mots clés: Effets dynamiques; Pression capillaire; Mécanique poreuse; Transport d'humidité; Retrait de séchage; Simulation numérique; Interaction fluide-solide

Table of contents

List of Figures

List of Tables

List of notations and abbreviations

Nomenclature

α	Parameter of capillary retention model
$\bar{\sigma}$	Volumetric stress
ϕ	Effective porosity
Ψ	Helmholtz free energy of an open system
$\sigma_{ij}^{'}$	Effective stress tensor
τ	Dynamic effects coefficient
b	Biot's coefficient
D	Effective diffusion coefficient
k	Effective permeability
l	Pore connectivity parameter
m	Parameter of capillary retention model
n	Parameter of capillary retention model
P_c^{dyn}	Dynamic capillary pressure
P_c^{stat}	Static capillary pressure
P_v^0	Vapour pressure within the media near the surface
P_v^e	Surrounding vapour pressure

R	Gas constant
S_w^0	Water saturation within the media near the surface
S_w^{ir}	Irreducible water saturation
T	Absolute temperature
u	Solid matrix displacement
w	Mass flux of moisture
δ_{ij}	Kronecker delta symbol
η_w	Dynamic water viscosity
λ_b	Lame's moduli
μ_b	Chemical poential per mass unit for water vapour
μ_w	Shear modulus
ϕ_0	Intrinsic porosity
ψ_g	Helmholtz free energy per mass unit of gas mixture
Ψ_s	Free energy of solid matrix and interfaces
ψ_w	Helmholtz free energy per mass unit of liquid water
ρ_a	Dry air density
ρ_g	Gas mixture density
ρ_v	Water vapour density
ρ_w	Water density
σ_{ij}	Stress tensor
ε_{ij}	Strain tensor
ε_v	Volumetric strain
D_0	Free diffusion coefficient

D_a	Apparent diffusion coefficient
D_{ijkl}	Fourth-order stiffness tensor
D_v	Mass per unit of initial volume of the porous sample for liquid water
E_v	Emissivity
H_{ce}	Air-entry pressure head
H_w	Water pressure head
k_0	Intrinsic permeability
K_b	Bulk modulus of porous body
k_{rw}	Relative permeability of water
K_s	Bulk modulus of solid
m_g	Mass per unit of initial volume of the porous sample for gas mixture
M_v	Vapour molar mass
M_w	Water molar mass
P_c	Capillary pressure
P_g	Gas mixture pressure
P_{vs}	Saturated water vapour pressure
P_w	Water pressure
S_e	Effective saturation
S_w	Water saturation
V_a	Velocity of dry air
V_g	Velocity of gas mixture
V_v	Velocity of water vapour
V_w	Velocity of liquid water

ABBREVIATIONS

$\mathrm{C-S-H}$	Calcium silicate hydrate
FEM	Finite Element Method
LM	Levenberg–Marquardt
RH	Relative Humidity
SCC	Self-Compacting Concrete
WVSIs	Water vapour sorption isotherms

Introduction

1. Motivation

Porous materials consist of solid matrix with pores that can be fully or partially filled with fluids. The investigation on fluid flow in deforming porous materials is significant for various fields of science and engineering, e.g. geotechnical engineering and geophysical engineering, structure engineering and agriculture. The porous materials from sand and soil to cement-based materials are widely used in engineering practice. Although, serious attention has been payed to improve our understanding of mechanical behaviour of fluid flow in porous materials, developing more physical and practical governing models for durability prediction is still an open issue.

Porous materials are always subjected to biological, physical or chemical degradation processes. Indeed, the transport of water molecule plays an important role in durability and sustainability of porous materials. For instances, the liquid-water could transport chloride ions, alter mechanical behaviour, cause freeze-thaw damage, and induce negative pore pressure resulting in shrinkage [14–16]. In order to provide a preciser prediction for durability of porous materials, it is very important to have a better understanding of the moisture behaviour in porous materials and its influence on deformation of porous solid.

In this thesis, we strictly focus on moisture loss and shrinkage of porous materials. The moisture loss always occurs at the interface of porous materials and surrounding as the boundary water pressure or external relative humidity decreases. For high permeability materials, this process is called drainage. Concerning low permeability materials, it is called drying. When the porous materials become unsaturated, the negative tension capillary pressure appears and will be imposed on pore wall. It is also the driving force of drying shrinkage and can increase the cracking risk and cause damage. The capillary pressure is closely relevant to water saturation, which is mainly determined by moisture movement. Since the drying shrinkage in turn has an influence on pore network and then on fluid flow. Thus, the drainage (drying) is a complex phenomenon and must be mastered.

Modelling of unsaturated moisture transport and drying shrinkage for porous materials have been studied for decades. Water retention curve gives the relationship between water saturation and capillary pressure, which is vital supplementary for solving moisture transport model [17]. However, in the early days, most moisture transport models used a simple approach, which adopted the same water retention curve obtained at equilibrium condition for dynamic drying process; thus, the existing physical phenomenon dynamic effects on capillary pressure for fast moisture transport has been neglected. The dynamic effects on capillary pressure have been recognized as one non-negligible characteristic of moisture behaviour for porous materials, such as sands and soils [18–21]. Recent studies recorded in [22–25] have indicated that this simplified approach is hard to provide accurate prediction and suggested to take dynamic effects on capillary pressure into account.

2. Objectives

At the microscopic scale in pores the dynamic fluid equations (for instance Navier-Stokes) are applied to simulate the fluid flow. At the macroscopic scale the Darcy's law is used. Between these two scales, at which pores are not explicitly represented in the numerical volume, but their behaviour have an important influence on the total behaviour of the porous medium, it is suggested to add a parameter in the macroscopic equations to consider the microscopic effects in pores. In this way, the dynamic coefficient, in sense of the fluid dynamics, is introduced in the capillary pressure equation.

The overall objective of this thesis is to optimize the fluid-solid interaction model with the consideration of the dynamic effects on capillary pressure, and then predict more accurate behaviour of moisture transport and solid deformation for porous materials. In this thesis, the model with and without the dynamic effects on capillary pressure are called 'dynamic model' and 'standard model', respectively. For this purpose, the thesis will focus on the following specific objectives and a overview of models used for various porous materials is plotted in Fig. 1:

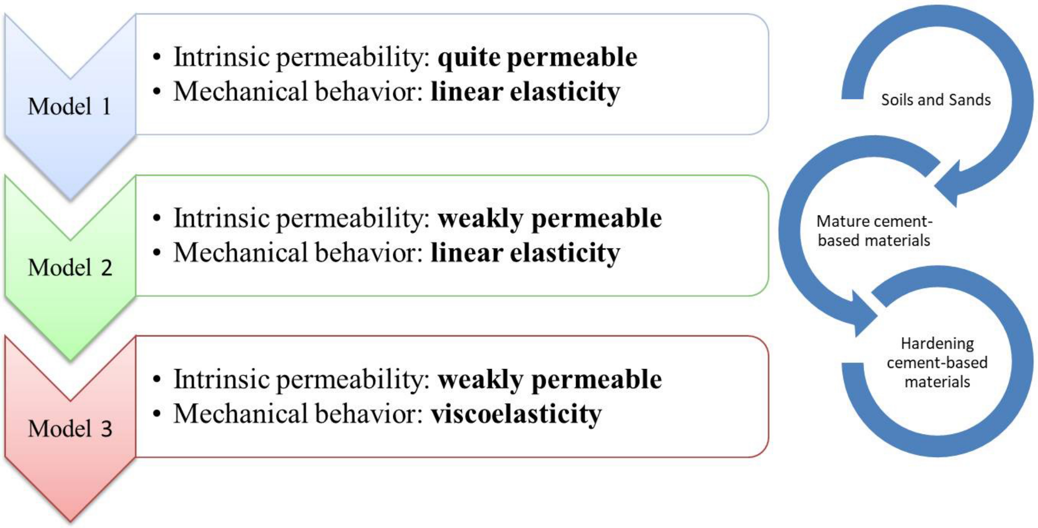

Figure 1: A overview of models used for various porous materials

First, we focus on developing model for porous materials with relative high permeability, such as sand and some kinds of soil. Since the studies on dynamic effects on capillary pressure is limited to unsaturated flow and its possible influence on deformation of porous structures are totally neglected, it is crucial to build a coupled model between unsaturated water-air flow and deformation for porous materials. In this case, the moisture transport only depends on water advection and vapor diffusion is totally neglected.

Second, the dynamic capillarity effect for weakly permeable porous materials is discussed. Considering that the moisture transport is more complicated for porous materials with low permeability, such as concrete and cement paste, a moisture transport model with the consideration of dynamic effects on capillary pressure for water advection and vapour diffusion is derived and then serves as the important part for fluid-solid interaction models.

Third, the weakly permeable porous media is still discussed. But, the mechanical behavior is supposed to be viscoelastic and the solid deformation caused by interfacial energy is also taken into account. In this case, the dynamic effects on capillary pressure is considered not only for moisture transport, but also for the release of interfacial energy according to thermodynamics. This model is applicable for hardening cement-based materials exposed to low ambient relative humidity condition.

3. Outlines of the thesis

This thesis elaborates the objectives and is organized in the following way:

Chapter 1 reviews the basic theories and models of moisture transport and solid deformation for porous materials. Then, the dynamic effects on capillary pressure are introduced and explained in detail.

Chapter 2 introduces a fully coupled model taking into account dynamic capillarity effect for unsaturated water-air flow and shrinkage within highly permeable porous materials. The dynamic model is validated with respect to documented experiment on investigation of dynamic capillarity effect in unsaturated sand sample. Then, further discussions about the application of this dynamic model in solving liquid-solid interaction problems at fast drainage condition are implemented.

Chapter 3 presents an advanced dynamic model to describe the moisture transport (consisting of water advection and vapour diffusion) and drying shrinkage of cement-based material with low permeability. A drying experiment for cement paste specimens exposed to different ambient relative humidity conditions has been analysed with dynamic and standard models to demonstrate that dynamic model can be applied successfully to predict moisture transport.

Chapter 4 develops a dynamic model with consideration of the dynamic capillarity effect and interfacial energy for drying shrinkage of viscoelastic cement-based materials. A documented drying experiment of Self-Compacting Concrete (SCC) specimens is employed as a example to verify this dynamic model. The standard and dynamic modelling approaches are studied through comparisons with documented experimental data including mass loss and average space shrinkage for verification.

Finally, a general conclusion summarizes the main contribution of this thesis and then potential future research directions are discussed. For clarity, we redefine the models and the field equations in each chapter and we can consider the chapters are independent.

Chapter 1

Context and literature review

1.1 Moisture transport in porous media

1.1.1 Introduction of porous media

Sand, soil and cement-based materials are typical porous materials encountered in practice. Generally speaking, the porous media consist of skeleton continuum and fluid continuum as demonstrated in Figure 1.1. The skeleton matrix is formed from the solid particle and

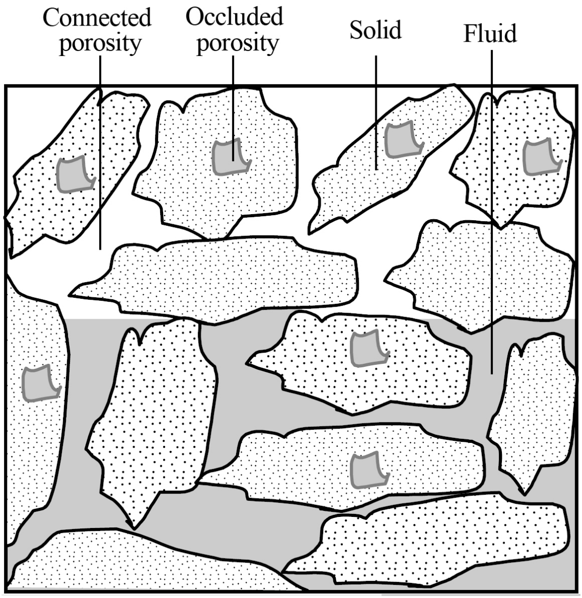

Figure 1.1: The infinitesimal volume of porous medium (taken from [1])

the empty connected pore. The fluid continuum is formed from the fluid saturating the connected and occluded pore. Because of our particular interest in transport phenomena in which advection of liquid water and diffusion of gas mixtures takes place in void space, the configuration of the void space must satisfy the requirements of connectivity [1].

1.1.2 Water states in porous media

This study focuses on two kinds of porous materials, i.e. soil and cement-based materials. Water states are greatly dependent on physical and chemical properties of porous media. Considering the typical water states in these two kinds of porous materials are different, It should be introduced respectively.

As for soil which is formed from granular particles, small amounts of water molecules are adsorbed to the surface of the particles in the form of thin films due to intermolecular forces and electrostatic forces (see Fig. 1.2(a)). The film thickness is determined by the strength of molecular level interactions between solid and water. For the sake of the tight bonding of the adsorbed water to the solid surface, this water is supposed to be immobile [26]. As the water saturation continues to increase, additional water is attracted due to cohesion forces. It is defined as capillary water which is initially formed in acute corners. In terms of granular porous media, pendular rings are formed around the contact points of grains as presented in Fig. 1.2(b). The pendular water is still hard to establish continuous flow paths. Hence, it is regarded as settled water macroscopically. If the amount of water improves further, the funicular stage appears, in which the growth of thickness of the water films helps to build a connected water system along pore walls corresponding to Fig. 1.2(c). The water flow is available at this stage. On the other hand, the gas mixtures are continuous in porous system for the mentioned three stages. Nevertheless, if the water continues to go up, the pores with small cross-section can be absolutely filled with water, which leads to the end of continuity of gas mixtures. Thus, the air bubbles is observed (see Fig. 1.2(d)). When the pore is entirely filled with water, the fully saturated stage is reached. We note that for quite permeable material soil, the evaporation and dissolution are ignored in this work.

As a component of cement-based materials, water have significant influence on their physicochemical and mechanical properties [27]. Water exists in hydrated cement-based

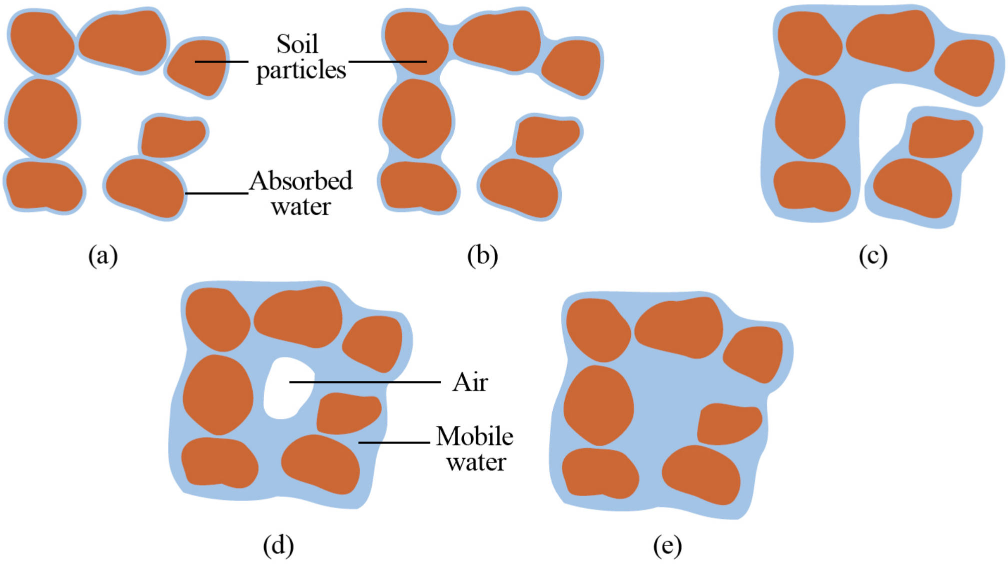

Figure 1.2: Configurations of water and air in soil (sand): (a) absorbed regime, (b) capillary pendular regime, (c) capillary funicular regime, (d) occluded air bubble regime, (e) fully saturated regime (taken from [2])

materials in various forms. According to the degree of difficulty or ease with which it can be removed from the hydrated cement paste, the water is classified into several types. The water states associated with calcium silicate hydrate (C-S-H), the main hydrate in cement paste, are plotted in Fig. 1.3 according to the Feldman-Sereda model [3].

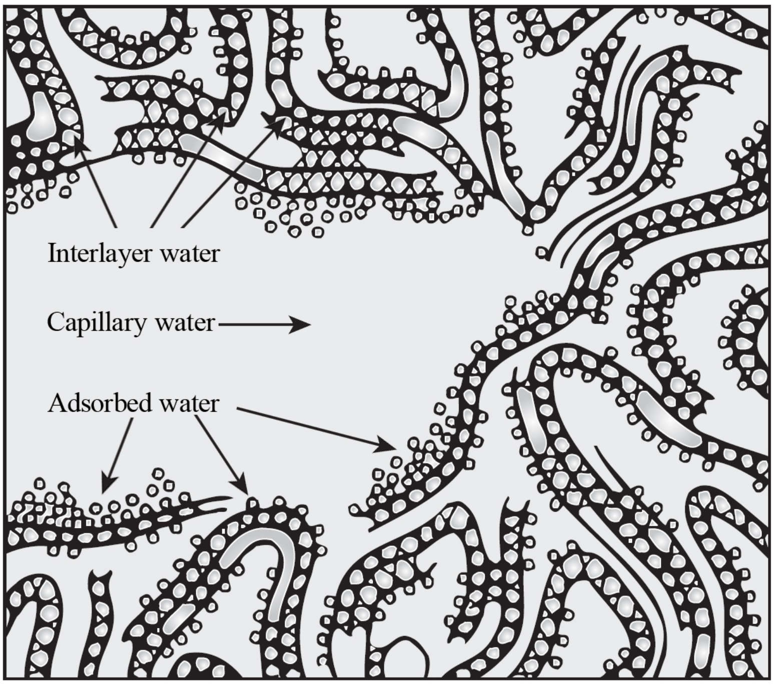

Figure 1.3: Diagrammatic model of types of water associated with C-S-H (taken from [3])

1) Capillary water which is the water presented in void with size larger than 5 nm. According to the performance of capillary water, it can be divided into two categories: the water in large voids (size 10 μm - 50 nm) is defined as free water. Its transport has no impact on volume change. Water in smaller capillary pores (size 50 nm to 5 nm) is held by capillary tension. The capillary water is easy to transport which may result in shrinkage phenomenon for the system.

2) Adsorbed water represents the water bond in the vicinity of solid surface due to the action of intermolecular forces and electrostatic forces (see Fig. 1.3). As the bond energies of the individual water molecules decrease with distance from the solid surface, a major portion of this water can be released when low relative humidity is reached. The loss of adsorbed water is the main cause of shrinkage.

3) Interlayer water is highly combined to layers of Calcium silicate hydrate (C-S-H). This water is hard to evaporate. Hence, only extremely low relative humidity condition could affect this water. The loss of interlayer water is responsible for the shrinkage of C-S-H structure.

4) Chemically combined water is an integral part of the hydration products. This water is not considered as liquid phase. The evacuation of this water provokes the destruction of cement paste observed under fine conditions.

As the ambient relative humidity decreases, the hydric gradient is caused. Thus, the moisture begins to move from interior to exterior to rebuild the gradient equilibrium. Then the drying occurs on the open surface of the system. The mechanism implies that the drying is complex, multiple and interdependent [28].

1.1.3 Water retention and Moisture sorption

For more porous materials, such as soils and sand, a great amount of menisci can be formed in void. The relationship between macroscopic (or Darcy-scale) capillary pressure and water saturation of porous media is called retention function:

$$P_c = P_c\left(S_w\right). \tag{1.1}$$

where P_c represent the capillary pressure function and S_w is the water saturation. This relationship is also known as capillary function, suction function and soil water characteristic function [29–32].

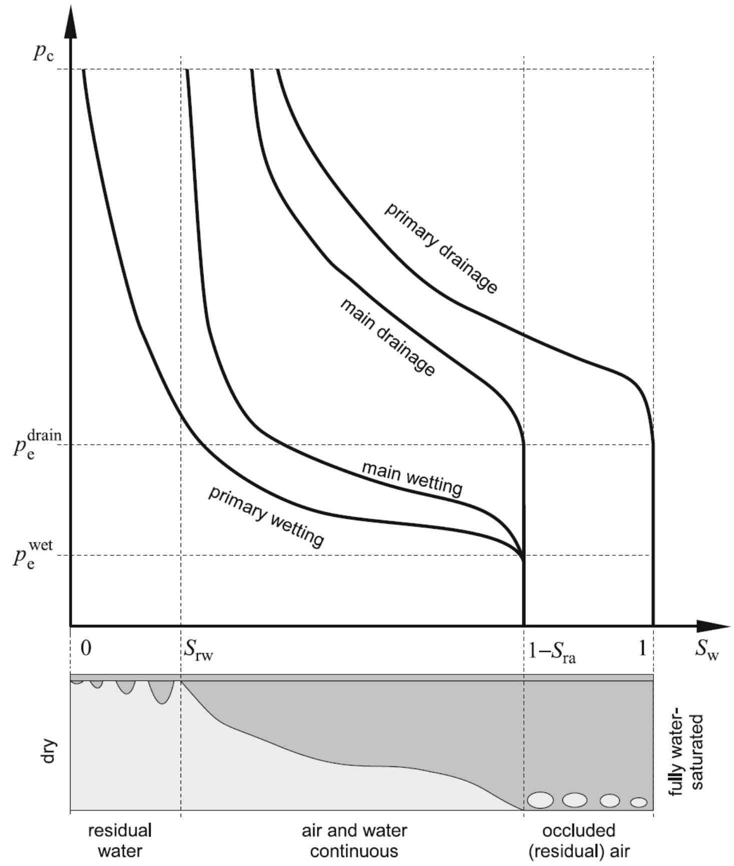

Figure 1.4: Capillary pressure–water saturation relationship for various air and water flow regimes (figure from [2])

In Fig. 1.4, the typical retention curves are plotted. It directly demonstrates fundamental behaviours related to distinct configurations of liquid water and gas mixtures in void. Assuming that the void is entirely filled with water initially, only if the pressure of gas exceeds the air-entry pressure, it can invade into porous media resulting in unsaturated phenomenon [31]. The air-entry pore pressure often exists in granular porous material with uniform grain size. However, it is hard to observe pronounced air entry pressure for fine-textured porous materials [33]. The specific value of air entry pressure is determined by the radius of the biggest pore forming a continuous path through the whole materials. After the gas pressure exceeds the air-entry pressure, the water saturation decreases with the increase of capillary pressure. The slope of the retention curves is a reflection of the distribution of pore network. If the pore size is close, most of water in this size of pore drains simultaneously as corresponding capillary drive force reaches and the slope of the retention curve must be steady. If the pore size ranges in a large scale, only a small amount of pores can be emptied at each increment of capillary potential. Thus the decrease rate of saturation is much slower. As the drainage continues until the residual water saturation is reached, the liquid flow is impossible due to lack of connectivity of the pendular capillary water. At this point, the evaporation begins to play a main role in saturation reduction. The evaporation, governed by the relative humidity condition, needs an extremely high capillary potential according to Kelvin equation [31]. The Brooks and Corey model [34] and van Genuchten model [35] are used widely to express the relationship saturation and capillary pressure for soil and sand. The review of these two models will be presented in Chapter 2.

It is well-known that capillary function curves not only show hysteresis but also rely on flow history. There are several explanations for hysteresis including variations in contact angle between imbibition and drainage procedure and ink-bottle effect [33, 36]. The ink-bottle effect is due to the reality that the action of capillary flow is great determined by the maximum cross-section of the pore during imbibition, while it is governed by the minimum cross-section for drainage procedure.

For cement-based material, which is less porous medium, it attains or releases moisture through the sorption process. The water vapor sorption isotherms (WVSIs) [37] is adopted to describe the relationship between water saturation and relative humidity at equilibrium condition. A schematic representation of a typical sorption isotherm with a hysteresis between the adsorption and desorption isotherms is plotted in Fig. 1.5. Indeed, the sorption isotherms for cement-based materials have identical function with retention curves for soils and sands. These two relationships can be transformed from one to the other on the basis of Kelvin's equation. That means there is an intrinsic relationship between capillary pressure, water saturation and relative humidity. Given the relationship between any two of them, the last one can be definitely solved.

The sorption consists of adsorption and desorption. The adsorption is induced by interaction forces between water molecules and solid surface. These forces include physical and chemical parts. The physical sorption is due to van der Waals attraction between adsorbate and adsorbent. The chemical sorption is due to the attractive chemical bonding between adsorbate and adsorbent.

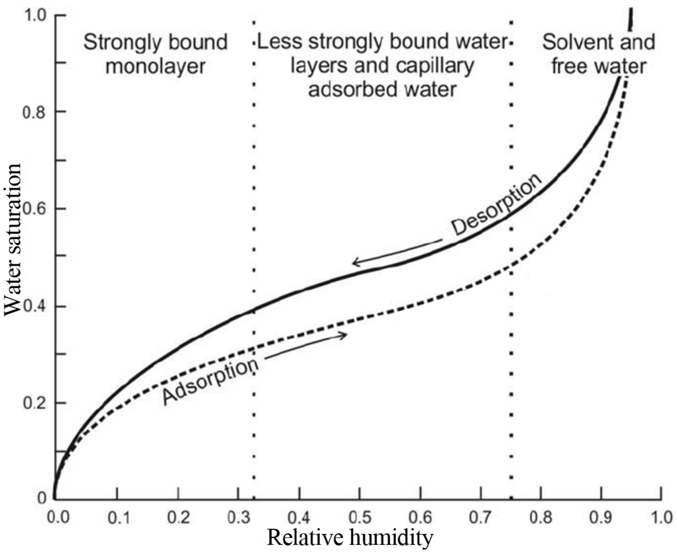

Figure 1.5: A schematic representation of a sorption isotherm with a hysteresis between the adsorption and desorption isotherms (figure from [4])

The capillarity is formed due to menisci between liquid water and gas mixtures. The existence of surface tension γ is the main cause of capillarity. The Young-Laplace equation gives the value of force balance at this interface:

$$P_c = P_g - P_w = \frac{2\gamma}{r^*}, \tag{1.2}$$

where P_g and P_w are gas mixtures pressure and liquid-water pressure, respectively. r^* indicates the mean radius of curvature.

As mentioned previously, the water vapor could condense or release from the pore walls based on the variation of vapor concentration. The menisci must be observed in pores with different size. Considering that the vapor concentration is dependent on the relative humidity at the macroscopic scale, there is a potential relationship between relative humidity and water saturation in porous materials. In terms of cement-based materials, the sorption isotherms curves can be measured by saturated salt solution method as recorded in [37]. Similar with water retention curve, there also exist hysteresis for adsorption and desorption isotherms curves for cement-based materials [38, 39].

Isotherms are classified into six types according to the International Union of Pure and Applied Chemist (IUPAC) classification [40]. There are a series of sorption models, including Langmuir [41], BET [42], Dent [43], etc., could give high fitting results of sorption isotherms. The generalized Langmuir equation is suitable for monolayer adsorption. It also assumes that the adsorption rate is not only proportional to gas pressure but also the area surface that without adsorbed gas molecules. BET and Dent's isotherms are an extension of the Langmuir theory. They are available for multilayer adsorption. It should be emphasized that these models are valid only under a certain condition that the relative humidity is low than 45% [44]. Nonetheless, durability investigation on cement-based infrastructures is related to comparatively high relative humidity condition ranging from 50% to 100%. In this range, both capillarity and sorption have effects on water-vapour sorption isotherms. This is the reason that the empirical equation used in soil research is adopted to fit the measured sorption curves of cementitious materials [28, 45, 46].

1.1.4 Mechanisms of moisture transport

Moisture transport in porous materials is very complex, which is a comprehensive expression of various mechanisms. As for weakly permeable porous media, it includes a series of phenomena, i.e. adsorption, desorption, condensation, evaporation, water flow, vapor diffusion, etc. A schematic representation of mechanism of moisture transport is presented in Fig. 1.6. Generally, the description of moisture transport can be divided into three stages according to the degree of relative humidity condition.

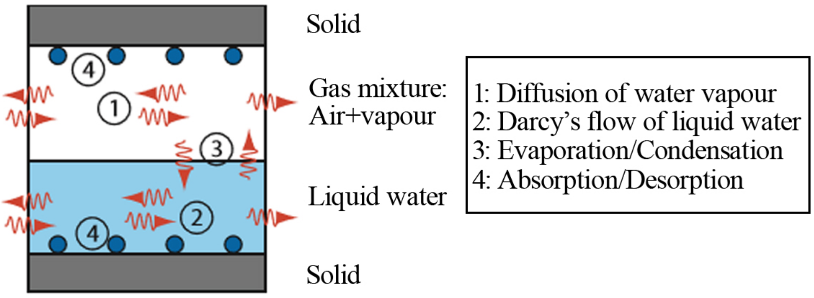

Figure 1.6: A Schematic representation of mechanisms of moisture transport (taken from [5])

1) At high relative humidity stage, the water saturation is high which indicates most of the free liquid water is continuous. The transport of moisture is principally in the form of liquid water. The gradient of capillary pressure is the driving force for this movement, thus the extended Darcy's law can be applied.

2) At intermediate relative humidity stage, the region of continuous liquid-water continues to reduce which weakens the capillary transport. On the other hand, the vapor diffusion continues to strengthen. It means that the liquid water flow and vapor diffusion occur simultaneously. As the drying develops further, the vapor diffusion has preponderance compared with liquid water flow.

3) At low relative humidity stage, there is no continuous liquid water in the pore, while the gas mixtures are continuous. The vapor diffusion plays more important role in moisture transport. While, the contribution of liquid water flow is almost negligible. Indeed, the water molecules are adsorbed on the surface of pore walls due to van der Waals forces [47, 48]. Evaporation occurs at the interface between liquid water and gas mixtures. This procedure is caused by the non-equilibrium between capillary pressure and vapor pressure. Then the evaporated vapor can be transported by diffusion through the pore. The diffusion includes ordinary diffusion, Knudsen diffusion [49], and surface diffusion [50]. The specific diffusion procedure is demonstrated in Fig. 1.7.

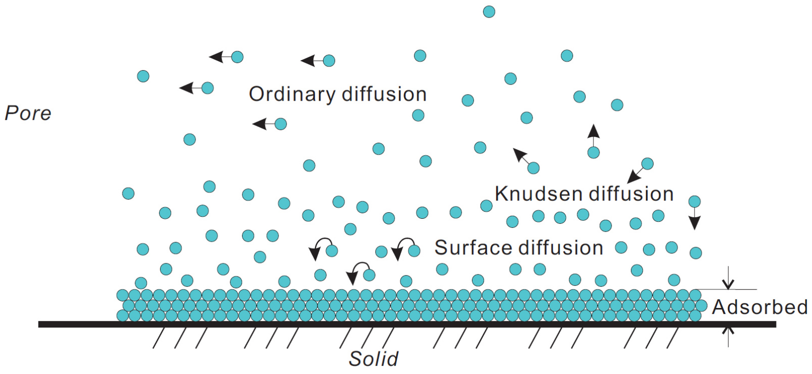

Figure 1.7: A schematic representation of diffusion (figure from[6])

As for quite permeable porous materials, such as soils and sands, hydraulic flow is the main approach of moisture transport when materials are directly in contact with liquid water. The vapor diffusion is always ignored, since its contribution on entire moisture transport is totally negligible. The moisture transport is regularly driven by external imposed water pressure gradient.

1.1.5 Moisture transport model for porous media

The governing model of unsaturated water-air flow for porous media is derived from the mass conservation principle. The extended Darcy's law, which is appropriate for the case of unsaturated system, is originally introduced by Buckingham [51]. Substitution of the extended Darcy equation into the mass balance equation for water and air phases leads to the typical governing equations. After that, Richard [52] proposes a simplified governing equation in which the air pressure is assumed to be constant and equals to atmospheric pressure. It is known as Richards' equation. Since then, a series of models have been developed for moisture transport simulation. Philip and de Vries [53] pioneer the investigation on theoretical basis models in the late of 1950s. Subsequently, multiphase transport model is employed in a lot of studies of Bear [1]. In addition, multiphase transport models with the consideration of liquid-water, water-vapour and dry air have been developed for cement-based materials [54–57].

As for most of materials used in civil engineering, such as sand and concrete, the order of magnitude of permeability ranges from 10^{-10} m^2 to 10^{-21} m^2. Since the moisture transport in porous media is greatly dependent on permeability, specific microstructure as well as initial and boundary conditions, etc., specific models should be chosen for specific porous materials. It is very important to understand the mechanisms of moisture transport process. The moisture transport includes advection of liquid-water, evaporation of liquid-water, diffusion of vapor and variation of gas mixtures. Coussy [58] has proposed a complete model coupling all above mechanisms.

Indeed, the air viscosity is 55 times smaller than that of water at room temperature. It indicates that the mobility of gas mixtures is greater than liquid water. Thus, there is no pressure gradient in gas mixtures. One can assume the gas mixtures pressure to be at a constant atmospheric pressure. Ignoring the movement of gas mixture, the multiphase model can be simplified as Richard's equation, which is widely accepted for the case of water flow in unsaturated soils and sand. The specific derivation of Richard's equation is presented in Chapter 2.

In term of weakly permeable porous medium, e.g. concrete, the moisture transport is not only dependent on the water advection, but also the vapor diffusion. Most of standard drying models [6, 54, 55, 59, 60], developed on the basis of the assumptions that air pressure is constant and advection of vapor is negligible, are a simplified form of the Coussy's model. The simplified model can also provide high accuracy for drying process. In chapter 3, a well-accepted multiphase model based on continuum approach is recalled. Here, the complete transport model of Coussy and a series of typical drying model for cementitious materials are reviewed in this section.

Continuum approach of Coussy [61]

The derivation of this approach is based on the assumption that there is no chemical reaction and the skeleton deformation is neglected. In addition, since the moisture transport is relatively slow in terms of weakly permeable materials, the momentum of each phase is not taken into account. After the discussion above, it can draw a conclusion that the moisture transport is merely governed by mass conservation laws. The mass balance for liquid water (denoted w), the water vapour (denoted v) and dry air (denoted a) are presented as below:

$$\frac{\partial\left[\rho_w \phi S_w\right]}{\partial t}+\nabla\left(\rho_w V_w\right)=-m_{w-v}, \tag{1.3}$$

$$\frac{\partial\left[\rho_v \phi\left(1-S_w\right)\right]}{\partial t}+\nabla\left(\rho_v V_v\right)=m_{w-v}, \tag{1.4}$$

$$\frac{\partial\left[\rho_a \phi\left(1-S_w\right)\right]}{\partial t}+\nabla\left(\rho_a V_a\right)=0, \tag{1.5}$$

where ρ_α and V_α $(\alpha=w,v,a)$ indicates density and velocity of corresponding phase, ϕ the porosity which provides the space for unsaturated water-air flow, S_w the water saturation which includes interstitial water (capillary water) and physically-adsorbed water and m_{w-v} the rate of liquid water changing into vapour.

Both water-vapour and dry air are transported by Darciean advection and by Fickian diffusion. The former is governed by Darcy's law and the latter is governed by Fick's law. The velocity of gas mixture V_g , also called filtration vector, is defined as the molar average:

$$V_g=x_a V_a+x_v V_v, \tag{1.6}$$

where x_a and x_v represent the mole fraction relate to the dry air and to the vapor. On the basis of the assumption of ideal gas, the mole fraction of each component corresponds to ratio of pressure as $x_a = P_a/P_g$ and $x_v = P_v/P_g$, where P_v, P_a and P_g represent the partial pressure of vapour, dry air and the pressure of gaseous mixture. There exists a relation that $x_a + x_v = 1$. Therefore, the following formulas are obtained:

$$V_v = V_g + x_a \left(V_v - V_a\right), \tag{1.7}$$

$$V_a = V_g - x_v \left(V_v - V_a\right). \tag{1.8}$$

In accordance with the second law of thermodynamics, the positiveness of the dissipation associated with transport of gaseous mixture should be satisfied [62].

$$-\nabla P_g \cdot V_g - \nabla x_v \left(V_v - V_g\right) \geq 0, \tag{1.9}$$

here, the first term is the dissipation associated with the advection of gaseous mixture, the second term accounts for the dissipation related to diffusion of the vapour through the air. Combining Darcy's and Fick's laws and taking into account the relation $x_v = P_v/P_g$ and condition relate to second law of thermodynamics mentioned previously, we finally write Eqs (1.7) and (1.8) in the more operationally explicit form:

$$V_v = -\frac{kk_{rg}}{\eta_g}\nabla P_g - \left(\phi\left(1 - S_w\right)\tau_0\right) D_0 \frac{P_{atm}}{P_v}\nabla\left(\frac{P_v}{P_g}\right), \tag{1.10}$$

$$V_a = -\frac{kk_{rg}}{\eta_g}\nabla P_g + \left(\phi\left(1 - S_w\right)\tau_0\right) D_0 \frac{P_{atm}}{P_a}\nabla\left(\frac{P_v}{P_g}\right), \tag{1.11}$$

where τ_0,D_0 and P_{atm} indicate tortuosity, diffusion coefficient of vapour or dry air in the wet mixture and the atmospheric pressure. k, k_{rg} and η_g are respectively intrinsic permeability, relative permeability and viscosity of gas mixture. The velocity of liquid water is governed by the Darcy's law.

$$V_w = -\frac{kk_{rw}}{\eta_w}\nabla P_w, \tag{1.12}$$

where k_{rw} the relative permeability η_w the dynamic viscosity of liquid water.

Intrinsic permeability is an important factor for moisture transport. Even though some recorded studies indicate that there exists discrepancy between gaseous mixture and liquid-water in terms of intrinsic permeability [63, 64], the intrinsic permeabilities of gaseous mixture and liquid-water are always assumed to be identical in most studies. Indeed, this assumption is reasonable due to the fact that the intrinsic permeability is only related to the property of porous material itself and independent of the type of fluid.

It is necessary to keep the thermodynamic equilibrium between the liquid and vapor phases of water. This equilibrium is always accounted by Kelvin equation which is written in the following form:

$$P_w - P_{atm} = \frac{\rho_w RT}{M_v} \ln\left(\frac{P_v}{P_{vs}}\right), \tag{1.13}$$

where P_{vs}, R, T and M_v represent saturated vapour pressure, gas constant, absolute temperature and vapour molar mass, respectively. Due to the support of capillary pressure curve (also called sorption isotherm curve concerning cement-based materials), which gives the relationship between capillary pressure and saturation, the Kelvin equation is rewritten as follows:

$$-P_c\left(S_w\right) + P_g - P_{atm} = \frac{\rho_w RT}{M_v} \ln\left(\frac{P_v}{P_{vs}}\right). \tag{1.14}$$

This equation gives the capillary pressure as a function of relative humidity $RH = P_v/P_{vs}$. To solve the problem, the vapor and dry air can be roughly considered as ideal gas. So that, both of their densities and pressures should follow the laws:

$$\rho_v = \frac{P_v M_v}{RT}, \tag{1.15}$$

$$\rho_a = \frac{P_a M_a}{RT}, \tag{1.16}$$

$$P_g = P_v + P_a, \tag{1.17}$$

where M_a is the molar mass of dry air. Furthermore, the liquid water is assumed to be incompressible, since the variation of temperature is not taken into account. Until now, a complete multiphase model is obtained by Coussy [61]. Most of transport model concerning cement-based materials is a type of simplification of the complete multiphase model. In general, the simplification is based on all or part of the following assumptions:

1) Gas pressure in the porous material is constant and always equal to the atmospheric pressure.

2) The contribution of vapour advection on moisture transport is weak and can be neglected, which means that the vapour transport is considered as a pure diffusion procedure.

3) The transport of gas mixture including vapour diffusion and advection of gaseous mixture are neglected. The moisture transport is merely related to liquid water flow.

Apart from the simplified continuum approach model, there exist other kinds of drying models. We are going to review the typical one that has been used in the field of cement-based materials.

EMPD model

The effective moisture penetration depth model, EMPD for short, has been originally proposed in [65]. This model has been widely used [66–68], since it could provide modelling results have good agreement with recorded experiment data under certain conditions. The derivation of this model is on the basis of a key assumption that the moisture buffering process occurs in a thin fictitious layer of interior element's material with thickness d_{EMPD}. This layer is also called moisture buffering layer. The uniform moisture content is a function of relative humidity. The specific model is presented as below [69]:

$$\rho_{mat} d_{EMPD} \frac{d\theta}{dt} = k_m \left(RH_p - RH^e \right), \tag{1.18}$$

where ρ_{mat}, θ and k_m indicate dry density of the adsorbing material, water content and coefficient of moisture transport respectively. RH_p and RH^e are relative humidity at depth d_{EMPD} and the external relative humidity. For a cyclic moisture variation, if the sorption curve and vapor permeability δ_{perm} are known, the EMPD could give precise solution. The moisture penetration depth d_{EMPD} which in turn depends on the period of the humidity variations is written as follows [70]:

$$d_{EMPD} = \sqrt{\frac{\tau_p p_{vs} \delta_{perm}}{\rho_{mat} \pi \frac{d\phi}{dRH}}}, \tag{1.19}$$

where τ_p is the humidity cycle period and p_{vs} is saturated vapor pressure.

The disadvantage of EMPD model is that its dependence on the moisture penetration depth [66]. This feature can merely be calculated from the moisture capacity and vapour permeability, measurements which are time consuming and labour intensive. In addition, the moisture penetration depth, which is the most significant factor of this model, is calculated by empirical equation. It is a non-negligible drawback and may reduce the accuracy.

Cunningham's method

The Cunningham's method [71] is based on the principle that the driving force of moisture transport in porous media is the gradient of moisture concentration and temperature. This method is suitable especially for the periodic temperature boundary conditions. The specific equation for Cunningham's method is given as follows:

$$\frac{\partial S_w}{\partial t} = \frac{\partial}{\partial x}\left(D_s \frac{\partial S_w}{\partial x} + D_T \frac{\partial T}{\partial x}\right), \tag{1.20}$$

where D_s represents the diffusion coefficient under moisture gradient which includes the contributions of liquid water flow and vapour diffusion for the entire moisture transport. D_T is the diffusion coefficient under temperature gradient. As for drying modelling of cement-based materials exposed to fire, this model has absolute advantages.

However, this model has restricted requirements for initial and boundary conditions. To obtain an analytical solution, the following assumptions are made. Since the time constant of response for temperature is very much shorter than for the moisture concentration, the Fourier number F_0 is assumed to far greater than 1, i.e.

$$F_0 = \frac{\kappa}{\rho_v l^2 C_T} \gg 1, \tag{1.21}$$

where κ is the thermal conductivity, which is always assumed to be constant because of the fast temperature diffusion. l and C_T are the length and temperature energy capacity of the porous media. Furthermore, the terms $\frac{\partial D_s}{\partial S_w}$ and $\frac{\partial D_T}{\partial S_w}$ are also assumed to be constant. Obviously, the applicability of this model is limited.

1.2 Shrinkage of porous materials

Shrinkage is a complex procedure for porous materials. In this section, cement-based materials are adopted as an example to introduce various types of shrinkage. Shrinkage of cement-based materials occurs during the entire stage including early age and later age. The early age is the stage that the cement-based materials are setting and beginning to harden. The later age refers to the stage after twenty four hours. The autogenous shrinkage, drying shrinkage and thermal shrinkage occur at both stages. The chemical shrinkage and carbonation shrinkage happen at early and later stages respectively.

1.2.1 Types of shrinkage

1) **Autogenous shrinkage**

Autogenous shrinkage is the macroscopic volume reduction of a closed, isothermal, cementitious material system not subjected to external forces. It is due to the internal consumption of water when cement hydrates after initial setting. It is also known as self-desiccation shrinkage. In the absence of an external source of water that could saturate the pore of the hydrating cement paste, the very fine porosity created by this chemical contraction drains an equivalent volume of water from the coarse capillary pores of the hydrating cement paste. Thus, menisci appear in these pores. As explained above, the emptying of the larger capillary pores causes the internal humidity to drop [72], and this self-induced drying induces tensile stress and shrinkage, i.e. self-desiccation shrinkage [73].

2) **Chemical shrinkage**

Chemical shrinkage is the volume reduction at the early ages of hydration due to the formation of products of hydration with smaller volume compared with the volume of the initial reactants [74]. Chemical shrinkage is like a molecular-level volume change (absolute internal volume change), and is considered as the underlying driving force for the occurrence of autogenous shrinkage (apparent volume change) [75]. A typical relationship between the chemical and autogenous shrinkage in concrete is described in Fig. 1.8.

After the formation of initial slurry, the hydration continues and leads to voids in matrix. At this period, autogenous shrinkage is smaller than the chemical shrinkage due to main reason explained as following. First, the autogenous shrinkage is only the measured apparent volume reduction. However, the volume of voids is included in the measurement of chemical shrinkage. During the plastic shrinkage stage, the values of autogenous shrinkage and chemical shrinkage may be roughly assumed to be equivalent.

3) **Plastic shrinkage**

Plastic shrinkage is the volume contraction occurs in a fresh concrete, after placing and before hardening of the concrete. This type of shrinkage is caused by the water

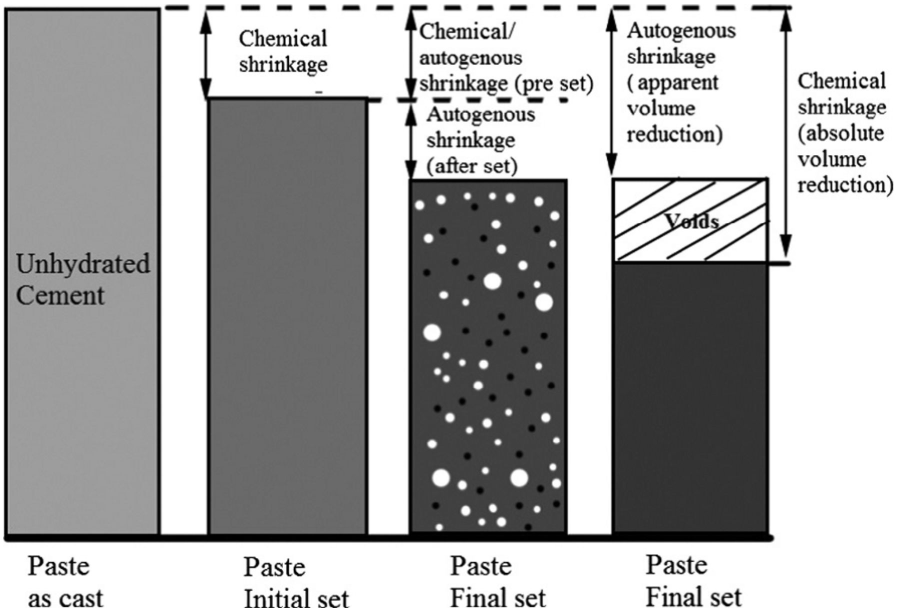

Figure 1.8: The relationship between chemical shrinkage and autogenous shrinkage (taken from[7])

loss by evaporation from its surface. [76]. At the surface, plastic shrinkage appears as the rate of evaporation exceeds the rate of bleeding. Contraction causes tensile stress in the surface layers because they are restrained by the non-deformable inner layers. Since concrete has a low tensile strength in its plastic state, cracking can easily appear. The more loss of water from surface, the greater the plastic shrinkage would be. Plastic shrinkage is proportional to cement content and inversely proportional to the water-cement ratio.

4) **Drying shrinkage**

Drying shrinkage is the self-contracting phenomenon of cement-based materials caused by the loss of free water due to the relative low ambient environment humidity, which often induces cracking, internal warping, and external deflection under the loading. All these could result in deterioration of durability in concrete structures. The development of drying shrinkage is lengthy compared with autogenous shrinkage. In order to prolong the longevity of structures, it is important quantitatively to predict shrinkage in concrete as well as to control cracking within the design stage. The drying shrinkage is always obtained indirectly by decreasing the autogenous shrinkage of the sealed specimens from the total measured deformation of the concrete. Considering that the low surrounding relative humidity condition could weaken the hydration of cement, which makes the shrinkage not a simple superposition. Indeed, the drying shrinkage value obtained by traditional measurement approach may contain part of autogenous shrinkage.

5) **Thermal shrinkage**

Thermal shrinkage is the volume contraction provoked by excessive temperature gradient between interior and exterior or temperature reduction in the early stage of hardening of concrete [77]. The temperature difference predominately owes to the release of heat in the cement hydration process. The release of heat is accompanied by thermal expansion. As the process advances, the mixture continues to cool which leads to shrinkage deformation. The actual temperature change is dependent on environment conditions and also impacted by concrete composition.

6) **Carbonation shrinkage**

Carbonation shrinkage is caused by the carbonation of concrete. Carbonation is a process that permeation of CO2 from the environment causes chemical reaction with calcium hydroxide as well as destabilization of calcium silicate hydrates (C-S-H).

$$Ca(OH)_2 + CO_2 \rightarrow CaCO_3 + H_2O. \tag{1.22}$$

It leads to the transformation of the concrete surface to get carbonated. Thus, this type of shrinkage is always observed on the surface during the entire period of the concrete structure.

1.2.2 Mechanisms of shrinkage

The volume contraction of cement-based materials is always associated to their moisture content. The mechanism of shrinkage due to moisture changes is explained in detail in this section. Kovler et al. [78] proposed three principal mechanisms to explain the shrinkage. Indeed, the observed deformation is the result of the interaction of all these mechanisms. Each mechanism is significant at the corresponding range of internal relative humidity.

1) **Capillary tension**

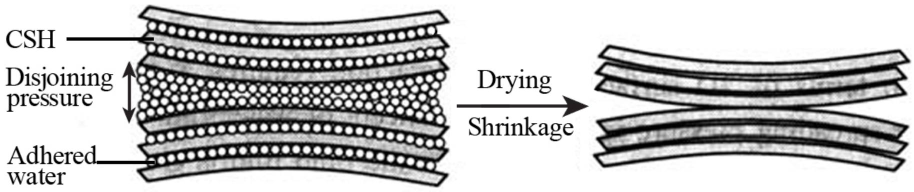

Figure 1.9: Shrinkage due to variation of disjoining pressure (adopted From [8])

The capillary pores are filled with liquid water and gaseous mixtures. The coexistence of these two phases conducts the creation of meniscus. As stated by Laplace equation, the capillary pressure, provided as the difference between gaseous mixture pressure and water pressure, is always negative, i.e. the liquid water stays in the tension state. This tensile stress in capillary water must be balance by compressive stress of the surrounding solid. Thus, emptying of capillary pores by drying could subject the porous material to compressive stress state, which could cause volumetric contraction, i.e. shrinkage.

2) **Disjoining tension**

The disjoining pressure exists in the interlayers of C-S-H particle, where the adsorption water is hindered. The distances between the adjacent interlayers are smaller than two times the thickness of the free adsorbed water layer. The adsorption of interlayer water enhances the repulsive forces, while decreases the attractive van der Waals's forces between solid layers. The net surface repulsion force and loss of attraction forces is usually referred as disjoining pressure [79]. The disjoining pressure varies with the relative humidity. In the case of drying, the thickness of adsorbed liquid water decreases, which results in the reduction of the disjoining pressure. Thus, the shrinkage is caused. The mechanism is shown in Fig. 1.9.

3) **Surface tension**

At the surface of the liquid water, the interaction forces between surface molecules and inner molecules are not in balance. A compensating force is required to apply to the surface layer of water molecules to obtain equilibrium condition. This force is the surface tension of the liquid [78]. As a result, the surface tends to contract and behaves like a stretched elastic skin. In particular of cement gel particles with massive surface area, great compressive stresses are caused [80]. The increases of such stresses could induce significant volumetric contraction. Moreover, the variations in the surface tension of the solids are merely dependent on the first three adsorbed layers. Since the outer layers are bound by small forces, their impacts on the surface tension of the adsorbent are ignorable. Thus, it has been suggested that this mechanism is valid in the range of relative humidity of $5-50\%$ [81].

Table 1.1: Shrinkage mechanisms after various authors (adopted from [12, 13])

Authors	Relative humidity					
	0	0.2	0.4	0.6	0.8	1.0
Power (1965)	Disjoining pressure					
				Capillary pressure		
Ishai (1965)	Surface energy			Capillary pressure		
Feldman et Serada (1970)	Movement of interlayer water		Capillary pressure and surface energy			
Wittmann (1968)	Surface energy			Disjoining pressure		

1.2.3 Shrinkage prediction and modelling

The principle of effective stress plays an important role in porous media mechanics. It is the effective stress that causes the deformation of the skeleton. Herein, a linear, isotropic, elastic porous media is used as a example to obtain the stress field equation. The stress–strain equations of porous material under saturated flow and infinitesimal displacement conditions are considered as follows [82, 83]:

$$\sigma_{ij} - bP\delta_{ij} = 2\mu_b\varepsilon_{ij} + \lambda_b\varepsilon_v\delta_{ij}, \tag{1.23}$$

where $\sigma_{ij}, \varepsilon_{ij}, b, \mu_b, \lambda_b, \varepsilon_v, \delta_{ij}, P$ represents stress tensor, strain tensor, Biot's coefficient, shear modulus, Lame's moduli, volumetric shrinkage, Kronecker delta symbol and pore pressure, respectively. As for unsaturated condition, the above equation evolves into the following formula:

$$\sigma_{ij} - bP_{ave}\delta_{ij} = 2\mu_b\varepsilon_{ij} + \lambda_b\varepsilon_v\delta_{ij}, \tag{1.24}$$

here, P_{ave} indicates average pore pressure consisting of water pressure P_w and gas mixture pressureP_g:

$$P_{ave} = (1 - S_w)\, P_g + S_w P_w = P_g + S_w(-P_c). \tag{1.25}$$

The geometric equation is showed as follows:

$$\varepsilon_{ij} = \frac{1}{2}\left(\frac{\partial u_i}{\partial x_j} + \frac{\partial u_j}{\partial x_i}\right). \tag{1.26}$$

The equilibrium equation is:

$$\sigma_{ij,j} + \rho f_i = 0, \tag{1.27}$$

where ρf_i represents the body force.

Substituting the geometric equation (1.26) into constitutive law (1.23), to express the stress components σ_{ij} as functions of the derivatives of the displacement components u_i. Thereafter replacing those equations into equilibrium equation (1.27) and neglecting the body forces ρf_i, it derives as follows:

$$\mu_b \nabla \cdot \nabla u + (\mu_b + \lambda_b)\, \nabla\, (\nabla \cdot u) + b \nabla P_{ave} = 0, \tag{1.28}$$

where ∇ represents the gradient and $\nabla\cdot$ the divergence. Since $\nabla \cdot u = \varepsilon_v$, the above equation can be written in details (for $i = x, y, z$):

$$\mu_b \nabla^2 u_x + (\mu_b + \lambda_b)\, \frac{\partial \varepsilon_v}{\partial x} + b\frac{\partial [P_g + S_w(-P_c)]}{\partial x} = 0, \tag{1.29}$$

$$\mu_b \nabla^2 u_y + (\mu_b + \lambda_b)\, \frac{\partial \varepsilon_v}{\partial y} + b\frac{\partial [P_g + S_w(-P_c)]}{\partial y} = 0, \tag{1.30}$$

$$\mu_b \nabla^2 u_z + (\mu_b + \lambda_b)\, \frac{\partial \varepsilon_v}{\partial z} + b\frac{\partial [P_g + S_w(-P_c)]}{\partial z} = 0. \tag{1.31}$$

The interest of shrinkage investigation is to understand the phenomenon of autogenous and drying shrinkage and then to predict the deformation of porous system in different mechanical forces and environmental conditions. The models recalled hereafter used mainly to autogenous and drying shrinkage which is supposed to be the most crucial component for porous system.

1) **Biot-Bishop model**

As for fully saturated quite permeable porous media, the deformation is governed by the variation of pore water pressure P in the absence of any external forces [82]:

$$\varepsilon_v = P\left(\frac{1}{K_b} - \frac{1}{K_s}\right), \tag{1.32}$$

where ε_v is volumetric deformation; K_b and K_s indicate drained bulk modulus of porous body and bulk modulus of its solid skeleton, respectively. Bishop [84] has extended this approach to partially saturated system. By replacing the water pressure with average pore pressure in the Eq. 1.32) and neglecting the contribution of gaseous mixture pressure, the typical shrinkage model has been obtained as follows:

$$\varepsilon_v = -S_w P_c\left(\frac{1}{K_b} - \frac{1}{K_s}\right), \tag{1.33}$$

where the evolution of capillary pressure P_c can be obtained with the unsaturated flow model as discussed in the previous section. However, this model is only available for line elastic materials and the performance of surface energy on shrinkage is totally neglected.

2) **Coussy et al. model**

Considering that pressure caused by release of interfacial energy has non-negligible influence on shrinkage, especially for cement-based materials with low moisture content, Coussy et al [85] have introduced the concept of equivalent pore pressure π_0 in place of the average pore pressure to calculate the drying shrinkage. The value of equivalent pore pressure is the combination of average pore pressure and pressure due to the contribution of interface energy U:

$$\pi_0 = P - U \tag{1.34}$$

where U can be calculated knowing the desorption isotherm:

$$U\left(S_w\right) = \int\limits_{S_w}^{1} P_c\left(S_w\right) dS_w. \tag{1.35}$$

The specific shrinkage model is presented as follows:

$$\varepsilon_v = -\left(S_w P_c + \int\limits_{S_w}^{1} P_c\left(S_w\right) dS_w\right)\left(\frac{1}{K_b} - \frac{1}{K_s}\right). \tag{1.36}$$

3) **Vlahinić et al. model**

Vlahinić et al. [86] has provided a model, taking into account the weakening of the solid caused by desaturation, to predict the volumetric shrinkage. In their model, drying merely affects the bulk modulus of the effective solid, which means the bulk modulus of the solid skeleton K_s changes as desaturation develops. The effective bulk modulus of solid skeleton for partially saturated system is given as follows:

$$\bar{K}\left(S_w\right) = K_s - \frac{\left(K_s - K_b\right)\left(1 - S_w\right)}{\left(1 - S_w\phi_0\right)}. \tag{1.37}$$

The shrinkage model of Vlahinić et al. is an extension of Biot-Bishop model. By substituting the constant K_s with $\bar{K}\left(S_w\right)$, the constitutive formulation of Vlahinić et al. model is obtained:

$$\varepsilon_v = -S_w P_c \left(\frac{1}{K_b} - \frac{1}{\bar{K}\left(S_w\right)}\right). \tag{1.38}$$

4) **Hua et al. model**

Hua et al. [87] has introduced a macroscopic scale model for autogenous shrinkage of cement-based materials, which are regarded as continuum medium with viscoelastic aging behaviour. This behaviour is generally characterized by an empirical creep function written as follows:

$$J\left(t, t'\right) = \frac{1}{E\left(t'\right)} + \varepsilon_\infty\left(t'\right)\frac{\left(t - t'\right)^{\alpha\left(t'\right)}}{\left(t - t'\right)^{\alpha\left(t'\right)} + b\left(t'\right)}, \tag{1.39}$$

where $\varepsilon_\infty\left(t'\right)$, $\alpha\left(t'\right)$ and $b\left(t'\right)$ indicate empirical parameters determined by a series of experiments. The solid skeleton of hardening cement is macroscopically subjected to tension stress induced by capillary pressure, thus the volumetric shrinkage strain is calculated by:

$$\varepsilon\left(t\right) = \int_{t_0}^{t} (1 - 2v) J\left(t, t'\right) d\sum\nolimits^{S}\left(t'\right), \tag{1.40}$$

where $\sum^{S} = \phi P_c$ indicates macroscopic stress of the skeleton. t, t_0 and t' are current time, reference time and dummy time variable of integration, respectively. Obviously, the contribution of the release of surface energy on shrinkage is totally neglected. Hence, this model cannot be used to low moisture content condition.

5) **Grasley et al. model**

In order to calculate the volumetric free shrinkage of solidifying viscoelastic cementitious materials with intrinsic ageing accounting for both capillary as well as the interface induced pressures, Grasley et al. [88] has provided a constitutive equation as below:

$$\varepsilon\left(t\right)=\int_{0}^{t}\frac{\partial\pi\left(t^{'}\right)}{\partial t^{'}}\left(3\left(1-2\upsilon_{p}\right)J_{p}\left(t-t^{'}\right)-\frac{1}{K_{s}}\right)dt^{'}, \tag{1.41}$$

where υ_p is Poisson's ratio of the porous body; K_s is the bulk modulus of the solid phase. Similar with the model of Coussy, the equivalent pore pressure is calculated according to $\pi_0 = S_w P_w + U$. J_p is the uniaxial viscoelastic compliance of porous body, which can be calculated through the inverse Laplace transform of $\overline{J}_p$ [89]:

$$\overline{J}_{p}=\frac{1}{s^{2}\overline{E}_{p}\left(s\right)}, \tag{1.42}$$

where $\overline{J}_p$ represent the Laplace transformed uniaxial viscoelastic compliance of the porous body. s and $\overline{E}_p\left(s\right)$ indicate the transform variable and the Laplace transform of viscoelastic Young's modulus of the porous body $E_p\left(t\right)$, respectively.

These models consider quasi-static conditions for the pressure variation. In case of low moisture content, they cannot predict the strain evolution because phenomena are very complex: high energy is needed to evaporate liquid water and interfacial energy is difficult to predict due to complex capillary bridge. The relation between P_c and S_w becomes difficult to define and the quasi-static relation seems insufficient. That is the reason why some researchers have suggested to add second order terms in this relation.

1.3 Dynamic effects on capillary pressure

As mentioned previously, the difference between the air pressure and water pressure is assumed to be capillary pressure. The relationship between macroscopic capillary pressure and water saturation is a fundamental constitutive relationship for the prediction of the unsaturated water-air flow behavior in porous materials. Experimental measurement of the capillary pressure-saturation relationship is time consuming and always quantified under equilibrium condition i.e. measurements made until the transport of fluid has stopped. It is commonly assumed that the $P_c - S_w$ relationship is totally independent of the desaturation rate, however, plenty of studies indicate that this may not be the case [10, 18, 90–93]. For example, Zhuang et al. [10] have implemented water-air drainage experiments, in which capillary pressure at a given saturation, increased with the time change rate of desaturation. The specific $P_c - S_w$ relation curves measured under equilibrium (quasi-static) and dynamic conditions are plotted and compared in Fig. 1.10 and Fig. 1.11 respectively. The term 'dynamic' used in this paper is in the sense of the fluid mechanics to describe the velocity of fluids.

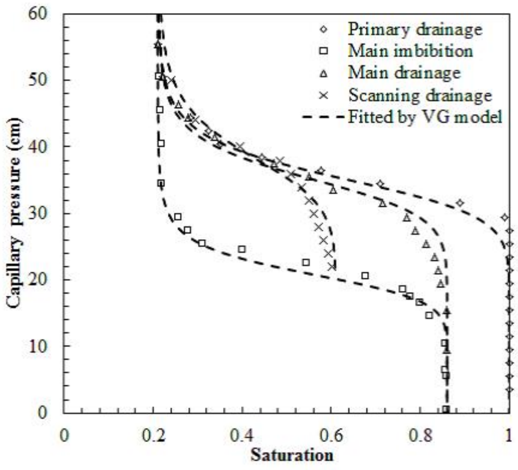

Figure 1.10: Capillary pressure-saturation curves under quasi-static conditions (figure from [9])

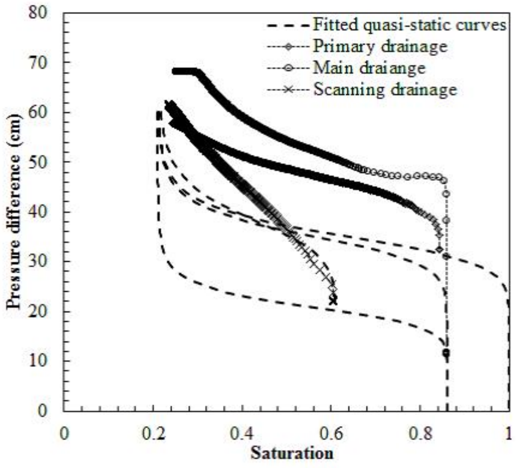

Figure 1.11: Measured pressure difference-saturation curves for dynamic primary, main and scanning drainage experiments (figure from [9])

In recent decades, many studies have focused on dynamic capillary pressure. Plenty of conceptions, models and formulas were proposed to specify this phenomenon [92, 94–96]. To account for the dynamic effects on the $P_c - S_w$ relationship, a series of relationships have been proposed to explain the observed non-uniqueness in $P_c - S_w$ relationship [92, 93, 95]. One of the generally accepted linear approximation of dynamic capillary pressure was presented in [21, 93, 95]. These studies of Hassanizadeh et al. have established a constitutive relationship for capillary pressure at macroscopic scale and developed a thermodynamic basis for the concept of dynamic effects in capillary pressure. The conception of dynamic effects coefficient was introduced into this linear approximation, which plays an extremely important role in describing dynamic capillary pressure.

1.3.1 The dynamic capillary pressure-saturation relationship

Since standard $P_c - S_w$ relationship is always given on the basis of empirical phenomena, in another words it lacks an essential theoretical foundation, it is necessary to provide a definition of macroscopic capillary pressure in the framework of thermodynamics. The macroscopic balance laws and appropriate constitutive relationship must be provided for properties of phases and interfaces of porous materials. Such a method was therefore developed and applied to the two-phase flow simulation [21, 22, 95]. The particular constitutive hypothesis is the dependence of the Helmholtz free energy functions for phases and interfaces on state variables including mass density, saturation, solid phase strain tensor, porosity, interfacial area density, etc. Interfaces are recognized to play important role in determining the thermodynamic state of the entire system. As for water-air flow in porous media, there are three phases and three interfaces. These are liquid water , air mixture and solid phase, here denoted by subscripts w, g, s. The interface is indicated by $\alpha\beta$, which could take on wg, ws and gs. According to the constitutive theory [21], the fluid pressures and capillary pressure is given as follows:

$$P_\alpha = (\rho_\alpha)^2 \frac{\partial \psi_\alpha}{\partial \rho_\alpha}, \tag{1.43}$$

$$P_c = -S_w \rho_w \frac{\partial \psi_w}{\partial S_w} + (1 - S_w)\, \rho_g \frac{\partial \psi_g}{\partial S_w} - \sum_{\alpha\beta} \frac{\gamma^{\alpha\beta}}{\phi} \left(\frac{\partial a^{\alpha\beta}}{\partial S_w} \right), \tag{1.44}$$

where $\alpha = w, g$; ψ_α is Helmholtz free energy of phase per unit mass of phase; ρ_w and ρ_g are water density and air density respectively; $a^{\alpha\beta}$ and $\gamma^{\alpha\beta}$ denote the area of $\alpha\beta$ interface per unit volume of porous media and interfacial tension of the $\alpha\beta$ interface respectively. $\sum_{\alpha\beta}$ indicates a summation over all interfaces. The Eq. (1.44) provides the capillary pressure equal to the variation in the free energy of the system caused by desaturation. Accordingly, capillary pressure gives an indication of the tendency of the system to allow a variation of water saturation as temperature, density and porosity remain constant. On the basis of this equation and taking into account that the capillary pressure is positive, the free energy of the whole system must decrease as the water saturation increases $(\Delta S_w > 0)$. Hence, the imbibition procedure is spontaneous. On the contrary, the free energy of system must increase during desaturation process $(\Delta S_w < 0)$. Therefore, this is not spontaneous. The external work must be supplemented to make the desaturation possible. Capillary pressure acts as a measure of the tendency of the porous media to experience a variation in saturation. The occurrence of this variation is dependent on initial state and boundary conditions, on the overall state of the system, and especially, on the distribution of fluid pressure. This is mathematically expressed by the residual entropy inequality. As presented in literature [21], the following combination of terms makes contribution to the entropy production. When other thermodynamic forces are neglected, the following inequality is obtained:

$$\phi \frac{D^s S_w}{Dt} \left[(P_g - P_w) - (P_c) \right] \geq 0, \tag{1.45}$$

where $D^s S_w / Dt$ denotes the material time derivative of the water saturation when transporting with solid phase. It reduces to partial time derivative $\partial S_w / \partial t$ in the absence of solid deformation. $P_g - P_w$ is the external driving force of fluid movement. This movement is opposed by capillary pressure P_c. As for equilibrium condition, $D^s S_w / Dt = 0$ and the capillary pressure P_c equals to $P_g - P_w$. However, if the equilibrium is disturbed, such as in the case $P_g - P_w > P_c$, the $D^s S_w / Dt$ should be negative according to the inequality (1.45). As for the case of $P_g - P_w < P_c$, the $D^s S_w / Dt$ is positive. The negative and positive of time derivatives of the water saturation correspond to drainage and imbibition respectively. Apparently, the faster the drainage or imbibition is, the greater the magnitude of the difference between $P_g - P_w$ and P_c. For a linear theory, the approximation for $D^s S_w / Dt$ may be provided as below [21, 22]:

$$-\phi \frac{D^s S_w}{Dt} = \tau^{-1} \left[(P_g - P_w) - (P_c) \right] \tag{1.46}$$

where τ is defined as dynamic effects coefficient, which perhaps be influenced by degree of water saturation. By replacing $D^s S_w/Dt$ in Eq. (1.45) with Eq. (1.46), the resultant $\tau \geq 0$ is obtained. Not only the inequality (1.45), but also the approximation (1.46) indicate that the water saturation tends to change locally to reach equilibrium for a given point in porous media and at any given time. In addition, the equation (1.46) suggests that the curve of $P_g - P_w$ versus S_w also depends on $D^s S_w/Dt$. The coefficient τ can be interpreted as a measure of the speed of the time change rate of water saturation. The equivalence between $P_g - P_w$ and P_c can be reached instantaneously after the disturbance at equilibrium concerning small value of τ. Consequently, τ is also interpreted as a capillary damping coefficient. If $P_g - P_w = P_c$ is used to define the macroscopic capillary pressure, it means that any disturbances at equilibrium are eliminated instantaneously. However, this only happens for high permeable porous media. As the permeability decreases, the well-known equation $P_g - P_w = P_c$ may not meet the reality. In the case of moisture transport in low permeable porous media, the equation $P_g - P_w = P_c$ is available only at condition of stable or equilibrium state. In order to predict system dynamics more precisely, the Eq. (1.46) must be employed. In addition, it should be emphasized that P_c is a hysteretic function of saturation. Therefore, the coefficient τ could also have hysteretic character that the values of τ are different between imbibition and drainage [97].

The pressure difference $P_g - P_w$ measured directly under dynamic condition (i.e., saturation experiences change) is denoted as P_c^{dyn}. On the other hand, the equilibrium capillary pressure is denoted as P_c^{stat}. Hence, as the material time derivative is replaced by partial time derivative, the Eq. (1.46) is simplified to:

$$P_c^{dyn} - P_c^{stat} = -\tau \frac{\partial S_w}{\partial t}. \tag{1.47}$$

1.3.2 The mechanisms of dynamic effects on capillary pressure

The proposed mechanisms of dynamic effects on capillary pressure include dynamic contact angles [98, 99], dynamic fluid spatial distribution [100–102], dynamic interface deformation [92, 99], and the effects of averaging homogeneous/heterogeneous flow zones [36, 103]. Here, the first two factors are discussed in detail.

1) **Dynamic contact angles**

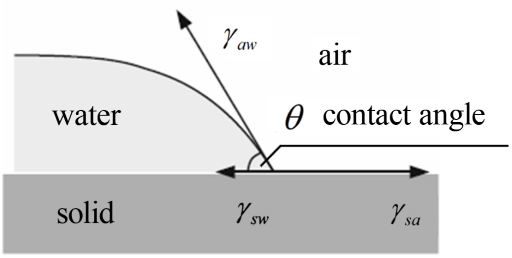

Figure 1.12: Contact angle ϕ between the water and air and surface tensions $\gamma_{\alpha\beta}$.

The static contact angle presented in Fig. 1.12 depends on the history of wetting and drainage processes, always with a larger contact angle for wetting than for drainage [104]. Therefore, the hysteresis of static contact angle is a cause of the hysteresis of the static wetting and draining water retention characteristics. Experimentally, the contact angle not only exhibit hysteresis, but also depends on fluid velocity [105]. Hoffman et al. [106] have founds that the dynamic contact angle is determined mainly by static contact angle and interaction between viscous and capillary forces. The impact of the second factor can be expressed by the capillary number Ca, which indicates the ratio between viscous and capillary forces.

$$Ca = \frac{\eta_w V}{\gamma}, \tag{1.48}$$

where η_w represents the dynamic viscosity of water, V the characteristic velocity and γ_{aw} the surface tension between water and air. Thus, according to Young-Laplace equation, the dynamic capillary pressure deviates from static capillary pressure as the velocity of fluid flow is increased.

2) **Dynamic fluid spatial distribution**

i. Entrapment of water. The water entrapment is due to hydraulic isolation of saturated pores by draining surrounding pores. The faster the drainage, the harder for all pores to drain simultaneously. It may appear throughout the porous system and would increase water retention, but unsaturated hydraulic conductivity is decreased as the mobile portion of water is decreased.

ii. Pore water blockage. As the large pressure step is applied to near-saturated soil sample, the large potential head gradient is formed, particularly close to outflow boundary. The smaller pores are drained which results in part of relatively large pores disconnected from the conductive flow paths and therefore undrained.

1.3.3 The dynamic effects coefficient

Dynamic effects coefficient τ is a very important parameter to investigate dynamic effects quantitatively and qualitatively. Both of numerical analyses [107, 108] and experimental methods [10, 23, 109, 110] were carried out to obtain more precise dynamic effects coefficient. An interesting numerical approach regarding this issue was proposed by Dahle et al. [36], who established bundle-of-tubes model for calculating dynamic effects coefficient. Concerning experimental methods, the common characteristic is that changing boundary conditions with great step in a short time [91].

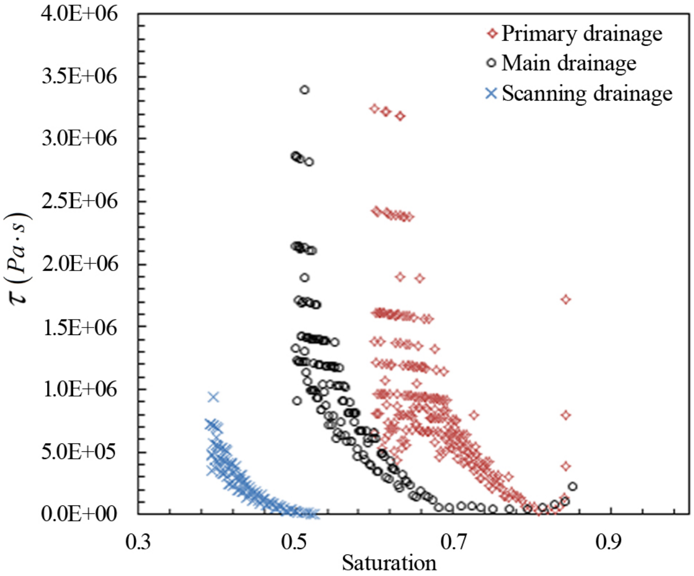

Figure 1.13: Dynamic effects coefficient for primary, main and scanning drainage [9]

Plenty of studies have indicated that τ varies with saturation [36, 90, 91, 111]. A kind of evolution for dynamic effects coefficient obtained by Zhuang et al. [9] is presented in Fig. 1.13. The relationship $\tau - S_w$ have been investigated by a number of studies, however, this functional relationship is still unclear. Different or even contradictory results are obtained for the past decades. No significant variation of τ with S_w is observed in [90]. However, large numbers of numerical and experimental studies have supported that τ increases as S_w decreases. For example, the fast drainage experiments [10, 109, 112] performed in air-water porous media have observed that τ may be expressed as a negative logarithmic function of S_w. O'Carroll [91] has proposed a negative linear relationship $\tau - S_w$ according to inverse analysis of outflow experiments. Furthermore, similar relationship has been reported in numerical studies on the basis of pore-scale [36, 108] and continuum-scale [24, 113] simulations. It should be noted that opposite trend that τ increases with increasing saturation has been reported in previous literatures [91, 109]. In addition, the investigation on dynamic effects is limited in sand and soil, few remarks are given on cement-based materials. In the next chapters, the range of τ values will be discussed for porous materials with high and low permeability.

1.4 Critical review and concluding remarks

The chapter briefly reviews the moisture transport and shrinkage for porous material, and then the dynamic effects on capillary pressure briefly.

Compared with other moisture transport models, the continuum model is the most accurate and should be the first choice. An important reason is that it is more physical for modelling moisture transport in porous media. In another words, this model is derived according to actual physical phenomena. Shrinkage is an extremely complex phenomenon. Concerning the drying shrinkage which plays significant role in entire shrinkage, a series of the constitutive models are introduced and their applicabilities are also discussed. Thereafter, the dynamic effects on capillary pressure are reviewed. It includes explicit performance and implicit mechanisms of dynamic effects.

Although different types of materials have different pore systems, it is of interest to test whether dynamic moisture transport models from soil science are also applicable to cementitious materials, as there are few studies on the dynamic effects of such materials. In addition, few remarks are given on the dynamic effects for fluid-solid interaction. Thus, it is also of interest to investigate the possible influence of dynamic capillarity effect on drying and drainage shrinkage for porous materials.

Chapter 2

Contribution of the dynamic capillary pressure on fast drainage of quite permeable porous materials

2.1 Background

As a negative tension, capillary pressure is supposed to be the main cause of shrinkage during drainage in porous materials [16, 114]. These deformations are often the cause of the occurrence of micro-cracks and must be mastered [115]. To predict these risks, experimental procedures and highly sophisticated models have been developed by researchers around the world. Probabilistic laws are defined regarding experiments so as to predict the risk, and models are proposed to approach real phenomena based on physical relationships. However, differences are observed between numerical results and experimental results, owning to a phenomenon little known: the dynamic effects on the capillary pressure (difference between the pressure of two fluids) when the saturation in porous media experiences a fast change [21]. Under dynamic condition, the viscous forces are non-negligible and needs additional pressure gradient to overcome. The pressure difference between gas mixture and liquid water may deviate from the initial static capillary pressure and it can be measured [10, 19, 93, 101, 116–118]. The dynamic effects on capillary pressure are not exactly identical with hysteresis which is caused by ink-bottle effect, the variation of liquid-solid contact angle and the pore-size distribution and pore connectivity [38, 119]. Indeed, dynamic effects are greatly dependent on time rate of change of water saturation [22, 120].

In recent decades, many researches have focused on dynamic capillary pressure. The capillary pressure is the driving force for unsaturated water-air flow. Thus the dynamic effects on unsaturated flow become a research focus. Goel et al. [23] analyzed the dynamic effects in the capillary pressure–saturation relationship and its impacts on unsaturated flow. Fučík et al. [24] presented the significance of dynamic capillarity effect in heterogeneous porous materials. Cao and Pop obtained the result for the two-phase flow model with the consideration of dynamic capillarity effect [25]. A dynamic pore-network model of air-water flow with phase change has been developed to analyze dynamic effects [121]. Meanwhile, the mathematical analyses are developed in dynamic capillary pressure models. A great contribution was done by Mikelić et al. [122] who investigated the pseudoparabolic equation which describes unsaturated flows in porous media with dynamic capillary pressure–saturation relationship. Furthermore, Bouadjila et al. [123] proposed a finite volume scheme to approximate the two incompressible phase flow with dynamic capillary pressure.

However, these well-developed dynamic capillary pressure theories were not applied to skeleton deformation. To the authors' best knowledge, very few publications are available in the literature taking into account the influences of dynamic capillary pressure on skeleton deformation. It is well known that capillary pressure is a kind of tension causing deformation of porous media, while most of models predicting the shrinkage phenomenon of porous media are based on the quasi-static behaviour laws. Shahbodagh-Khan et al. [124] put forward a numerical model for nonlinear large deformation analysis of unsaturated porous media. Zhou et al. [125] introduced an enhanced hydraulic model to describe the hydro-mechanical interaction in terms of the degree of capillary saturation, etc. The common feature of these models and methods is that the dynamic effects on capillary pressure were totally neglected.

Considering little investigation has been carried out for dynamic capillarity effect on solid skeleton deformation of soils and sands. It is crucial to establish a coupled model between unsaturated water-air flow and deformation of soils and sands with the consideration of dynamic effects. In this chapter, a particular approach based on traditional quasi-static coupled model is proposed firstly to generate the coupled dynamic model. The deduction of dynamic coupled model is divided into two parts: (i) unsaturated water-air flow with dynamic skeleton deformation; (ii) solid deformation with dynamic capillary pressure. In part one, Richards' equation governs the air-water transport. In part two, principle of effective stress is adopted to investigate the evolution of solid deformation. Thereafter, a documented experiment of drainage from a sandbox has been employed to validate the proposed model. Modelling with inverses analysis method has been inspected through comparisons with experimental results for verification. Modelling results based on dynamic effects and non-dynamic effects have been compared. Moreover, further discussion of the proposed model have been implemented by simulating a fictitious drainage experiment.

2.2 Governing model for unsaturated water-air flow in deforming porous materials

The aim of this chapter is to impose the dynamic effects on the coupling of unsaturated water-air flow and skeleton deformation for soils and sands which are porous materials with relative high permeability. As presented in Fig. 2.1, water movements governed by fluid mechanics result in a rapid change in capillary pressure. The skeleton deformation, governed by capillary pressure, leads to the changes of pore size and permeability, which in turn affects the unsaturated fluid flow. When dynamic effects are considered in capillary pressure, the interaction should be further developed between unsaturated air-water flow and skeleton deformation. In this section, the derivation of the coupled dynamic model is presented in detail. Constant temperature and local thermodynamic equilibrium are assumed throughout the present research.

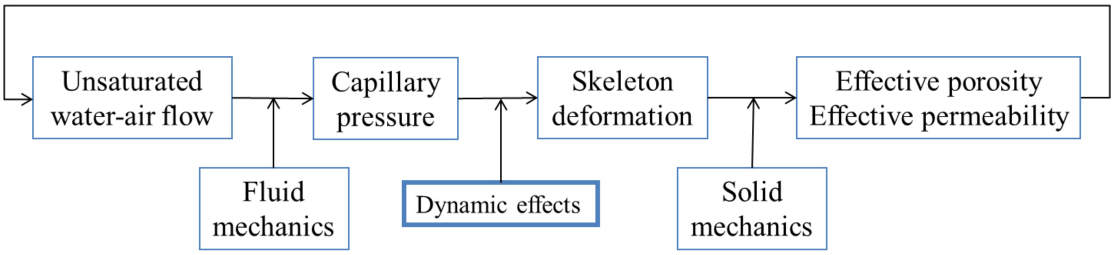

Figure 2.1: Schematic diagram of coupling principle

2.2.1 Physical model for unsaturated water-air flow from standard to dynamic

The evolution of unsaturated water-air flow in porous media is governed by the mass conservation and extended Darcy's law. Initially, the dynamic effects on water transport are excluded. Supposing that the phase transition and the gas mixture diffusion were neglected, the mass conservation for water and the air is written as follows:

$$\frac{\partial\left(\phi S_w \rho_w\right)}{\partial t}+\nabla\cdot\left(\rho_w V_w\right)=0, \tag{2.1}$$

$$\frac{\partial\left[\phi(1-S_w)\,\rho_g\right]}{\partial t}+\nabla\cdot\left(\rho_g V_g\right)=0, \tag{2.2}$$

where ϕ represents the Eulerian porosity, ρ_w and ρ_g the density of water and air respectively, V_w, V_g the velocity of liquid water and gas mixture and S_w the saturation of water.

In terms of quite permeable porous media, it can be assumed that the air phase is continuous in the pore space and that it is connected to the atmosphere [58]. It is well known that the air viscosity is about 55 times smaller than the water viscosity at room temperature, which means that if the relative permeability of both fluids are similar, the air mobility is greater than the water mobility by approximating the same factor. As a result, any pressure difference in the air phase is in balance faster than that in the water phase. When the variations in the atmospheric pressure are neglected, the pore air is considered at a constant atmospheric pressure [2].

The capillary pressure P_c is a discontinuity in pressure across the interface between non-wetting and wetting phase. Its value is equal to the difference between gas mixture pressure P_g and liquid water pressure P_w. The reference atmospheric pressure is often assumed to be zero. Hence:

$$P_c=P_g-P_w=-P_w. \tag{2.3}$$

When considering the coupling between fluid flow and the deformation of the skeleton, the actual fluid velocity should be rewritten as the extended Darcy's velocity plus the average skeleton velocity $\phi S_w(\partial u/\partial t)$ as follows:

$$V_w=-\frac{kk_{rw}}{\eta_w}(\nabla P_w-\rho_w g)+\phi S_w\frac{\partial u}{\partial t}, \tag{2.4}$$

where k represents the intrinsic permeability, k_{rw} the relative water permeability, η_w the water viscosity, g the gravity acceleration and u the displacement of the solid matrix. Since the air in the porous media is supposed to be constant and equals to atmospheric pressure, the governing equation for air-water flow comes down to Richards' equation. Substituting Eq (2.4) into Eq (2.1) and taking into account Eq (2.3) gives:

$$\frac{\partial(\rho_w \phi S_w)}{\partial t} + \nabla \cdot \left[\rho_w \left(-\frac{kk_{rw}}{\eta_w}(-\nabla P_c - \rho_w g) + \phi S_w \frac{\partial u}{\partial t}\right)\right] = 0. \tag{2.5}$$

As mentioned previously, the effective porosity is not constant and varies with the deformation of the porous medium. Based on the definition of Eulerian porosity, the effective porosity is expressed by:

$$\phi = \frac{d\Omega - d\Omega^s}{d\Omega} = 1 - \frac{d\Omega_0^s + \Delta d\Omega^s}{d\Omega_0 + \Delta d\Omega} = 1 - \frac{d\Omega_0^s\left(1 + \Delta d\Omega^s / d\Omega_0^s\right)}{d\Omega_0\left(1 + \Delta d\Omega / d\Omega_0\right)}, \tag{2.6}$$

where $d\Omega_0$represents the initial whole volume, $d\Omega$ the current whole volume, $d\Omega_0^s$ the initial matrix volume, $d\Omega^s$the current matrix volume and Δ the differential symbol. When matrix is considered to be incompressible, specifically $\Delta d\Omega^s / d\Omega_0^s$ is much less than one along with $\Delta d\Omega / d\Omega_0 = \varepsilon_v$, the effective porosity can be obtained as:

$$\phi = \frac{\phi_0 + \varepsilon_v}{1 + \varepsilon_v}, \tag{2.7}$$

where ϕ_0 represents the initial porosity and ε_v the volumetric strain. Moreover, shrinkage or swelling of the porous medium not only affects the porosity, but also changes the intrinsic permeability. The classical Kozeny-Carman (KC) equation [126] is employed to describe the porosity-permeability relation. In the unmodified KC equation, to achieve the present permeability, only the calculation of the initial and present porosity is required [127].

$$k = k_0 \frac{\phi^3}{(1-\phi)^2} \frac{(1-\phi_0)^2}{{\phi_0}^3}, \tag{2.8}$$

where k_0 is the initial intrinsic permeability. Additionally, the compressibility of water is assumed negligible in this study. Therefore, the spatial gradients and time derivative of water density are zero. It leads the storage term written as follows:

$$\frac{\partial(\rho_w \phi S_w)}{\partial t} = \rho_w \phi \frac{\partial S_w}{\partial P_c} \frac{\partial P_c}{\partial t} + \rho_w S_w \frac{\partial \phi}{\partial t}. \tag{2.9}$$

It converts the differential of saturation versus time into the product of differential of pressure versus time and moisture capacity. Moreover the van Genuchten and the Brooks-Corey formulas, presented in Eq. (2.11)-(2.13) and Eq. (2.14)-(2.16) respectively, are typical retention models used widespread to link effective saturation with capillary pressure and also specify the relative permeability k_{rw} and moisture capacity $\partial S_w/\partial P_c$ by capillary pressure or water saturation. The effective saturation S_e is defined as:

$$S_e = \frac{S_w - S_w^{ir}}{1 - S_w^{ir}}, \tag{2.10}$$

where S_w^{ir} is the irreducible water saturation. It means all the other variables for unsaturated flow can be expressed by the only variable water pressure. With the van Genuchten equations [128], the porous medium is considered saturated when fluid water pressure is equal to atmospheric pressure.

$$S_e = \begin{cases} 1/[1 + |\varphi H_w|^n]^m & H_w < 0 \\ 1 & H_w \geq 0, \end{cases} \tag{2.11}$$

$$\frac{\partial S_w}{\partial P_c} = \begin{cases} \frac{\varphi m}{(m-1)\rho_w g} {S_e}^{1/m} \left(1 - {S_e}^{1/m}\right)^m & H_w < 0 \\ 0 & H_w \geq 0, \end{cases} \tag{2.12}$$

$$k_{rw} = \begin{cases} {S_e}^l \left[1 - \left(1 - {S_e}^{1/m}\right)^m\right]^2 & H_w < 0 \\ 1 & H_w \geq 0, \end{cases} \tag{2.13}$$

where φ, n, m represent parameters related to the pore-size distribution and H_w is the water pressure head which is given as $H_w = \frac{P_w}{\rho_w g}$. The relationship between m and n is $m = 1 - 1/n$. l is the pore connectivity parameter. All those parameters specify a particular type of porous medium. With Brooks-Corey formulas [129], an air-entry pressure head ($H_{ce} = 1/\varphi$) distinguishes saturated ($H_w \geq -1/\varphi$) and unsaturated ($H_w < -1/\varphi$) porous media.

$$S_e = \begin{cases} 1/|\varphi H_w|^n & H_w < -1/\varphi \\ 1 & H_w \geq -1/\varphi, \end{cases} \tag{2.14}$$

$$\frac{\partial S_w}{\partial P_c} = \begin{cases} \frac{n}{\rho_w g H_w} \frac{1}{|\varphi H_w|^n} & H_w < -1/\varphi \\ 0 & H_w \geq -1/\varphi, \end{cases} \tag{2.15}$$

$$k_{rw} = \begin{cases} {S_e}^{2/n+l+2} & H_w < -1/\varphi \\ 1 & H_w \geq -1/\varphi. \end{cases} \tag{2.16}$$

Therefore, the Eq. (2.5) is rewritten as Eq. (2.17) which describes transient water flow under unsaturated conditions and is called coupled Richards' equation:

$$\phi \frac{\partial S_w}{\partial P_c} \frac{\partial P_c}{\partial t} + \nabla \cdot \left[\frac{k k_{rw}}{\eta_w} \left(\nabla P_c + \rho_w g \right) \right] = -\nabla \cdot \left(\phi S_w \frac{\partial u}{\partial t} \right) - S_w \frac{\partial \phi}{\partial t}. \tag{2.17}$$

On the other hand, dynamic capillarity effect, observed in lab experiments, has non-negligible influence on unsaturated water-air flow in porous media under certain conditions. Experimental evidence has gradually accumulated in the past decades to support a more general and precise description of dynamic capillary pressure [6]. The pressure difference between gas and liquid water is a commonly measured quantity denoted as dynamic capillary pressure P_c^{dyn}, and the equilibrium (or 'static') capillary pressure is denoted as P_c. A well accepted expression Eq. (2.18), proposed by [21], defines the relationship between dynamic and static capillary pressure:

$$P_c^{dyn} - P_c = -\tau \frac{\partial S_w}{\partial t}. \tag{2.18}$$

Since the eference atmospheric pressure is assumed to be zero as discussed previously, then $P_c^{dyn} = -P_w^{dyn}$, consequently:

$$P_w^{dyn} = -P_c + \tau \frac{\partial S_w}{\partial t}, \tag{2.19}$$

where P_c is a given function with respect to S_w defined by Eq. (2.11) or Eq. (2.14).

The parameter τ, the dynamic effects coefficient, is a measure of the magnitude of dynamic effects on measured capillary pressure. Most previous studies suggest that τ is dependent on intrinsic permeability, pore connectivity and effective saturation [22, 93, 120]. Several authors also have demonstrated the scale-dependence of dynamic effects [23, 34]. Several studies have been done by Hassanizadeh [22] to calculate approximate value of τ. However, despite the similarities in the porous media and fluids used, values ranged from 3×10^4 $Pa \cdot s$ to 5×10^7 $Pa \cdot s$ with a range of more than three orders of magnitude. It is also hard to find consistency between different studies in terms of the effect of system properties (fluids, porous media) on magnitude of τ, how τ varies with saturation, or how it differs between drainage and imbibition [100, 109, 130]. An empirical relationship suggested by Stauffer [93] is shown as below:

$$\tau = \frac{a \phi \eta_w}{k n} (H_{ce})^2, \tag{2.20}$$

where a is assumed to be constant and equal to 0.1 for all types of soils, H_{ce} and n represent coefficients in the Brooks-Corey formula. Although this empirical formula proved to be limited, we can at least estimate the preliminary value of dynamic effects coefficient. If this empirical relationship is applied to approximate τ for porous media specified by van Genuchten retention model, it is necessary to find a method to convert the van Genuchten parameters to Brooks-Corey parameters. At first, Corey [129] defined a new parameter p by incorporating Brooks-Corey parameter n:

$$p = 3 + 2/n. \tag{2.21}$$

The equivalence between Brooks-Corey and van Genuchten parameters is defined based on two criteria. (i) the effective capillary drive must be preserved; (ii) the asymptotic behaviour of capillary pressure versus water content should be preserved at low water contents, i.e. the functional dependence on saturation close to zero should be the same. This second condition requires that the parameters p and m are linked by the formula $m = 2/(p-1)$ (see [131] for more details). It means that Brooks-Corey parameter n can be defined by van Genuchten parameter m presented as $n = 1/m - 1$. Furthermore, when van Genuchten parameters φ and m are known, p can be calculated from the above equation and then H_{ce} can be calculated from the following formula [131]:

$$H_{ce} = \left(\frac{1}{\varphi}\right) \frac{(p+3)}{2p\,(p-1)} \left(\frac{127.8 + 8.1p + 0.092p^2}{55.6 + 7.4p + p^2}\right). \tag{2.22}$$

From the discussion above, the empirical equation not only can be applied to materials following Brooks-Corey retention model, but also is useful for materials that satisfy van Genuchten retention model. However, this empirical formula proved to be limited, we can only estimate the preliminary value of dynamic effects coefficient. As described previously, τ can be defined as a functional dependency on S_w. Here, the τ is assumed to be a high order function of saturation as

$$\tau = \sum_{i=1}^{N} q_i {S_w}^{i-1}, \tag{2.23}$$

where q_i is the fitting parameters and will be discussed in detail later.

In the case of modelling with dynamic capillarity effect, The dynamic water pressure P_w^{dyn} should be used to replace the static water pressure P_w in unsaturated water-air flow model.

Taking the dynamic effects into account, the dynamic Darcy's velocity of water is written as follows:

$$V_w = -\frac{kk_{rw}}{\eta_w}\left[\nabla\left(-P_c + \tau\frac{\partial S_w}{\partial t}\right) - \rho_w g\right] + \phi S_w \frac{\partial u}{\partial t}. \tag{2.24}$$

Submitting the above relation Eq (2.24) to standard governing equation to replace the initially corresponding relation Eq (2.4), leads to the dynamic coupled model for unsaturated water-air transport:

$$\begin{aligned} \phi\frac{\partial S_w}{\partial P_c}\frac{\partial P_c}{\partial t} + \nabla\cdot\left[-\frac{kk_{rw}}{\eta_w}\left(-\nabla P_c - \rho_w g\right)\right] = \\ -S_w\frac{\partial \phi}{\partial t} - \nabla\cdot\left(\phi S_w\frac{\partial u}{\partial t}\right) + \nabla\cdot\left[\frac{kk_{rw}}{\eta_w}\nabla\left(\tau\frac{\partial S_w}{\partial t}\right)\right]. \end{aligned} \tag{2.25}$$

Three additional terms on the right hand side of the Eq. (2.25) are held. The first term explains the influence caused by the porosity change on unsaturated flow. The second term describes the effect of skeleton displacement on unsaturated flow. In fact, the existing of these two terms is due to skeleton deformation. The last term of Eq. (2.25) represents the contribution of dynamic capillarity effect. It directly demonstrates the influence of dynamic capillarity effect on air-water transport.

2.2.2 Dynamic physical model for the deformation of solid skeleton

The concept of effective stress $\sigma_{ij}^{'}$ is used to characterize the mechanical behaviour of unsaturated porous media. It incorporates the impact of external load σ_{ij}, as well as the average pore pressure P_{ave}, into a single term, defined as below [82, 83]:

$$\sigma_{ij}^{'} = \sigma_{ij} - bP_{ave}\delta_{ij} \tag{2.26}$$

where $\sigma_{ij}, \sigma_{ij}^{'}, \delta_{ij}$, b, represent total stress tensor, effective stress tensor, Kronecker delta symbol and Biot's coefficient respectively. Here, the positive values of stress and pore pressure denote compression. As found in research [82], parameter $b = 1 - K_b/K_s \leq 1$, where K_b is the drained bulk modulus of the porous body and K_s is the bulk modulus of its solid or the grain. $P_{ave} = (1 - S_w)\, P_g + S_w P_w$ indicates average pore pressure which consists of water pressure P_w and air pressure P_a. Capillary pressure P_c, a negative tension, causes shrinkage for porous media. As for partially saturated porous media, capillaries form at the water-air interface and govern the pore pressure. The absolute value of water pressure rapidly exceeds the atmospheric pressure during the process of drainage i.e. $|P_g| \ll |P_w|$. Thus, ignoring the contribution of the gas pressure and recalling the definition of static capillary pressure $P_c = P_g - P_w$, the effective pore pressure reduces to $P_{ave} = -S_w P_c$. If the infinitesimal displacement condition is satisfied, the stress-strain relationship for porous media is presented as below:

$$\sigma_{ij}^{'} = D_{ijkl}\varepsilon_{kl}, \tag{2.27}$$

where D_{ijkl} is the fourth-order stiffness tensor of the given materials, ε_{kl} the second-order tensor describing the strain induced by effective stress. Here the isotropic and linear elastic materials are used as an example to present the derivation of dynamic physical model. The stress–strain equation for this kind of material is simplified as follows:

$$\sigma_{ij} + (1 - K_b/K_s)S_w P_c \delta_{ij} = 2\mu_b \varepsilon_{ij} + \lambda_b \varepsilon_v \delta_{ij} \tag{2.28}$$

where μ_b and λ_b are known as Lame's moduli of dry media. μ_b is also called the shear modulus. ε_{ij} indicates strain tensor defined as $\varepsilon_{ij} = \left(\partial u_i/\partial x_j + \partial u_j/\partial x_i\right)/2$ and ε_v is volumetric strain defined as $\varepsilon_v = \varepsilon_{xx} + \varepsilon_{yy} + \varepsilon_{zz}$.

The pore pressure only has effect on normal strains on the basis of constitutive Eq. (2.28). Hence, only volumetric deformation could be caused by pore pressure. Therefore, in the absence of any externally deviatoric stress loads and taking into account of the existing relation between bulk modulus and Lame‘s modulus i.e. $K_b = (2\mu_b + 3\lambda_b)/3$, constitutive law Eq. (2.28) reduces to:

$$\varepsilon_v = \frac{\overline{\sigma}}{K_b} + S_w P_c \left(\frac{1}{K_b} - \frac{1}{K_s}\right), \tag{2.29}$$

where $\overline{\sigma} = \left(\sigma_{xx} + \sigma_{yy} + \sigma_{zz}\right)/3$ is volumetric stress. Moreover, in the absence of any external loads, the drying shrinkage model Eq. (2.29) reduces to Eq. (2.30).

$$\varepsilon_v = S_w P_c \left(\frac{1}{K_b} - \frac{1}{K_s}\right). \tag{2.30}$$

In this work, we focus on dynamic capillarity effect, and strictly deal with the contribution of dynamic capillary pressure on skeleton deformation. For simplicity, the grains forming the matrix is assumed to be rigid, leading to $K_s \to \infty$. Moreover, the contribution of the interface energy is also neglected. submitting dynamic capillary pressure Eq. (2.18) to substitute the corresponding standard capillary pressure in Eq. (2.30), the dynamic model for predicting skeleton shrinkage is achieved:

$$\varepsilon_v = S_w \left(P_c - \tau \frac{\partial S_w}{\partial t} \right) \left(\frac{1}{K_b} \right) \tag{2.31}$$

The equilibrium equation which governs the solid deformation without neglecting body force ρb_i is given as follows:

$$\sigma_{ij,j} + \rho b_i = 0 \tag{2.32}$$

Until now the fluid-solid interaction model, which takes into account dynamic capillarity effect for unsaturated water-air flow and mechanical behavior of porous media, has been attained.

2.3 Presentation of the numerical test

As introduced previously, no existing literature considers a problem of coupling between unsaturated flows and deforming porous media with dynamic effects accounted and no experiment has been performed. Based on the analysis of characteristics of the existing experiments, a documented water drainage experiment from a sand box [6] is chosen as the most appropriate example to validate the innovative numerical model proposed in this chapter.

2.3.1 Dynamic drainage test of a sandbox

The physical experiment of dynamic drainage test [10] consists of a custom-built Plexiglas sandbox packed with sand. The height, length and width of the sandbox are 3 cm, 3 cm and 2 cm respectively. In the dynamic drainage test, the air pressure keeps constant and equals to atmospheric pressure. There is no water inflow at the top of sandbox and the drainage occurs at the bottom where a hydrophilic nylon membrane acts as a capillary barrier to the air phase. The specific schematic representation of sand drainage is presented in Fig. 2.2. The initial saturation of the sample is 0.83. The dynamic drainage experiment begins by decreasing the bottom boundary water pressure to $-70\ cm$ immediately. There is no applied gas pressure. The gas pressure keeps constant at atmospheric pressure. No vertical load is imposed on

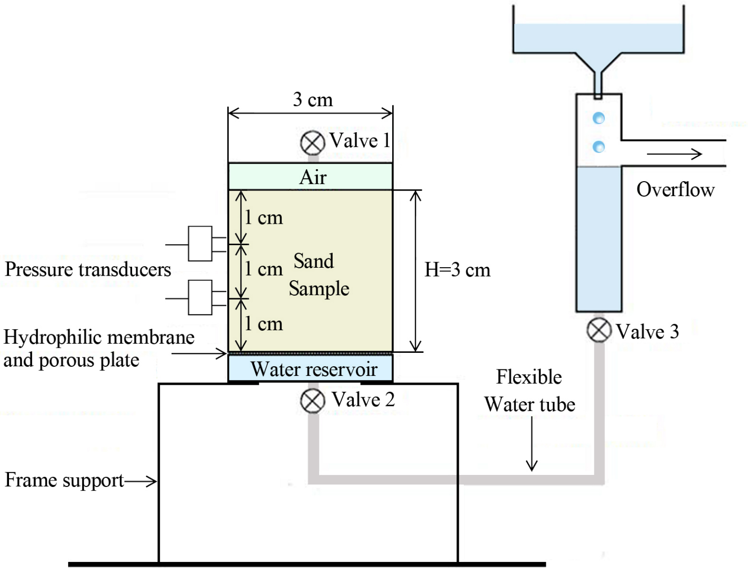

Figure 2.2: Schematic representation of sand drainage [10]

the top. On the lateral walls and at the bottom of the sandbox no deformation occurs. All experiments were conducted in a stable temperature at $T = 21 \pm 0.5\ ^0C$. Even though the precise data for mechanical properties of the sand sample are unknown, their approximations have been obtained based on mechanical behaviour of similar sand. The data related to effective saturation-capillary pressure relation were collected from experiment measurement directly, and fitted according to van Genuchten model to determine parameters φ and m. The fitting curve is presented in Fig. 2.3. All values used for the numerical simulation are summarized in table 2.1.

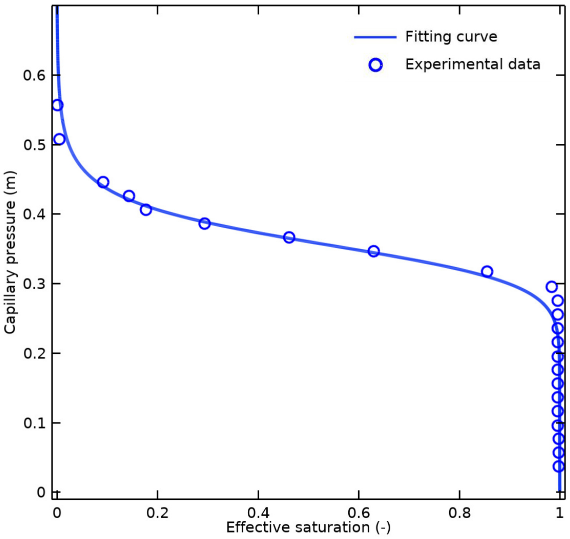

Figure 2.3: Van-Genuchten model fitting for sand sample

Table 2.1: Properties of the material used in experiment

Parameter	Value
Young's modulus of sand	$E = 1.3\ MPa$
Poisson ratio of sand	$v = 0.4$
Intrinsic porosity of sand	ϕ=0.39
Density of wet sand	$\rho_s = 2000\ kg/m^3$
Water density	$\rho_w = 1000\ kg/m^3$
Water viscosity	$\eta_w = 1 \times 10^{-3}\ Pa \cdot s$
van Genuchten coefficient	$n = 12$
van Genuchten coefficient	$\varphi = 2.8\ m^{-1}$
Inrreducible water saturation	$S_w^{ir} = 0.14$
Gravitational acceleration	$g = 9.82\ m/s^2$

2.3.2 Modelling method

To obtain quantitative solutions for the proposed model, appropriate numerical algorithm has to be chosen. The governing equations are discretized in space by Finite Element Method and in time by an implicit time-stepping method which is backward Euler method. The Galerkin method is used to get access to a weak form of the governing equations. The backward Euler method guarantees the stability of the scheme. Furthermore, given the small scale of the system, the up-scaled change rate of saturation instead of the local one is used to evaluate the dynamic capillary pressure. To solve the governing equations efficiently, the time step is flexible according to the convergence rate. The detail procedure of spatial and time discretization is analogous to that of the governing model introduced in the next chapter, which have been discussed in detail in Appendix.

A two-dimensional plain strain hypothesis has been employed. As presented in Fig. 2.4, the simulation is carried out using uniform mesh of 900 rectangle elements for analysis.This mesh is sufficiently high to optimize the computing time and give stable results.

To simulate the fast drainage process, however, two important parameters are still absent, including the intrinsic permeability (or hydraulic conductivity) and dynamic coefficient.The

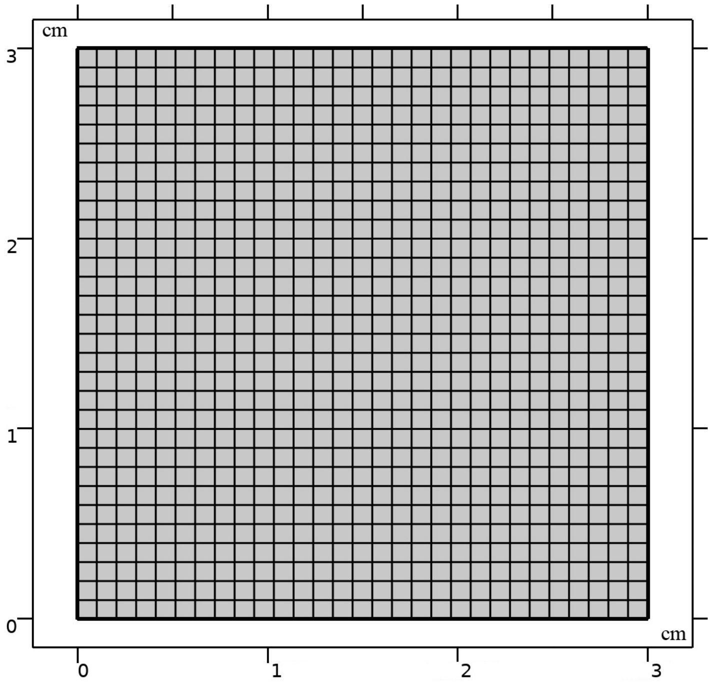

Figure 2.4: Schematic representation of mesh

water drainage occurs at the bottom of the sand sample. This process also is mainly influenced by hydrauphilic nylon membrane, porous holders, and also the interaction between porous media and the surrounding water reservoir. The water gradient, observed in the water in the vicinity of the bottom of porous media, governs the water transport from the interior of the porous media to its bottom and finally go through the membrane. The Neumann-type boundary condition, which takes this given gradient into account, is a feasible choice. The term W is mass flux of water and $W = R_b\,(P_w^o - P_w^e)$. P_w^0 is water pressure within the porous media near the membrane. P_w^e is the external water pressure within water reservoir. The water drainage between the ambient water reservoir and the porous media is mainly governed by conductance R_b and its value equals to 5×10^{-5} $\left(\frac{kg}{Pa \cdot s \cdot m^2}\right)$ based on characteristics of membrane and porous plate holders. As for k_0 and τ, both of them can be determined by inverse analysis that fits the water pressure curves and the saturation curves from the drainage experiment. The Levenberg-Marquardt (LM) algorithm is applied to parameter optimization. After that, to emphasize the significance of dynamic capillarity effect on the unexpected skeleton deformation and water drainage, both of standard and dynamic physical model are employed to simulate this identical drainage experiment.

2.4 Results analysis

2.4.1 Calibration of the dynamic coefficient

To evaluate the availability of the coupled dynamic model, this proposed model is implemented to simulate the documented drainage experiment. Dynamic capillarity effect is positively relevant to the time change rate of water saturation $\partial S_w/\partial t$. Obviously, a faster drainage in porous media leads to stronger dynamic effects on capillary pressure. If the dynamic capillarity effect is ignored, the modelling could not reproduce the observed experiment phenomenon when the boundary condition experiences rapid change. The recorded experimental results including evolution of water pressure at point with height $H = 2\ cm$ and evolution of average saturation of the whole sand sample are adopted to inversely determine the intrinsic permeability k_0 (or hydraulic conductivity) and dynamic coefficient τ. As for dynamic coupled model, dynamic coefficient τ plays an important role for drainage process.

As introduced previously, the existing literatures of dynamic effects researches reveal that τ ranges from $3 \times 10^4\ Pa \cdot s$ to $1 \times 10^{10}\ Pa \cdot s$ for most soil and sand. However, the evolution of τ is extremely complicated. Even though in the original article [10] the authors suggest that τ values increase almost log-linearly as saturation decreases within a certain saturation range, until now there is no well-accepted formula to predict them precisely. Thus, it is significant to estimate the value of τ by inverse analysis method. The precise value of τ is difficult to calculate. We note that we only did preliminary optimizations for τ here. Based on previous literatures [9,15,16,49] and the characteristics of higher order polynomial, the τ is assumed to follow a polynomial function of saturation as $\tau = \sum\limits_{i=1}^{N} q_i {S_w}^{i-1}$. when $N = 1$, the τ values are constant, independent of saturation. when N increase to 2, it presents that τ values increase linearly as saturation decreases. As the order of polynomial N increases, more number of fitting parameters q_i develop, which permit higher flexibility to optimize τ.

The following fitting procedure is employed. The parameters k_0 and q_i are calibrated step by step. In the first step, we let $N = 1$ fit the measured water pressure and average saturation of the drainage experiment by adjusting all parameters ensemble. If the experimental data are not properly fitted by simulated results, the N increases to the next number and repeat the fitting procedure. Until a good approximation of the experimental results is obtained by coupled dynamic modelling, this iterative procedure is stopped and the fitting parameters achieved. Finally, when N reaches to 5, which leads to $\tau = q_5 S_w^4 + q_4 S_w^3 + q_3 S_w^2 + q_2 S_w + q_1$, the expected fitting results are obtained. In this way, the values of these five parameters q_i for dynamic coefficient and parameters k_0 are adjusted. The specific values are collected in Table 2.2.

Table 2.2: Fitting results of Parameters

Parameters	k_0 (m^2)	q_5 (10^8)	q_4 (10^8)	q_3 (10^8)	q_2 (10^8)	q_1 (10^8)
Values	2.37×10^{-12}	4.70	-13.92	15.54	-7.80	1.50

The evolution of dynamic coefficient τ is presented and compared with the experimental and fitting results of authorship in Fig. 2.5. Obviously, the τ evolution obtained by simulation has a better agreement with the experimental results compared with log-linear model proposed in [10] as saturation decreased to a certain value. Also, the values obtained from simulations are in the order range that given in [111] which have supposed that τ is in the range between 1×10^1 $Pa \cdot s$ and 1×10^5 $Pa \cdot s$ by considering uncertainties of micro-sensors in experiments.

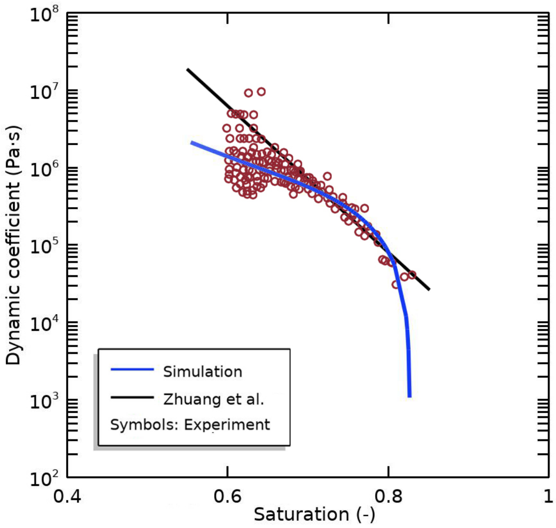

Figure 2.5: Comparison of dynamic coefficient simulated by inverse analysis with experimental and fitting results of authorship in [10]

2.4.2 Analysis of the cross effects between deformation and dynamic pressure

In Fig. 2.6 and Fig. 2.7 the simulated saturation and water pressures curves obtained from the dynamic coupled modelling are plotted and compared with the experimental measurements and corresponding results of standard modelling, respectively.

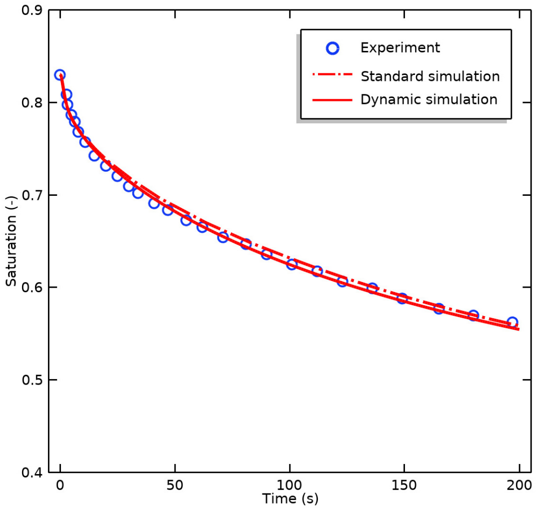

Figure 2.6: Comparison of simulated average water saturation with measured data for sand sample

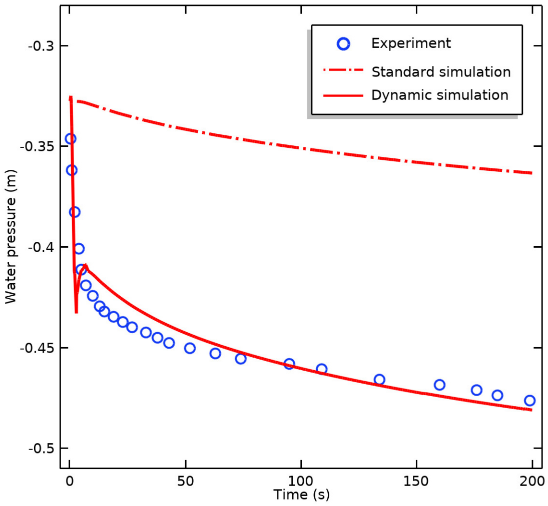

Figure 2.7: Comparison of simulated water pressure with measured data for sand sample

In general, the fitting results are quite good. For average saturation, the results of dynamic and standard modelling are almost identical and close to experimental data with coefficients of determination R^2 close to 1 (see Fig. 2.6). However, the dynamic effects lead the dynamic water pressure to evidently depart from standard water pressure. Even though the predicted dynamic water pressure curve display a slight discrepancy with the measured curve that there is a pressure overshoot observed at the beginning of dynamic modelling (see Fig. 2.7), dynamic coupled model still provides high agreements with measured data. Indeed, this non-monotonic behaviour has been observed in other drainage tests [10, 90], and also evidenced by documented simulations [132, 133]. The observed difference between simulated and experimental water pressure could be attributed to a potential reason that the relative permeability-saturation relationship is not independent and derived from the initial capillary pressure-saturation relationship. However, a constitutive relationship defined under steady-state conditions cannot be applied to transient flow procedures. Nonetheless, we strictly deal with the dynamic effects within the capillary pressure and ignore possible dynamic effects in the relative permeability curves. The detailed evolutions of water saturation and dynamic water pressure are presented in Fig. 2.8 and Fig. 2.9 respectively.

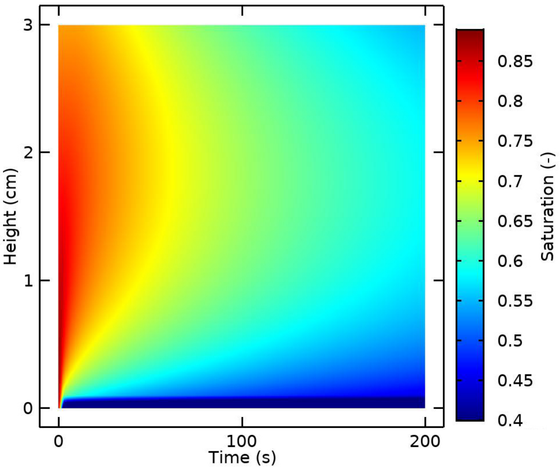

Figure 2.8: Water saturation as a function of height and time

The vertical displacement simulated by dynamic deformation model are plotted and compared with corresponding results from standard deformation modelling in Fig. 2.10. In general, both of dynamic and standard modelling deformations increase gradually from bottom to top surfaces. As drainage continues, the negative tension capillary pressure increases. Thus, the vertical displacement also enlarges as time goes by. However, a non-negligible deviation between results of dynamic and standard modelling is observed. Vertical displacement derived from dynamic model is always greater than that derived from

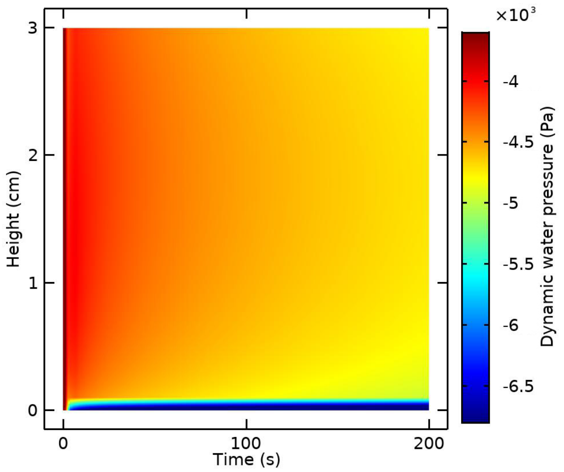

Figure 2.9: Water pressure as a function of height and time

standard model at identical time points. It reveals that dynamic effects have a significant impact on mechanical behaviour for porous media. The additional deformations caused by dynamic effects should not be neglected in predicting the risk of porous media especially when the porous material is exposed to a rapidly changing surrounding condition. The observed phenomenon in numerical simulation is consistent with the proposed dynamic model Eq. (2.31) in which the additional term $\tau\frac{\partial S_w}{\partial t}$ caused by dynamic capillarity effect indicates that volumetric shrinkage is a dependency on time change rate of saturation.

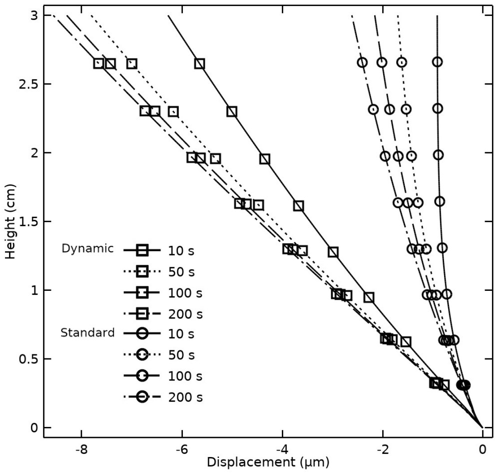

Figure 2.10: Comparison of vertical displacement between dynamic and standard modelling

However, it also notices that the absolute deformations of dynamic and standard modelling are limited and their influences on factors that governs drainage process, such as porosity and permeability, are negligible. As shown in Fig. 2.11, both average porosity of dynamic modelling and standard modelling values almost keep constant at the intrinsic value 0.39

during the whole drainage process. Indeed, the proposed model can handle porous media experience significant shrinkage. We are going to simulate a fictitious experiment where the experimental setup and the sand and fluid properties almost remain identical, except decreasing the Young's modulus value of sand from $E = 1.3 \times 10^6\ Pa$ to an appropriate value $E = 1 \times 10^4\ Pa$. It gives valuable deformation to the porous sample and then enables us to analyze the potential impact of dynamic capillarity pressure on fast drainage. We note that we only did preliminary qualitative analysis here. The evolutions of average porosity and average permeability of the given system are presented in Fig. 2.11 and Fig. 2.12 respectively.

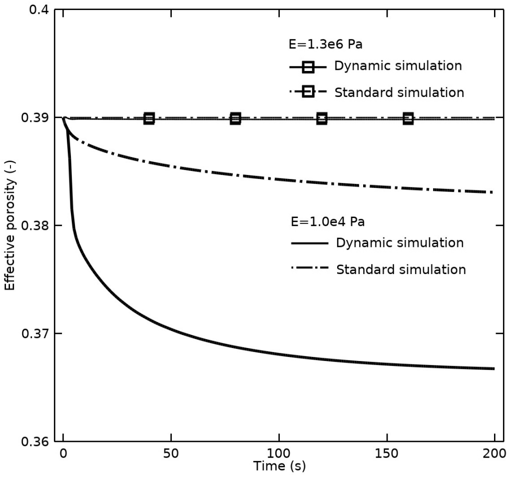

Figure 2.11: Comparison of average effective porosity with $E = 1.3 \times 10^6\ Pa$ and $E = 1 \times 10^4\ Pa$

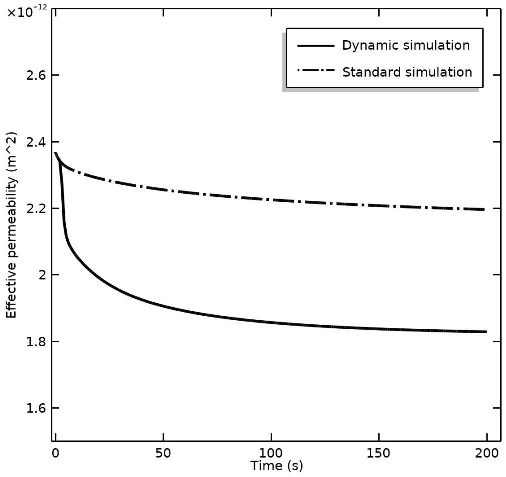

Figure 2.12: Evolution of average permeability with $E = 1 \times 10^4\ Pa$

As time goes by, the development of volumetric shrinkage caused by capillary pressure develops gradually leads the effective porosity as well as effective permeability to decrease. Obviously, results obtained from dynamic modelling deviate from the corresponding results of standard modelling remarkably. The curves of average water volume (ϕS_w) of dynamic and standard modelling are presented and compared in Fig. 2.13. The observed discrepancy between these two curves intuitively indicates that the unexpected deformation due to dynamic effects has impact on drainage.

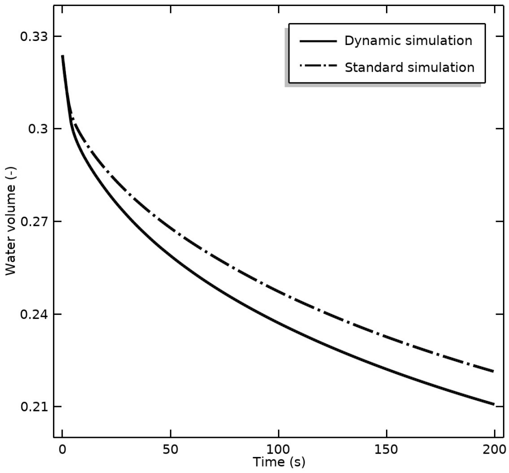

Figure 2.13: Evolution of average water volume with $E = 1 \times 10^4\ Pa$

2.5 Further application and discussion of the proposed model on drainage of deformable porous medium

2.5.1 Fictitious drainage experiment of porous medium

In the second test, the drainage of a homogeneous porous column with radius $r = 0.5m$ and height $h = 0.3\ m$ is simulated. The results from dynamic simulation are compared with the corresponding standard simulation. Various analyses on capillary pressure, effective saturation and deformation have been performed.

During the numerical drainage test, air pressure keeps constant and equals to atmospheric pressure. No flow is allowed at the bottom and on the top surface. The drainage only

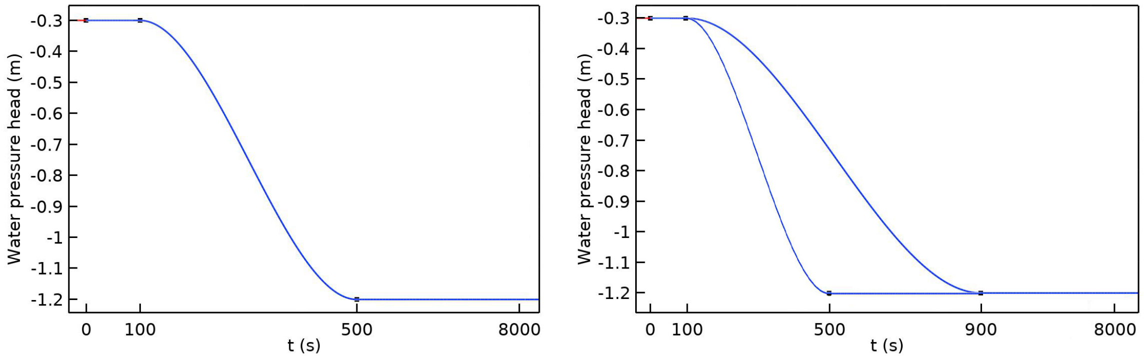

(a) Evolution of boundary pressure head

(b) Comparison of relative fast and slow boundary pressure heads

Figure 2.14: Evolution of different boundary pressure heads

occurs on the lateral surface. The initial saturation is 0.92. The drainage process begins by decreasing the surrounding water pressure head from $-0.3m$ to $-1.2m$. The detailed evolutions of boundary water pressure are plotted in Fig. 2.14(a). The negative tension capillary pressure is the only force to cause deformation. No load is imposed on the lateral surface. On the top and at the bottom of the column no vertical deformation is allowed. Neglecting the gravitational load, this 3D numerical example is simplified to a 2D plane strain problem. Table 2.3 gives the parameters used for the numerical test.

Similar to the test of last section, standard and dynamic coupling model are used to simulate the drainage respectively. For the dynamic model, a constant τ is chosen based on Eq. (2.20), neglecting any functional dependency on the water saturation, because we just strictly focus on the qualitative behavior of dynamic effects.

2.5.2 Results analysis for dynamic and standard modellings

The distribution of the effective saturation and the radial displacement obtained with dynamic model at $T = 400\ s$ is plotted in Fig. 2.15(a) and Fig. 2.15(b), respectively. Fig. 2.16(a) and Fig. 2.16(b) show the variation of effective saturation versus the radius at different time. It is obvious that the position closer to the boundary, the faster the saturation drops and the saturation obtained with dynamic model is always lower than the corresponding saturation obtained with standard model. This phenomenon is significant

Table 2.3: Material data for the numerical test

Patameters	Unit	Description	Value
ρ_w	kg/m^3	Water density	1000
g	m/s^2	Gravitational acceleration	9.82
K	m/s	Intrinsic hydraulic conductivity	7×10^{-6}
n	1	van Genuchten's coefficient	1.37
φ	$1/m$	van Genuchten's coefficient	1.6
l	1	Pore connectivity parameter	0.5
θ_s	1	Saturated liquid volume fraction	0.46
θ_r	1	Residual liquid volume fraction	0.034
H_w	m	Initial water pressure head	-0.3
E	Pa	Young's modulus	1×10^6
v	1	Poisson's rate	0.25
ρ_s	kg/m^3	Soil density	2000

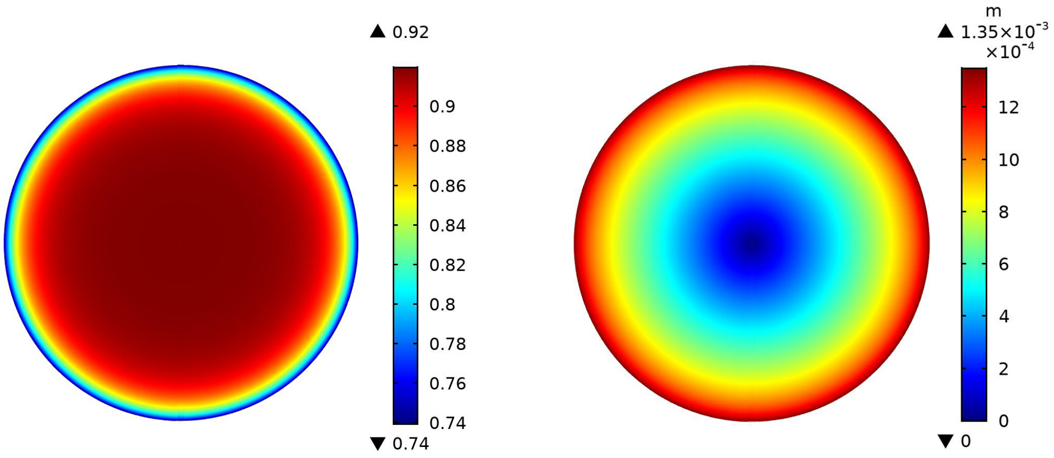

(a) Effective saturation at $T = 400\ s$ (b) Radial displacement at $T = 400\ s$

Figure 2.15: Distribution of effective saturation and Radial displacement at $T = 400\ s$

especially at the earlier stage when the boundary condition experiences rapid change. This indicates that dynamic effects accelerate the drainage process.

Capillary pressure distribution versus radius at different time points are plotted in Fig.

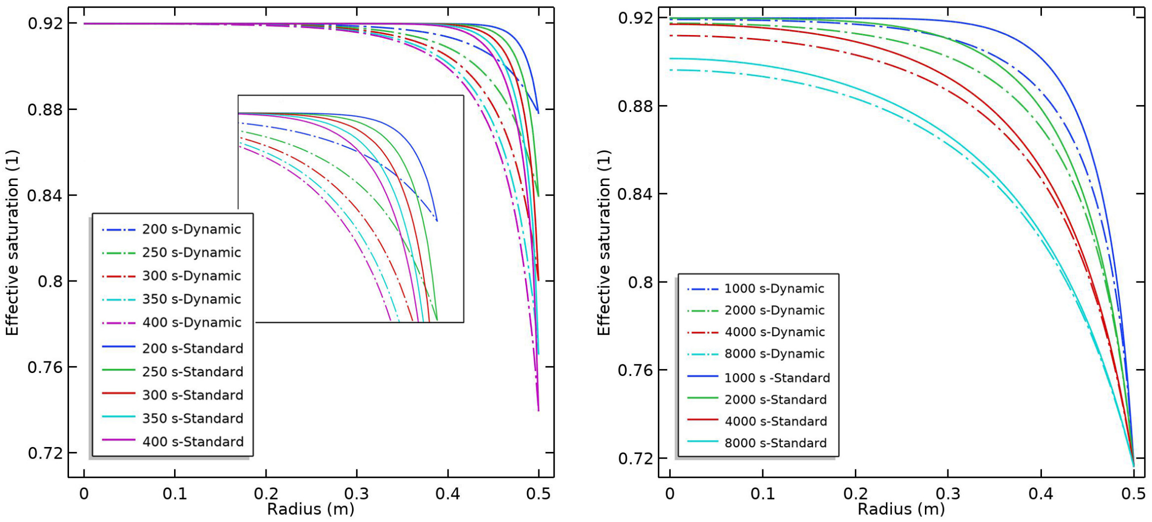

(a) Effective saturation versus radius at earlier stage

(b) Effective saturation versus radius at later stage

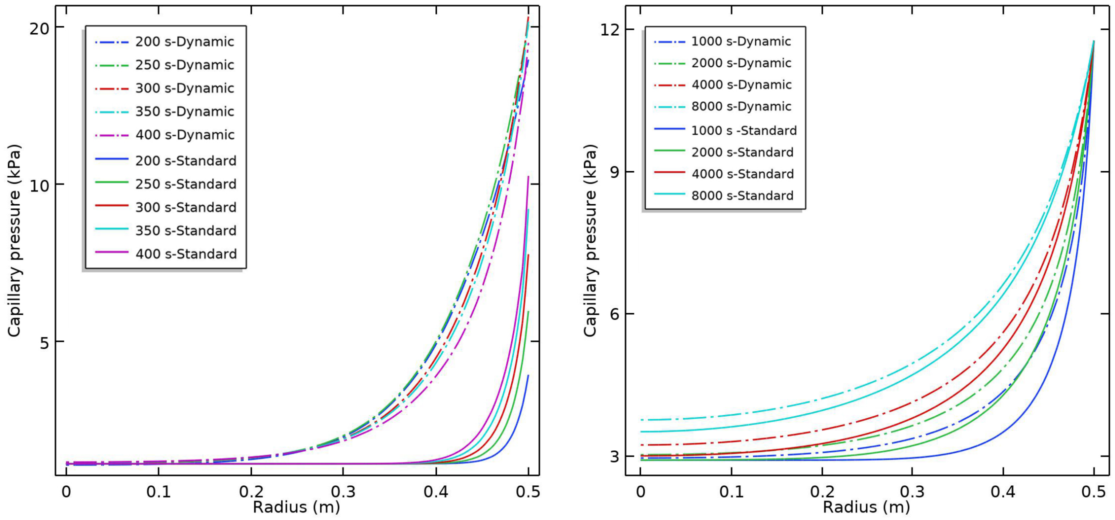

(c) Capillary pressure versus radius at earlier stage

(d) Capillary pressure versus radius at later stage

Figure 2.16: Distribution of effective saturation and capillary pressure at different stages

2.16(c) and Fig. 2.16(d). It is obvious that the capillary pressure increases rapidly in areas close to the surface. The position closer to the boundary, the greater the capillary pressure is. Another important observation is that the dynamic capillary pressure is more pronounced than standard capillary pressure at the area close to surface during the earlier stage when the boundary conditions suffer fast change. When the boundary conditions enter a stable period, dynamic effects still exist. However, those two kinds of capillary pressures tend to be close. It means that dynamic effects continue to decrease as time goes by. The last term of Eq. 2.25 represents the contribution of dynamic capillarity effect. Judging from this additional term caused by dynamic effects, the strength of dynamic effects depends on time change rate of saturation $\partial S_w/\partial t$, effective permeability, relative permeability and dynamic effects coefficient directly. However, the $\partial S_w/\partial t$ plays a predominate role in deviating capillary pressure obtained with dynamic model from that obtained with standard model, because of a good agreement between evolution of dynamic effects and evolution of $\partial S_w/\partial t$ can be observed. As plotted in Fig. 2.16(b) and Fig. 2.16(d), the dynamic effects decrease gradually as time passes. Moreover, an implication is observed that the point with maximum deviation between dynamic and standard capillary pressure seems to propagate from the surface to centre and this maximum deviation decreases gradually. Considering that capillary pressure is the driving force to transport water, capillary pressure with the consideration of dynamic effects may cause faster drainage compared with prediction from static modelling, which is evidenced with the result curves in Fig. 2.16(a).

The radial displacements obtained from dynamic numerical model are compared with those governed by standard numerical model in Fig. 2.17(a) and Fig. 2.17(b). In general, dynamic effects enhance the displacement. The radial displacement increases from inner to surface and the slope of these curves are increasing as radius increases. When it is close to the surface, the slope of the curve reaches to maximum. Radial displacement derived from dynamic coupling model is always greater than that derived from standard coupling model at identical time points. It demonstrates that dynamic effects have a significant impact on displacement at earlier stage. This earlier dynamic displacement is even greater than the maximum static displacement at end time of $8000\ s$. When the boundary conditions become constant, the dynamic capillarity effect is limited.

Meanwhile, volume ratio distribution plotted in Fig. 2.17(c) and Fig. 2.17(d) demonstrates the volume shrinkage directly. In general, the position closer to the surface of porous media, the more obvious the solid shrinkage is. The volume shrinkage obtained from dynamic coupling simulation is greater than that obtained from standard coupling simulation, especially at the area near surface during earlier stage. As presented in the Eq. (2.31), the evolution of shrinkage is governed by effective pore pressure which is a functional dependency on capillary pressure and saturation. Effective pore pressure obtained with dynamic model is greater than that obtained with standard model. So that, the nature of the observed phenomenon demonstrated in Fig. 2.17(c) is that the effective pore pressure induced by dynamic capillary pressure increases the stress imposed on solid, and this

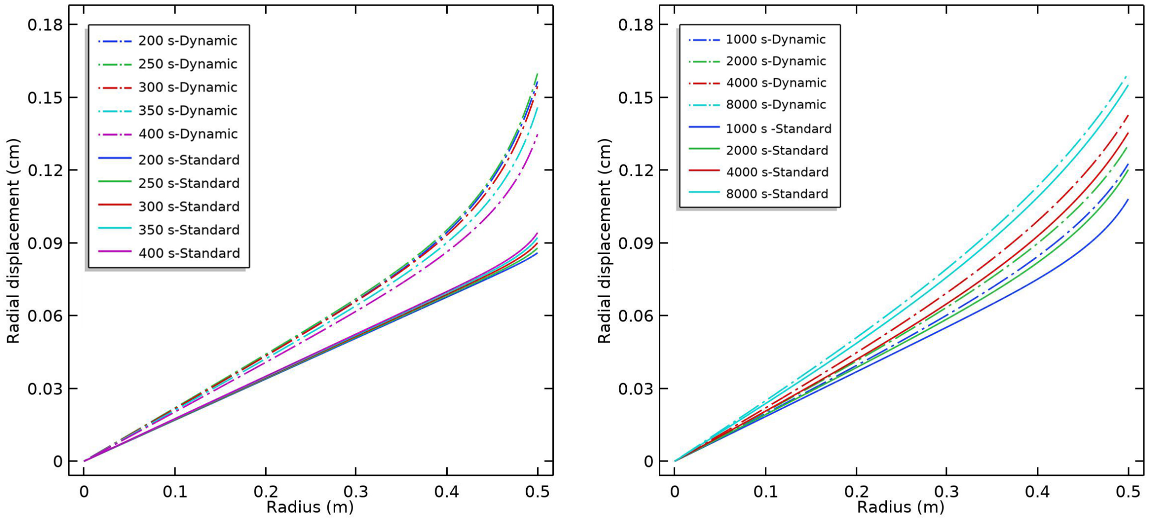

(a) Radial displacement versus radius at earlier stage (b) Radial displacement versus radius at later stage

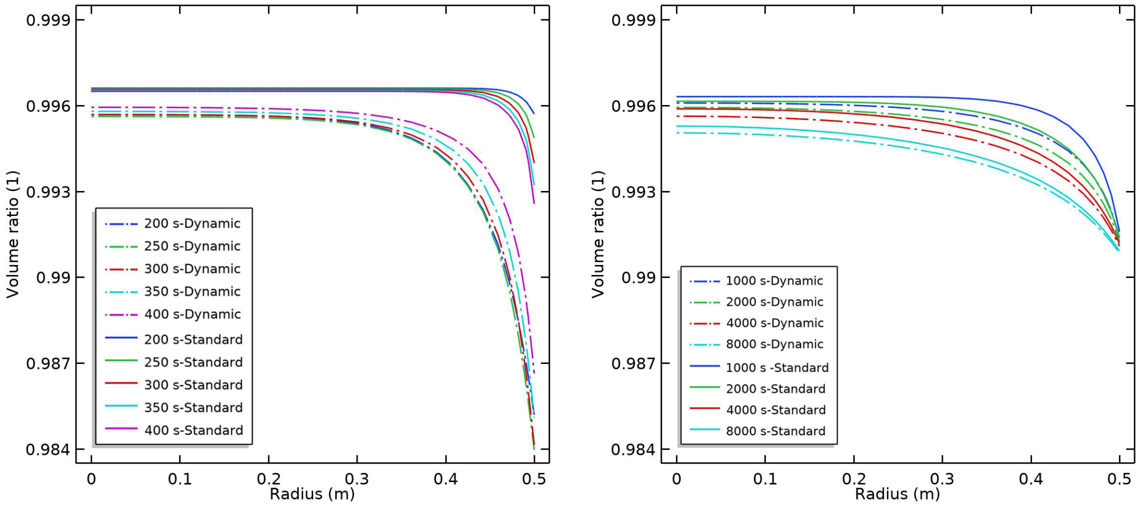

(c) Volume ratio versus radius at earlier stage (d) Volume ratio versus radius at later stage

Figure 2.17: Distribution of deformation at different stages

increased stress amplifies the shrinkage and raises the likelihood in causing cracks in porous media. At later stage, however, the dynamic effects continue to weaken as boundary conditions become stable. the differences between dynamic shrinkage and static shrinkage decrease gradually. Moreover, by comparing Fig. 2.17(c) and Fig. 2.17(d), it is obvious that, in the area close to the surface of porous materials, the shrinkage obtained with dynamic model at earlier stage is even greater than the maximum shrinkage at later stage. It seems that the time change rate of boundary condition is an important factor of the risk prediction.

In order to quantitatively analyzes the effect of time change rate of boundary water pressure head on solid skeleton deformation, the identical simulation is performed once again only by replacing the initial fast change boundary condition with a slow change rate one the comparison of these two boundary conditions are plotted and compared in Fig. 2.14(b). As for high change rate condition, the boundary pressure head decreases from -0.3 m to -0.12 m in 400 s, while it needs 800s for the low change rate condition.

2.5.3 Exploration of the relationship between dynamic effects and change rate of boundary condition

The percentage of additional radial displacement and volume shrinkage caused by dynamic effects at different positions during earlier stage are depicted in Fig. 2.18(a) and Fig. 2.18(b), respectively. The additional displacement, obtained with boundary condition changing with high speed, is significantly larger than that obtained with low change rate. Moreover, the closer to the material surface, the additional displacement of solid is greater and its growth rate also increases. The additional displacement can reach to 40%. Similar phenomena and laws are observed in additional volume shrinkage. The percentage of additional volume shrinkage can even reach to 70%. The additional deformations caused by dynamic effects could not be neglected. The phenomenon observed in numerical simulation has a good agreement with the proposed dynamic model that indicates that volumetric shrinkage is a dependency on time change rate of saturation. The importance of the dynamic effects in predicting the risk of porous media is evidenced, especially when the material is exposed to a rapidly changing environment. And the cracks are more likely to occur at the area close to

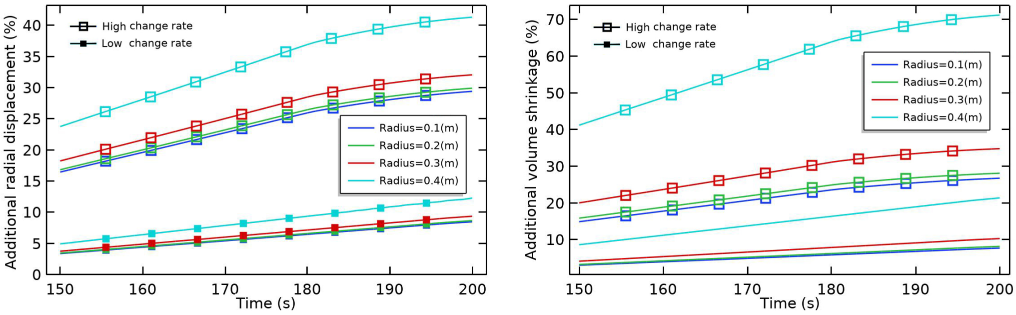

(a) Percentage of additional radial displacement (b) Percentage of additional volume shrinkage

Figure 2.18: Percentage of additional deformation

surface.

2.6 Concluding remarks

In this chapter, a coupled dynamic model, which implements the dynamic capillarity effect and fluid-solid coupling into unsaturated water-air flow, has been proposed. Taking into account the fast drainage of surface pores by a dynamic fluid movement to simulate the shrinkage of porous media is innovative. After that, we carry out a test to allow the validation of the proposed dynamic model with regard to documented experiment results. The numerical results of mechanical behaviour in the case of coupled dynamic modelling and standard modelling (no dynamic capillarity effect) have also been performed. Based on the experimental verifications and comparisons for simulation results obtained from different modelling, the following conclusions can be drawn:

1) Compared with the traditional standard model, the dynamic model is advanced because the dynamic capillarity effect is considered not only for Darciean advection, but also mechanical deformation. The estimation on dynamic coefficient for porous media is performed based on inverse calibration method. The τ obtained by inverse analysis enables the modelling results to coincidence with experimental data. Meanwhile, this τ is in accordance with the measured value.

2) Comparisons with measured average saturation and water pressure for sand sample drainage experiments show that modelling taking dynamic effects into account could provide numerical results with high agreement. The main reason is that dynamic model could predict the capillary pressure closer to actual value for unsaturated water transport, especially in the condition that the saturation experiences rapid variation.

3) According to the comparisons performed in this chapter, it proves that dynamic capillarity effect generates unexpected displacement (shrinkage) which increases the possibility of cracking risk. Thus, dynamic capillarity effect should be emphasized in predicting durability of porous media. Meanwhile, this unexpected deformation should not be ignored in predicting the water drainage especially when the negative force capillary pressure causes valuable shrinkage.

For the prospective, improving the dynamic coupled model considering vapor diffusion is necessary. In general, the moisture transport for weakly permeable porous media consists of water flow and vapor diffusion. The vapor transport plays a predominant role for the drainage process when the residual saturation is reached. Therefore, it is meaningful to ameliorate the coupled model by considering phase transformation.

Chapter 3

Contribution of the dynamic capillary pressure on fast drying of mature cement-based materials

3.1 Background

It is expected that the climate variation results in wetting-drying cycles in concrete structures. Most of the mechanisms of deterioration, such as chloride ingress and corrosion, are governed by moisture transport in porous material [14, 15, 134]. Moreover, These cycles are the main cause of great swelling and shrinkage phenomena. For example, the low ambient relative humidity induces high order of magnitude of the capillary pressure which causes drying shrinkage [16]. Indeed, the tensile stress existing in cementitious materials is due to the development of drying shrinkage [135]. If this stress exceeds the tensile strength, micro-cracks begin to generate and then develop to macro-cracks [136]. The cracks formed in the cement matrix decrease the durability of concrete [115]. Essentially, the moisture state determines the distribution of capillary pressure which is the driving force for shrinkage and swelling of concrete. Therefore, in order to evaluate the durability of cement-based infrastructures, the evolution of moisture state and drying shrinkage must be mastered.

Predictive models have been developed to calculate the influence of wetting-drying cycles on deformation of concrete. Ghourchian et al. [137] developed a poromechanics approach to plastic shrinkage. As reported in [138], a multiscale approach to model the rate of self-desiccation shrinkage of cementitious materials was proposed. A predictive method of early autogenous shrinkage based on the capillary tension theory and microstructure pore was established by Li et al. [139]. Most of them are based on simple quasi-static fluid flow. Occasionally, the deformation variation is taken into account to modify the porosity and the permeability coefficient during the drying evolution. However, these models can only simulate drying for high external relative humidities for which the drying kinetics is slow and can be simulated by a quasi-static model. In case of low external relative humidity, some authors calibrate the exchange coefficient between the material and the environment according to the moisture kinetics [140]. Others consider higher permeability coefficients in order to increase the mass loss as measured in experiment [141]. The authors have explained this observation by assuming that more cracks appear during shrinkage. Previously, Day et al. [142] have suggested this assumption, but also indicated that it could be due to capillary tension forces. In our opinion, in a first approximation it is more relevant to develop a descriptive model to understand the role of each phenomenon in the global behaviour. So, how to consider physics effects in modelling to analyze the fast drying under low external relative humidity conditions?

The pressure difference between gas mixture and liquid water could deviate from the original static capillary pressure under dynamic situation in which viscous forces are non-negligible and need unexpected pressure gradient to overcome [118]. It can be explained by a theory of dynamic effects on capillary pressure [22]. The capillary pressure-saturation ($P_c - S_w$) relationship is crucial to predict moisture transport in cement-based materials.

In recent decades, Considerable attention has been paid to unsaturated flow in quite permeable materials with dynamic effects considered [22, 25, 121, 143]. However, these well-developed dynamic capillarity effect theories have not been applied to weakly permeable materials (cement-based materials). Compared with quite permeable materials, the moisture transport in weakly permeable materials is more complex.

The moisture transport in low permeable materials, such as cement paste and concrete, consists of liquid-water advection in the pore network and water-vapour diffusion in space without liquid. Indeed, the contribution of vapour diffusion on the entire moisture transport is significant, especially in low relative humidity condition. As mentioned in the chapter of literature review, Coussy [58] has proposed a complete multi-phase model to simulate the moisture transport based on the continuum approach. In this model all mechanisms, including advection of liquid-water, evaporation of liquid-water, diffusion of vapour and variation of gas mixtures, are coupled. For simplification, most of the standard drying models [6, 56, 57, 60, 144, 145] are developed on the basis of the assumptions that air pressure is constant and advection of vapour is negligible. The simplified model can also provide high accuracy for drying process. In addition, various empirical models are also used to predict the evolution of moisture state [54, 55, 146–149]. However, the transport coefficient, which is the most significant factor of the model, is not absolutely associated with the transport property and the diffusion mechanism. It is a non-negligible drawback and may reduce the accuracy.

This chapter aims to present an advanced model with consideration of dynamic capillarity effect and skeleton deformation for fast drying of cement-based materials. In this chapter this model will be called ’coupled dynamic model’ while when the deformation skeleton is not taken into account it will be called ’uncoupled dynamic model’; and ’standard model’ will be used when the dynamic capillarity effect is not taken into account. First, the derivation of this coupled dynamic model is introduced in detail. Then drying experiments of a kind of cement paste have been employed for the verification of this advanced model. Modelling results based on dynamic effects and non-dynamic effects are compared with experimental one. The last part investigates the skeleton deformation performed with dynamic effects and no-dynamic effects modelling.

3.2 Dynamic governing model for moisture transport in deforming porous media

3.2.1 Moisture transport from standard to dynamic model

Plenty of research results have proved that unsaturated moisture transport in weakly permeable porous media like cementitious material is composed of advective transport of liquid water and the advection-diffusion of gas mixture consisting of water vapour and dry air [28, 58]. The typical mass conservation equation for moisture transfer in porous material is written as follows:

$$\frac{\partial\left(\phi S_w \rho_w\right)}{\partial t}+\frac{\partial\left[\phi(1-S_w)\rho_v\right]}{\partial t}+\frac{\partial\left[\phi(1-S_w)\rho_a\right]}{\partial t}+\nabla\cdot\left(\rho_w V_w+\rho_v V_v+\rho_a V_a\right)=0 \tag{3.1}$$

where subscripts w, v, a represent respectively liquid water, vapour and dry air, ρ_α and V_α the density and the velocity of $\alpha = w, v, a$, ϕ the effective porosity, S_w the saturation of liquid water. For a deformable porous medium, the effective porosity can be expressed as follows:

$$\phi=\frac{\phi_0+\varepsilon_v}{1+\varepsilon_v} \tag{3.2}$$

where ϕ_0 represents the initial intrinsic porosity and ε_v the volumetric strain.

Considering the gaseous phases have much lower densities compared with liquid water, the second and third terms at the left-hand side of the equation (3.1) is considered negligible. An earlier study has justified that dry air transport has very weak contribution to total mass transport and only causes fluctuated air pressure in the material [150]. Similar conclusion was also obtained by the asymptotic analysis implemented by Coussy [58]. Besides, because of the liquid water is assumed incompressible, the initial mass conservation (equation 3.1) can be simplified by the following equation regarding liquid water and water vapour [28, 151]:

$$\rho_w\frac{\partial\left(\phi S_w\right)}{\partial t}+\nabla\cdot\left(\rho_w V_w+\rho_v V_v\right)=0. \tag{3.3}$$

The advective velocity of water V_w is defined by Extend Darcy's law:

$$V_w=-\frac{k k_{rw}}{\eta_w}\nabla P_w \tag{3.4}$$

where k, k_{rw}, η_w, P_w represent effective permeability, relative permeability, water viscosity, water pressure respectively. Taking into account the deformation of the solid skeleton, the effective permeability is not constant. A well-known function converts initial intrinsic permeability k_0 into effective permeability based on effective porosity [127, 152]:

$$k=k_0\left(\frac{\phi}{\phi_0}\right)^3\left(\frac{1-\phi_0}{1-\phi}\right)^2. \tag{3.5}$$

The vapour transport includes two terms corresponding to Darcian advection and Fickian diffusion. It is reasonable to assume that the total pressure of gas mixture is almost constant and equals to the atmospheric pressure, so that the Darcian advection is negligible [28]. Thus, the velocity of vapour transport V_v only corresponds to Fickian diffusion which is written as follows:

$$V_v = -\frac{D\nabla\rho_v}{\rho_v} = -\frac{D_0 f \nabla\rho_v}{\rho_v} \tag{3.6}$$

where D, D_0, f represent the vapour diffusion coefficient, the free vapour diffusion coefficient in air, the resistance factor of pore network for gaseous diffusion respectively. f is a function of porosity ϕ and effective saturation S_w, which is given by:

$$f(S_w, \phi) = \phi(1 - S_w)\phi^{x_D - 1}(1 - S_w)^{x_D + 1} \tag{3.7}$$

where x_D is a material parameter. For granular media like soils, Millingon [153] suggested $x_D = 4/3$. In terms of cement and mortar, $x_D = 2.74$ is recommended [154]. $\phi(1 - S_w)$ implies the actual space variable for vapour diffusion. $\phi^{x_D - 1}(1 - S_w)^{x_D + 1}$ represents the tortuosity and connectivity effects.

The vapour is assumed as ideal gas in this research; thus the following relationship is obtained:

$$\rho_v = \frac{P_v M_v}{RT} \tag{3.8}$$

where P_v, M_v, R, T represent the vapour pressure, the vapour molar mass, the gas constant and the absolute temperature respectively.

The thermodynamic equilibrium between the liquid water and vapour is presumed. Thus, the Kelvin's equation shows the dependence of capillary pressure on relative humidity:

$$P_c = -\frac{\rho_w RT}{M_w} \ln\frac{P_v}{P_{vs}} \tag{3.9}$$

where P_{vs}, M_w represent the saturated vapour pressure and the water molar mass respectively.

Capillary pressure P_c is a discontinuity in pressure across the interface which is roughly equals to the difference between the gas mixture pressure P_g and the liquid water pressure P_w. Once the capillary pressure P_c is known, the saturation of liquid water S_w is immediately obtained by means of experimentally determined functions. The relationship of P_c is defined as a functional dependency on S_w, called the retention curve. For cement-based materials with low permeability, this curve is indirectly measured by sorption experiments implemented at constant temperature. Various models, including Brooks-Corey model and van Genuchten model, were proposed to describe the retention curve. In this chapter, the well-accepted model proposed by van Genuchten is employed:

$$P_c(S_w) = \alpha\Big({S_w}^{-1/m} - 1\Big)^{1-m} \tag{3.10}$$

where α, m represent dimensionless parameters related to the pore-size distribution.

Relative permeability is an important variable which is also a functional dependency on S_w. Following the previous literatures [128, 141], a well-known and simple analytical relation derived from Genuchten-Mualem equation is chosen:

$$k_{rw} = {S_w}^{l}\Big[1 - \Big(1 - {S_w}^{1/m}\Big)^{m}\Big]^{2}. \tag{3.11}$$

where l is a paramter which represents effects caused by tortuosity. The value $l = 0.5$ was proposed as the best choice for cement-based materials [155, 156].

Van Genuchten retention model also defines the moisture capacity $\partial S_w/\partial P_c$:

$$\frac{\partial S_w}{\partial P_c} = \frac{m}{\alpha(m-1)}{S_w}^{1/m}\Big(1 - {S_w}^{1/m}\Big)^{m}. \tag{3.12}$$

Substituting equations (3.4), (3.6) and (3.8-3.12) into mass balance equation (3.3) yields a standard governing equation for moisture transport in deformable porous medium written in terms of water pressure as follows:

$$\begin{aligned} -\phi\frac{\partial S_w}{\partial P_c}\cdot\frac{\partial P_w}{\partial t} - \nabla\cdot\Big(\frac{kk_{rw}}{\eta_w}\nabla P_w\Big) - \frac{M_v P_{vs}}{RT\rho_w}\nabla\cdot\Big[D_0 f\nabla e^{\left(\frac{M_w P_w}{\rho_w RT}\right)}\Big] \\ +S_w\frac{\partial\phi}{\partial t} = 0. \end{aligned} \tag{3.13}$$

In the above equation, the second term represents the contribution of water advection and the third term indicates the contribution caused by vapour diffusion. The last term takes into account the impact of porosity variation for moisture transport. Combining a certain initial condition and boundary conditions, the solution of moisture transport problem is accessible.

The moisture evaporation on the surface of porous media is mainly influenced by the interaction between porous media and the surrounding environment. The external moisture gradient, observed in the air in the vicinity of the open surface of porous media, governs the moisture transport from the interior of the porous media to its surface where evaporation happens. The Neumann-type boundary condition, which takes this given gradient into account, has been utilized in plenty of previous researches [141, 151, 157]. The formula is presented as follows:

$$w = \phi S_w^0 E_v \left(P_v^o - P_v^e\right), \tag{3.14}$$

where w represents the mass flux of moisture, P_v^0 the vapour pressure, P_v^e the surrounding vapour pressure and S_w^0 the water saturation within the media near the surface. The moisture exchange between the ambient environment and the porous media is mainly governed by emissivity E_v. A value $E_v = 2.58 \times 10^{-8} kg \cdot m^{-2} \cdot s^{-1} \cdot Pa^{-1}$ is measured for laboratory condition that there is no air flow and $T = 296 \pm 1K$ [158]. The term ϕS_w^0 represents the influence due to the decrease of wet surface when exposed to the environment with low RH.

It is necessary to notice that equation (3.10) is applied to main water vapour sorption isotherms. In this chapter, we strictly focus on dynamic effects without discussing hysteresis. The dynamic effects are not exactly identical with hysteresis which is caused by ink-bottle effect, the variation of liquid-solid contact angle and the pore-size distribution and pore connectivity [38, 119]. Moreover, dynamic effects are dependent on change time rate of saturation and permeability [22, 93, 120]. Plenty of experiments proved that there exist dynamic effects when the saturation in porous medium surfers rapid fluctuation [10, 19, 93, 101, 116, 117]. In fact, in the case of modelling with the rapid change of surrounding relative humidity, a dynamic model is indispensable to calculate a new $P_c - S_w$ relationship. The well-accepted equation (3.15), derived from thermodynamic theories and constitutive conservation laws, was mentioned firstly in [21]:

$$P_c^{dyn} - P_c = -\tau \frac{\partial S_w}{\partial t}. \tag{3.15}$$

The pressure difference between gas mixture and liquid water, indicated as P_c^{dyn}, is a measured quantity during experiments. Meanwhile, the symbol P_c stands for equilibrium (or 'static') capillary pressure. The parameter τ is the dynamic effects coefficient, which serves as an assessment of the magnitude of dynamic capillarity effect. Since the gas mixture pressure could be assumed constant, the equation (3.15) reduces to the equation (3.16). The water pressure in the case of modelling with dynamic effects P_w^{dyn} should be used to replace the static water pressure P_w in moisture transport governing model:

$$P_w^{dyn} = P_w + \tau \frac{\partial S_w}{\partial t}. \tag{3.16}$$

Moreover, taking into account dynamic effects, Kelvin's equation (3.9) evolves into:

$$P_c^{dyn} = -\frac{\rho_w RT}{M_w} \ln \frac{P_v^{dyn}}{P_{vs}}, \tag{3.17}$$

where P_v^{dyn} represents the dynamic vapour pressure. Practically, equations (3.16) and (3.17) govern the dynamic capillarity effect on water advection and vapour diffusion respectively. By submitting these relations to standard governing equation to replace the initially corresponding relations, it leads to the dynamic coupled model for vapour-water moisture transport:

$$\begin{aligned} -\phi\frac{\partial S_w}{\partial P_c} \cdot \frac{\partial P_w}{\partial t} - \nabla \cdot \left[\frac{kk_{rw}}{\eta_w}\nabla\left(P_w + \tau\frac{\partial S_w}{\partial t}\right)\right] + S_w\frac{\partial \phi}{\partial t} \\ -\frac{M_v P_{vs}}{RT\rho_w}\nabla \cdot \left\{D_0 f \nabla e^{\left[\frac{M_w}{\rho_w RT}\left(P_w + \tau\frac{\partial S_w}{\partial t}\right)\right]}\right\} = 0. \end{aligned} \tag{3.18}$$

The terms $\tau\frac{\partial S_w}{\partial t}$ in equation (3.18) represent the additional contribution on moisture transport induced by dynamic capillarity effect. The first one among them indicates the additional contribution caused by dynamic water advection. The second one stands for the additional contribution of dynamic vapour diffusion. Similar with the standard coupled model for moisture transport (equation 3.13), with certain given initial and boundary conditions, the dynamic moisture transport problem can be figured out.

3.2.2 Dynamic poro-mechanical model

Coussy et al. [85] proposed an upgraded poro-mechanical model for cementitious materials by introducing the concept of equivalent pore pressure to substitute the effective pore pressure. This takes into account the additional contribution due to the release of interface energy during drying. Vlahinić [86] improved the initial model by providing the effective bulk modulus of the solid $\overline{K_s}$ to replace the initial constant K_s. It means that the bulk modulus of solid changes with drying is considered. In this work, we focus on dynamic capillarity effect, and strictly deal with the contribution of dynamic capillary pressure on skeleton deformation. For simplicity, the matrix is assumed to be rigid, leading to $K_s \to \infty$. And the contribution of the interface energy is also neglected. So that, the same coupled dynamic model for predicting shrinkage of sand and soil developed in the last chapter is also applicable for cememtitious materials. Therefore, when the dynamic effects are taken into account, the shrinkage model for isotropic and partially saturated cementitious materials is:

$$\varepsilon_v = S_w \left(P_c - \tau \frac{\partial S_w}{\partial t} \right) \left(\frac{1}{K_b} \right) \tag{3.19}$$

The combination of equations (3.18), (3.19) and (2.32) leads to the coupled model which could takes into account dynamic capillarity effect and governs the studied phenomenon.

3.3 Presentation of the numerical test

3.3.1 Modelling method

In order to obtain quantitative solutions for the proposed model, an appropriate numerical algorithm has been chosen. The governing equations are discretized in space by finite element method and in time by an implicit time-stepping method which is backward Euler method. The Galerkin method is used to get access to a weak form of the governing equations.

The basic variables of the studied phenomenon are displacement u and water pressure P_w. They are expressed by global shape function matrices $\mathbf{N}^u$ and $\mathbf{N}^p$ as function of nodal value vectors $\mathbf{u}$ and $\mathbf{p_w}$: $\mathbf{U} = \mathbf{U}(t) = \mathbf{N}^u \mathbf{u}(t)$ and $P_w = P_w(t) = \mathbf{N}^p \mathbf{p_w}(t)$. According to the Galerkin method and Green's theorem, the following set of algebraic equations in space is obtained as follows by substituting these defined basic variables into governing equations:

$$\mathbf{K u} - \mathbf{C_{dyn}} \dot{\mathbf{p}}_\mathbf{w} + \mathbf{C_{sw} p_w} = \mathbf{f_u}, \tag{3.20}$$

$$\mathbf{C_{ws}} \dot{\mathbf{u}} + \mathbf{P_{ww}} \dot{\mathbf{p}}_\mathbf{w} + \mathbf{H_{ww} p_w} = \mathbf{f_w}. \tag{3.21}$$

The detailed derivation of the governing equations in discretised form is collected in Appendix. The meaning and full expression of the listed matrices can also be found in Appendix.

A two-dimensional plain strain hypothesis has been employed. The simulation is carried out using uniform mesh of 1750 rectangle elements for analysis. As presented in Fig. (3.1),

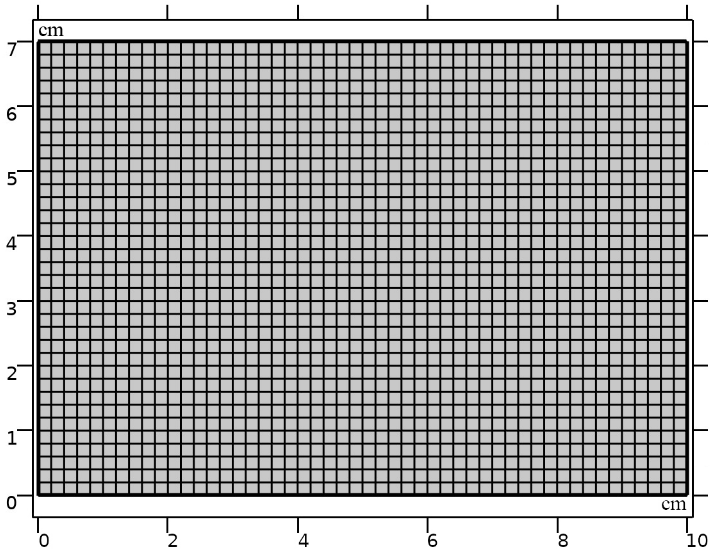

Figure 3.1: Schematic representation of mesh

50 elements on the length and 35 elements on the width. This mesh is sufficiently high to optimize the computing time and sufficiently small to well follow the fields. An implicit approximation (backward Euler method) in time step is employed to guarantee the stability of the scheme. Furthermore, to solve the governing equations efficiently, the time step is flexible according to the convergence rate.

As introduced previously, no existing literature considers a problem of moisture transport in a deforming porous media with dynamic effects accounted and very few documented experiment has been performed. One of these is a drying experiment for cement paste sample conducted by [37, 159], for which simulations performed with uncoupled standard model have been obtained by various researchers [141, 151]. This drying experiment has been used for the validation of the proposed coupled dynamic model.

To emphasize the influence of dynamic capillarity effect on moisture transport and skeleton deformation, three models including coupled standard model, uncoupled dynamic model and coupled dynamic model are employed to simulate the same drying experiment. Coupled standard model is used to simulate the moisture transport without considering the dynamic capillarity effect. By removing the terms relevant to dynamic effects in the coupled dynamic model, this model is easily achieved. As for an uncoupled dynamic model, it takes into account the dynamic capillarity effect, while totally neglects the performance of deformation. Thus, this model can also be obtained by eliminating the corresponding terms relevant to deformation in coupled dynamic model.

3.3.2 Experimental data

Experimental tests used for the comparison were performed by [37, 159]. Cement paste specimens were designed with Ordinary Portland Cement. Their properties are collected and summarised in Table 3.1. The cement pastes were cast in cylindrical mould with a diameter $d = 7cm$. Prior to drying experiment, the cement paste specimen has been cured for more than two hundred days in a sealed condition to reach physical (mechanism) and chemical stabilization. After removing the mould, the column was cut into $h = 10cm$ specimens. One end and the lateral surface of the sample were sealed with self-adhesive aluminium foil sheets. Only the other end was open for moisture evaporation. As evaporation goes on, the induced pressure gradient in porous media transfers the inner moisture to open surface continuously (Figure 3.2). The drying experiments were performed at a stable temperature T=296 ± $0.1K$. The specimens were submitted to drying at two fixed external relative humidity 53.5% and 63.2% respectively. RH was fixed at $RH^e = 53.5\%$ by using a

Table 3.1: Properties of cement paste I

Porosity	Initial RH	w/c	Young's modulus	Poisson's ratio	V-G Parameters	
					$\alpha(MPa)$	m
0.31	83%	0.35	29 (GPa)	0.26	44.75	0.48

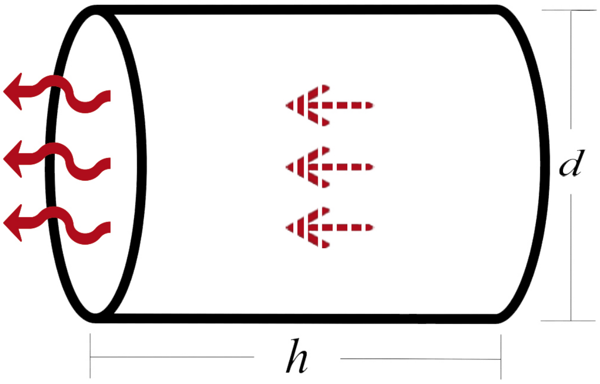

Figure 3.2: Schematic representation of drying

saturated salt solution (magnesium nitrate, $M_g(NO_3)_2 \cdot 6H_2O$). On the other hand, RH was fixed at $RH^e = 63.2\%$ by using solution of ammonium nitrate NH_4NO_3. Both of their mass loss curves were measured by weighing the specimens at intervals. No external load exists and the gravity is also neglected. Only axial deformation on the open end is allowed.

The main desorption isotherm curve is measured by the saturated salt solution method. The detailed description of the measurement is reported in [37]. The data related to main desorption isotherm were collected from literature [37, 159], and fitted according to the van Genuchten model to determine parameters a and m. The fitting curve is presented in Figure 3.3 and the corresponding parameter values are presented in Table 3.1. The values of mechanical properties are collected from previous literature [160] in which the mechanical properties of almost identical cement paste are measured. However, the important parameter permeability (or hydraulic conductivity) is unknown. In this chapter, the inverse analysis method is adopted to fix the absent parameter.

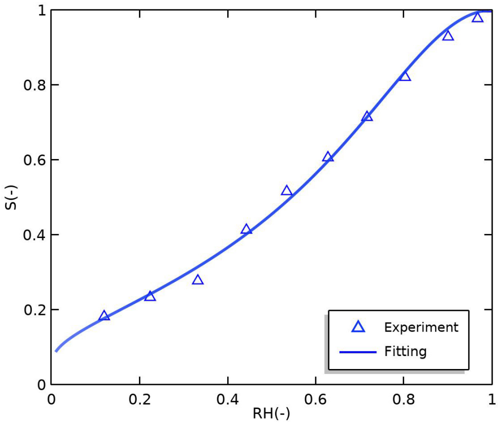

Figure 3.3: Van-Genuchten model fitting for cement paste specimen

3.4 Results analysis

3.4.1 Calculations with the coupled standard model

Firstly, the coupled standard model was used to simulate the drying experiment mentioned above. Intrinsic hydraulic conductivity K_w was determined independently by inversely analyzing the kinetics of mass loss during drying at a constant external relative humidity

$RH^e = 53.5\%$ or $RH^e = 63.2\%$. The parameter optimization is based on the Levenberg-Marquardt (LM) algorithm. The mass loss is calculated by integrating the moisture mass evaporated from the open surface.

As presented in Figure 3.4, the fitting of hydraulic conductivity, which provides mass loss kinetics, have high agreements with corresponding experimental data according to some conditions. Indeed, it must be noticed that the calibrated K_w values show dependency on boundary conditions. When the cement paste is exposed to environment with boundary condition $RH^e = 63.2\%$, $K_w = 2 \times 10^{-15}\ m \cdot s^{-1}$ gives a good fitting of the mass loss with a correlation coefficient $R^2 = 0.980$ (Figure 3.4(a)), but it is not relevant for $RH^e = 53.5\%$. Inversely, when the boundary condition is $RH^e = 53.5\%$, $K_w = 3 \times 10^{-15}\ m \cdot s^{-1}$ gives a good fitting of the mass loss with a correlation coefficient $R^2 = 0.988$ (Figure 3.4(b)), but it is not relevant for $RH^e = 63.2\%$. The relative deviation of these two calibrated results reaches to 33%. Moreover, the same drying experiment has also been simulated previously in literature [141]. Even though, the performance of deformation on moisture transport is ignored, a difference in the permeability coefficient values is also recorded for cement pastes fitted by using two boundary conditions. It is consistent with the present calculations.

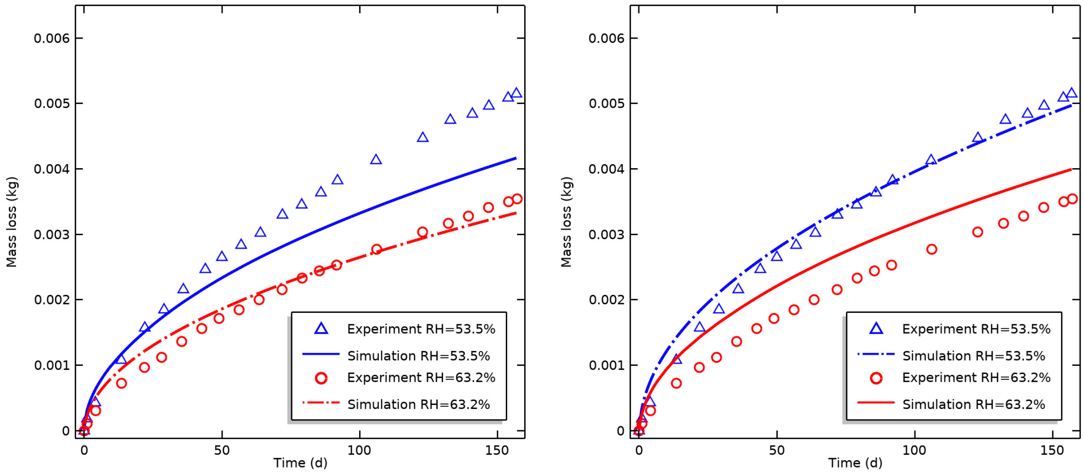

(a) Drying at $K_w = 2 \times 10^{-15} m \cdot s^{-1}$ (b) Drying at $K_w = 3 \times 10^{-15} m \cdot s^{-1}$

Figure 3.4: Comparisons of mass loss curves simulated by coupled standard model at identical permeability conditions with experimental results

Theoretically, K_w should be independent of the boundary condition; the previous researchers attribute such discrepancy to the variability of specimens preparation [141].

Nevertheless, we suppose that the observed discrepancy could due to an added phenomenon, such as the dynamic capillarity effect.

3.4.2 Calculations with the coupled dynamic model

Drainage experiment in sand and soil proved that dynamic effects could accelerate the drainage, which inspires us to think about the same phenomenon may occur for drying in cement-based materials. Dynamic capillarity effect is positively relevant to the time change rate of water saturation $\partial S_w/\partial t$. Obviously, the lower external relative humidity 53.5%, causing a faster drying in porous media, leads to stronger dynamic effects. As the dynamic capillarity effect was ignored until now, the extra part of the mass loss supposed to be caused by dynamic effects can be supplemented by improving the transport coefficient, such as K_w. This is the main reason why the value of K_w fitted at lower drying condition $RH^e = 53.5\%$ is greater than that fitted at higher drying condition $RH^e = 63.2\%$. The consideration of dynamic effects on capillary pressure is required for mass loss kinetics in porous media. In the coupled dynamic model, not only K_w but also dynamic effects coefficient τ plays an important role for calculation of drying process. Similarly to the coupled standard model, the unknown parameters are also determined by fitting mass loss kinetics of drying experiment.

As introduced previously, the investigation of dynamic effects coefficient is limited to quite permeable materials. Both of numerical analyses [36, 107, 108] and experimental methods [10, 23, 91, 109, 110] were carried out to analyze this coefficient. As performed in [130], various numerical experiments for fine and coarse soil indicate τ ranges from 10^7 to $10^{10} kg \cdot m^{-1}s^{-1}$. The values of τ are recorded to range from 1.93×10^6 to $9.95 \times 10^9 kg \cdot m^{-1}s^{-1}$ in alternative references [23, 161]. Otherwise, plenty of studies concerning drainage experiments in sands for air-water systems [21] suggest that values of τ range from 3×10^4 to $5 \times 10^7 kg \cdot m^{-1}s^{-1}$. In total, τ in quite permeable materials, such as sand and soil, is likely in the range of 3×10^4 to $10^{10} kg \cdot m^{-1}s^{-1}$.

The results of coupled dynamic modelings with K_w values 2×10^{-15} and 3×10^{-15} $kg \cdot m^{-1}s^{-1}$ are presented and compared with the corresponding results of coupled standard modelling and experimental data in Figure 3.5(a) and Fig. 3.5(b) respectively. For these

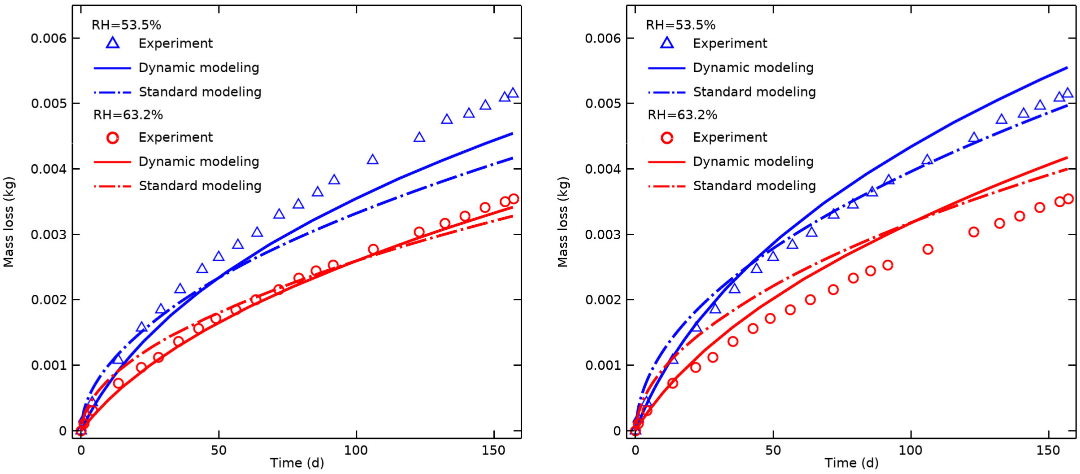

(a) Drying at $K_w = 2 \times 10^{-15} m \cdot s^{-1}$ (b) Drying at $K_w = 3 \times 10^{-15} m \cdot s^{-1}$

Figure 3.5: Comparisons of mass loss curves simulated by coupled dynamic and coupled standard modelings with experimental results

two K_w values, neither dynamic modelling nor standard modelling gives good fitting results for both boundary conditions. The dynamic and standard modelling results show slight deviation for high RH^e value and this deviation becomes significant as RH^e value is low. It implies that dynamic effects are stronger for fast drying.

Indeed, dynamic effects coefficient are dependent on intrinsic permeability, pore connectivity and effective saturation [22, 93, 120]. Several authors also have demonstrated the scale-dependence of dynamic effects [23, 34, 90, 112]. It is difficult to detect coherence between different investigations concerning the impacts of properties of fluids and porous materials on magnitude of τ and how it varies with saturation [100, 109, 130]. Stauffer [93] has presented an empirical formula to estimate τ for soil:

$$\tau = \frac{a\phi\eta_w}{kn}(H_{ce})^2 \tag{3.22}$$

where a is assumed to be constant and equal to 0.1 for quite permeable porous media. H_{ce} and n represent coefficients in the Brooks-Corey formula. Although this empirical formula proved to be limited, we can at least effectively draw a conclusion that the dynamic effects coefficient is inversely proportional to the permeability. Thus, it is appropriate to suppose that the dynamic effects coefficient for weakly permeable porous media, such as cement-based materials, is greater than the largest one observed in soil.

Since the values of τ are difficult to determine, until now there is no well accepted formula to calculate its value. Recently, the drainage experiments [10] observed that $\tau - S_w$ almost follows log-linear function within a certain saturation range. They proposed a function given as $\log_{10}\tau = A(S_0 - S_w) + \log_{10}\tau_0$, in which S_0 and τ_0 are some threshold values and A is the slope of the lines, to fit the $\tau - S_w$ data. We note that we only did preliminary optimizations here. This log-linear function is employed to define the relation $\tau - S_w$. For coupled dynamic modelling, the unknown parameters are determined to provide the modeled mass loss curves equal to the measured data for both boundary conditions. The calibrated parameters are collected in table 3.2.

Table 3.2: Fitting results from inverse analysis of drying kinetics according to coupled dynamic model

$K_w(m \cdot s^{-1})$	$\tau_0(kg \cdot m^{-1}s^{-1})$	A	S_0	$R^2(RH^e = 53.5\%)$	$R^2(RH^e = 63.2\%)$
2.4×10^{-15}	8.91×10^{14}	3.74	0.83	0.992	0.988

In Figure 3.6(a) the mass loss curves obtained from coupled dynamic modelling with adjusted K_w value 2.4×10^{-15} $kg \cdot m^{-1}s^{-1}$ are plotted and compared with the experimental measurements. Even though the same value K_w is used for both boundary conditions, all fitting results are quite good. The $R^2 = 0.992$ for boundary condition $RH^e = 53.5\%$ and $R^2 = 0.988$ for boundary condition $RH^e = 63.2\%$. However, as the same calibrated parameters are used for the case of coupled standard modelling, deviations become significant between modelling mass loss curves and experimental data especially for low ambient relative humidity condition $RH^e = 53.5\%$ (Figure 3.6(b)). Nonetheless, there is no considerable variation between dynamic and non-dynamic modelings for high external relative humidity condition $RH^e = 63.2\%$ (red curves in Figure 3.6). Indeed, the higher external relative humidity induces slower drying. Considering dynamic effects are greatly dependent on drying rate, dynamic capillarity effect is weak for condition $RH^e = 63.2\%$. By comparing Figure 3.6(a) and Figure 3.6(b) and reviewing the poor performance of coupled standard model presented in Figure 3.4, the results computed by coupled standard model are not as good as that obtained from coupled dynamic model. Based on the verifications by the experimental data, it can be concluded that consideration of dynamic effects for moisture transport in cement-based materials is more advanced. The slight discrepancy observed between dynamic modelling curves and experimental data could be attributed to a potential reason that the relative permeability-saturation relationship is not independent and derived from the initial capillary pressure-saturation relationship. However, a constitutive relationship defined under steady-state conditions cannot be applied to transient flow procedures. Nonetheless, we strictly deal with the dynamic effects within the capillary pressure and ignore possible dynamic effects in the relative permeability curves. Another possible reason is that the prescribed log-linear function for $\tau - S_w$ relationship may slightly deviate from the reality. Considering the log-linear function has already given good fitting results and the available experimental data are limited, the improvement for $\tau - S_w$ relationship is arduous but fruitless. In addition, the order of magnitude of dynamic effects coefficient almost reaches to 1×10^{15} which is greater than the maximum one for soil. It is consistent with expectation discussed previously.

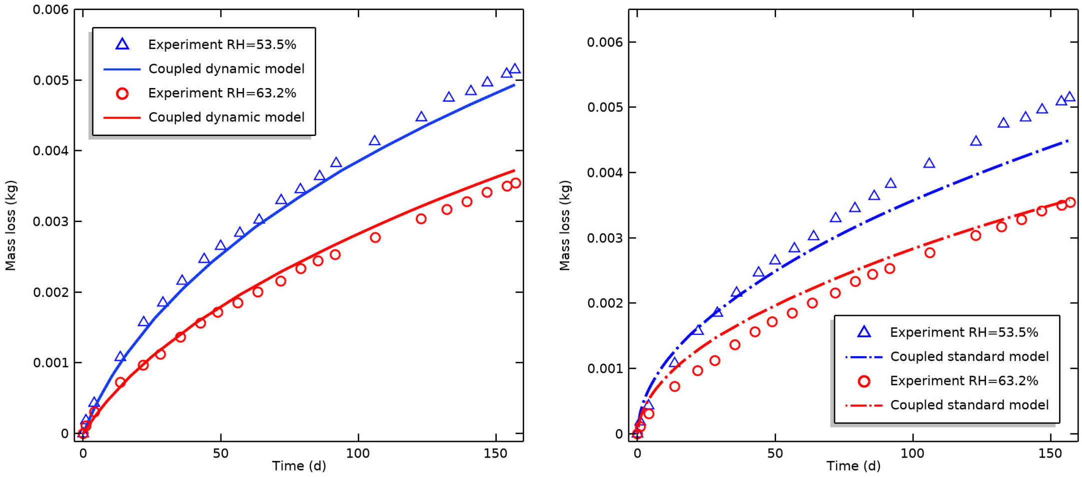

(a) Coupled dynamic modelling

(b) Coupled standard modelling

Figure 3.6: Comparisons of mass loss curves simulated by coupled dynamic and coupled standard modelings with experimental results

3.5 Discussion

3.5.1 Spatiotemporal evolution of saturation

The spatiotemporal evolution of saturation for the studied cases obtained from coupled dynamic modelling is given by the maps in Figure 3.7. In this chapter, we define the part of the material with a saturation disturbed by the variations of RH^e as the penetration depth. As presented in Figure 3.7, the penetration depth increases gradually as time goes by. the comparison of Figure 3.7(a) with Figure 3.7(b) shows that the differences in terms of penetration depth for both boundary conditions are not obvious. However, at the area close to open surface, the saturation obtained from modelling at condition $RH^e = 53.5\%$ is smaller than that obtained from modelling at condition $RH^e = 63.2\%$. The higher the hydric gradient between the external environment and the specimen, the faster the evaporation rate is. It indicates that the low external relative humidity accelerates the evaporation of vapour on open surface. Given the low saturation results in high capillary pressure, which enhances the generation and development of deformation.

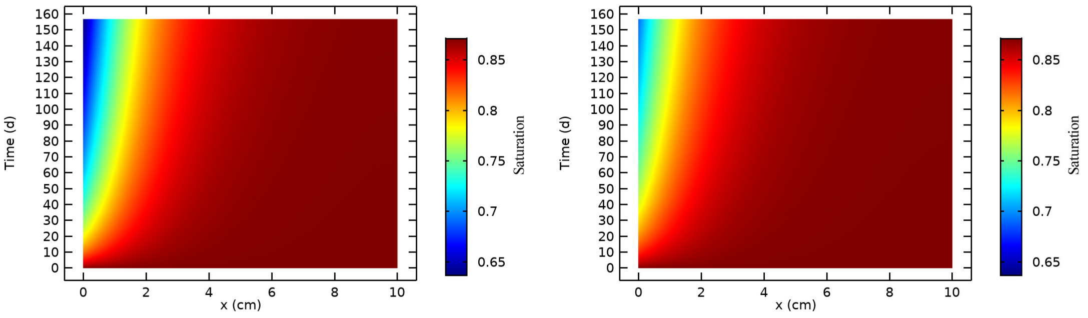

(a) Drying at $RH^e = 53.5\%$

(b) Drying at $RH^e = 63.2\%$

Figure 3.7: Spatiotemporal evolution of the saturation for both boundary conditions

The time change rate of saturation $\partial S_w/\partial t$ is calculated and plotted as a function of time and position in Figure 3.8. As expected, the absolute values of $\partial S_w/\partial t$ are extremely small for weakly permeable materials. The maximum absolute value is found at the position close to open surface during initial stage. As time goes by, the change rate decreases step by step. By comparing Fig. 3.8(a) and Figure 3.8(b), the change rate at condition $RH^e = 53.5\%$ is slightly faster than that at condition $RH^e = 63.2\%$. Indeed, the lower RH^e condition induces higher hydric gradient resulting in fast evaporation. By retrospecting the coupled dynamic model in previous section, the additional term describing the contribution of dynamic effects in dynamic model is greatly dependent on time change rate of saturation. Thus, the faster time change rate of saturation leads to stronger dynamic effects.

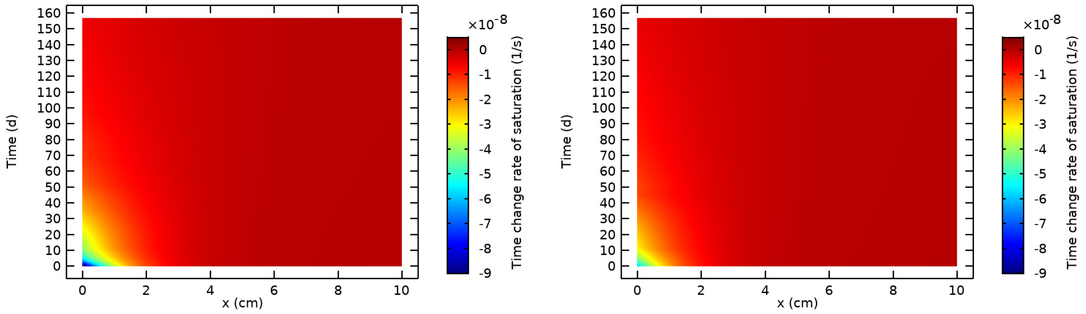

(a) Drying at $RH^e = 53.5\%$

(b) Drying at $RH^e = 63.2\%$

Figure 3.8: Spatiotemporal evolution of the time change rate of saturation for both boundary conditions

3.5.2 Fluid-solid coupling with the consideration of dynamic effects

After the verification of the dynamic coupled model, the performances of dynamic effects on coupling of moisture transport are discussed in this section. The investigations focus on the drying procedure at condition $RH^e = 53.5\%$, since the low RH^e condition results in a relatively higher drying rate (Figure 3.8) and lower saturation state, inducing more significant dynamic capillarity effect and deformation. The investigation is implemented on the basis of results comparison regarding coupled dynamic modelling, uncoupled dynamic modelling and coupled standard modelling.

The result comparison between dynamic coupled modelling and dynamic uncoupled modelling aims to study the possible impact of deformation on moisture transport. The coupled dynamic model takes into account the effect of the skeleton deformation on moisture state evolution, while the uncoupled dynamic modelling totally neglects it. As presented in Figure 3.9, the mass loss curve of drying kinetics at $RH^e = 53.5\%$ obtained from uncoupled dynamic modelling are plotted and compared with that simulated by coupled dynamic model.

Obviously, the mass loss curves of both simulations are almost identical. It indicates that the influence of deformation on moisture transport is limited. Indeed, the effective hydraulic conductivity is the main factor to determine moisture transport in porous media. One possible reason behind this phenomenon is that the contribution of deformation on the decrease of effective hydraulic conductivity is insignificant. In the dynamic modelling,

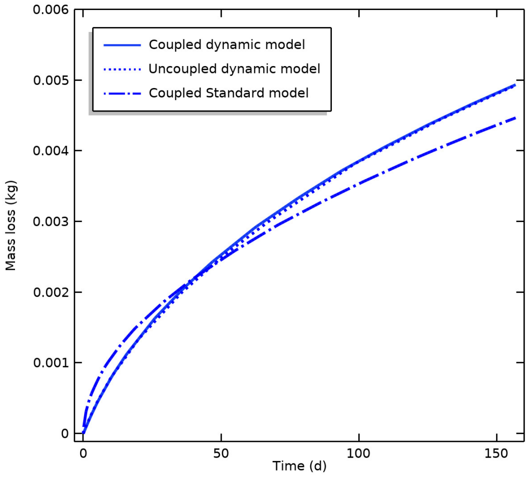

Figure 3.9: Comparisons of mass loss curves simulated by coupled dynamic modelling with results of uncoupled dynamic modelling and coupled standard modelling for $RH^e = 53.5\%$ condition.

after reach a certain time point, the mass loss has always higher values than the standard modelling. Considering capillary pressure is the driving force relevant to moisture transport, it confirms once again that dynamic effects on capillary pressure have non-negligible influence on drying process. Indeed, the observed phenomenon has clear theory foundation. As mentioned previously, the last three terms of coupled dynamic model (Eq. 3.18) have taken into consideration the contribution of dynamic effects on Darciean advection and Fickian diffusion. The fast drying induced by current boundary condition leads the dynamic effects can no longer be ignored.

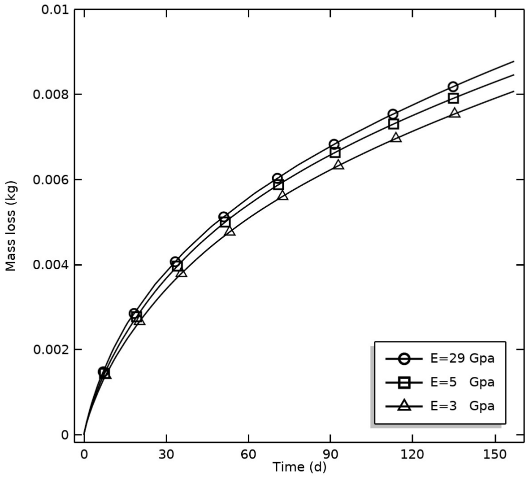

Figure 3.10: Modelling mass loss curves at condition $RH^e = 10\%$.

Indeed, the proposed model can handle system experiencing significant deformation. Now, we propose to study fictitious experiments by using coupled dynamic model. In addition to giving an extremely low ambient relative humidity condition $RH^e = 10\%$ and providing additional two smaller Young's modulus values 3 and 5 GPa, the experimental setup and the cement paste and fluid properties almost remain unchanged. In this way, considerable deformation of cement paste occurs and then makes it possible to investigate the potential impact of deformation on drying procedure. We note that we only did preliminary qualitative analysis here. The mass loss curves of the given system simulated by different values of Young's modulus are presented in Figure 3.10. The observed discrepancy between these three curves intuitively indicates that the deformation has an impact on moisture transport under extreme conditions.

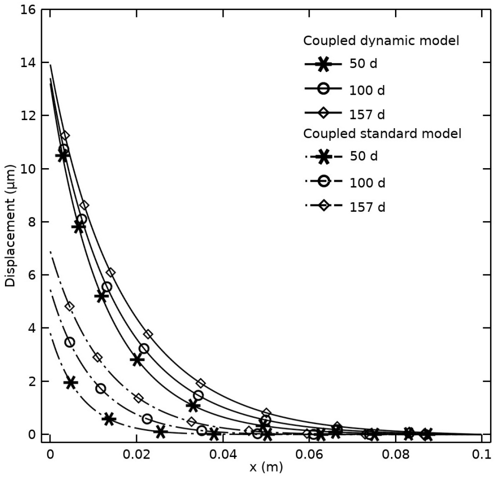

Figure 3.11: Comparison of axial displacement between dynamic and standard modelling.

The numerical results of the axial displacement simulated by both dynamic and standard modelings are plotted and compared at various points of time during drying process in Figure 3.11. Generally, both axial displacements increase gradually from sealed end to open surface. The slopes of these curves are increasing as position closes to open surface. However, axial displacement obtained from coupled dynamic modelling is always greater than that simulated by the standard coupled model along the axis. It indicates that dynamic effects could cause additional deformation for porous media during drying. Moreover, the position closer to the open surface, the greater deviation is observed between dynamic and standard modelling results. A rational explanation is given as follows. The dynamic term in constitutive model (equation 3.19) implies the contribution of dynamic effects on deformation generation. Theoretically, the strength of dynamic effects is proportional to time change rate of saturation and this rate is relatively high in the vicinity of the open surface of specimen during initial stage (Figure 3.8). Thus, it can be concluded that dynamic effects have a non-negligible impact on deformation under fast drying condition. Thereafter, the distributions of effective hydraulic conductivity simulated by both models are compared in Figure 3.12. Since the variation of hydraulic conductivity is relevant to deform according to equation (3.5), a phenomenon similar to the shrinkage evolution is founded. Although the maximum reduction of hydraulic conductivity is observed near open surface; this reduction is still relatively small.

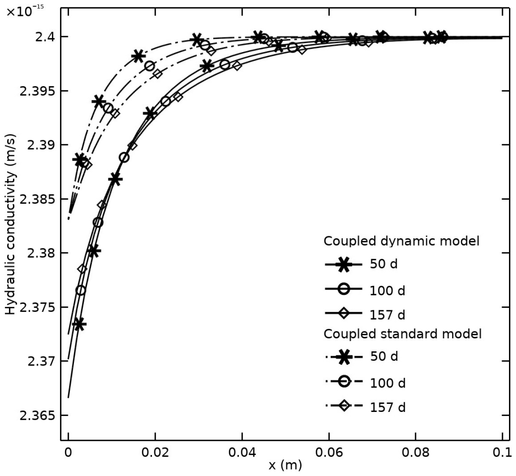

Figure 3.12: Comparison of effective hydraulic conductivity between dynamic and standard modelling.

3.6 Concluding remarks

In this chapter, a coupled dynamic model, which implements the dynamic capillarity effect and fluid-solid coupling into moisture transport, has been proposed and employed to simulate a drying experiment. The simulations in the case of coupled standard modelling (no dynamic effects) and uncoupled dynamic modelling (no fluid-solid coupling) have also been performed. Based on the verifications by the experimental data, the following conclusions can be drawn:

1) Compared with the traditional standard model, the dynamic model is more advanced and complete since the dynamic capillarity effect for the Darciean advection and

Fickian diffusion has been considered. In addition, the investigation on the values of dynamic effects coefficient for cement-based materials is pioneering. The obtained values are greater than the values observed in soil, which are consistent with theoretical predictions.

2) Comparisons with measured mass loss curves for cement paste, drying experiments show that modelling taking dynamic effects into account obviously provides better results than the non-dynamic modelling. The main reason is that the dynamic model could predict the capillary pressure closer to actual value for moisture transport, especially in the condition that the vicinity of the open surface is exposed to variations of RH^e.

3) The mass loss curve of drying kinetics at $RH^e = 53.5\%$ obtained from coupled dynamic modelling, in which skeleton deformation is considered, has a good agreement like that obtained from uncoupled dynamic modelling, in which no deformation is allowed. It reveals that the influence of skeleton deformation on moisture transport is negligible for this kind of cement paste.

4) According to the comparisons performed in this chapter, it is explicit that dynamic effects could cause additional unexpected displacement and increase the possibility of cracking risk, when the material strength is weak and/or the environmental conditions are extremes. Thus, dynamic capillarity effect should be taken into account for predicting durability of cement-based materials under low ambient relative humidity condition.

Chapter 4

Contribution of the dynamic capillary pressure and interface energy on fast drying of hardening cement-based materials

4.1 Background

The durability of cement-based materials is significantly affected by the environmental conditions. As the world continues to become warmer, the ambient relative humidity could even decrease to 20%. This extreme condition directly impacts the moisture transport in porous materials. As mentioned in the last chapter, the moisture transport in weakly permeable materials mainly consists of Darciean water flow and Fickean vapour diffusion. Moreover, by-also known moisture transport determines the evolution of capillary pressure, which is the main cause of the delayed deformations and occurrence of micro-cracks in cement-based materials [16, 115]. The shrinkage due to drying has typically been attributed to three primary mechanisms including changes in capillary pressure, disjoining pressure and pressure of interfacial energy [85, 88] at extremely low ambient relative humidity conditions. Bishop [84] originally put forward an elastic constitutive equation to simulate shrinkage in unsaturated condition. Since pioneering work of Wittmann [80] and

Bažant [162], considerable investigations taking into account thermodynamics have been implemented in drying shrinkage. Coussy et al. [85] proposes an upgraded drying shrinkage model in which the contribution of interfacial energy on equivalent pore pressure is highlighted. Plenty of studies indicate that this contribution should be appreciated especially for low ambient relative humidity [11, 58]. Moreover, since cement-based materials exhibits viscoelastic effects at early stage, several studies [11, 88, 147, 163, 164] have proposed poroviscoelastic models which incorporate the main mechanisms for shrinkage based on the experimental results. Thus the shrinkage model proposed in former chapters is limited concerning hardening cement-based materials.

On the other hand, in order to verify the availability and performance of these models, the numerical modelling results should be in agreement with corresponding experimental results. However, previous studies were not able to verify moisture transport and drying shrinkage simultaneously. It might be due to the limitation of model or lack of experimental data and premature computational approaches. Zhang et al. [141, 151] have adopted a standard moisture transport model to fit the measured dying kinetics, while the verification for drying shrinkage is totally neglected. In contrast, Samouh et al. [11] merely fit measured drying shrinkage without fitting water mass loss. In addition, durability risks may be underestimated with dynamic capillarity effect omitted. However, the literature on dynamic effects is limited to unsaturated fluid flow for the soils and sands. Implementing the dynamic capillarity effect into coupling of moisture transport and drying shrinkage for hardening cement-based materials exposed to low ambient relative humidity condition is an advanced mechanism and urgently needed.

This chapter aims to develop an appropriate dynamic model to simulate the evolution of moisture transport and drying shrinkage of hardening cement-based materials under extreme ambient relative humidity conditions. In this case, the mechanical behaviour of porous materials is viscoelastic and interface energy pressure also has non-negligible impact on shrinkage development. Standard and dynamic modelling approaches are studied through comparisons with documented experimental data for verification. Regarding the structure of this chapter, an advanced model incorporating dynamic capillarity effect into moisture transport and drying shrinkage is firstly introduced on the basis of a well-known standard model. Secondly, a drying shrinkage experiment provided in [11] is employed to verify the performances of both standard and dynamic model. Modelling results based on standard and dynamic modelling are presented and compared. The comparison of solutions obtained from different modelling methods allows to recognize the non-negligible contribution of interface energy effect and dynamic capillarity effect on drying procedure. Finally, the strong agreement between numerical modelling results and corresponding experimental data confirms the reliability of the proposed dynamic model.

4.2 The derivation of dynamic physical model

4.2.1 Physical model for moisture transport from standard to dynamic

The governing model of unsaturated water-air flow for porous media is derived from the mass conservation principle. An efficient drying model based on the assumptions that the pressure of gas mixture is constant and the liquid water remains incompressible has been chosen. As for cement-based materials, the moisture transport is not only dependent on the water advection, but also on the vapour diffusion. The mass conservation equations of liquid water and water vapour reduce to a simplified equation regarding moisture, i.e. including liquid water and water vapour [151]. Substitution of the extended Darcy's equation which governs advection of liquid water and Fick's equation which governs vapour diffusion into this simplified mass conservation equation results in the typical drying model [28]:

$$\frac{\partial S_w}{\partial t} + \nabla \cdot \left(-\frac{k k_{rw}\left(S_w\right)}{\phi \eta_w} \nabla P_w - \frac{D_0 f\left(S_w, \phi\right)}{\phi \rho_w} \nabla \rho_v \right) = 0, \tag{4.1}$$

where S_w, k, k_{rw}, ϕ, η_w, P_w, ρ_w, ρ_v, D_0 and $f\left(S_w, \phi\right)$ represent water saturation, permeability, relative permeability, porosity, water viscosity, water pressure, water density, vapour density, vapour diffusion coefficient in air and resistance factor of pore network for gaseous diffusion respectively. Resistance factor $f\left(S_w, \phi\right)$ has a functional dependency on S_w and ϕ.

In the case where equilibrium between liquid water and water vapour is satisfied, the value of capillary pressure can be predicted by Kelvin's equation:

$$P_c = -\frac{\rho_w R T}{M_w} \ln \frac{P_v}{P_{vs}}, \tag{4.2}$$

where R, T, P_v, P_{vs} and M_w represent universal gas constant ($8.314\ J \cdot mol^{-1} \cdot K^{-1}$), absolute temperature, vapour pressure, saturated vapour pressure and water molar mass respectively. Meanwhile, during the drying process of a given porous media, the relationship between capillary pressure and saturation could be expressed by van Genuchten model Eq (4.3). The van Genuchten model is also applicable for cement-based materials [28, 165], since the relationship of capillary pressure versus saturation can be derived from the sorption isotherms according to Kelvin's equation. The evolution of k_{rw} also depends on the saturation; and Genuchten-Mualem equation is adopted to describe it following the previous literature [28].

$$P_c\left(S_w\right) = \alpha\left({S_w}^{-1/m} - 1\right)^{1-m}, \tag{4.3}$$

$$k_{rw}\left(S_w\right) = {S_w}^{l}\left[1 - \left(1 - {S_w}^{1/m}\right)^{m}\right]^{2}, \tag{4.4}$$

where α and m are fitting parameters and relevant to pore-size distribution. l accounts for tortuous effects and $l = 0.5$ is assigned to cement-based materials. Considering the water vapour is regarded as ideal gas and the pressure of gas mixture is negligible compared with capillary pressure, the moisture transport model Eq. (4.1) evolves to:

$$\frac{\partial S_w}{\partial t} = \nabla \cdot \left\{\left[-\frac{k k_{rw}}{\phi \eta_w} - \left(\frac{M_v}{\rho_w R T}\right)^2 D_0 f\left(S, \phi\right) \frac{P_{vs} R H}{\phi}\right] \nabla P_c\right\}, \tag{4.5}$$

where M_v and RH represent vapour molar mass $\left(18 \times 10^{-3} kg \cdot mol^{-1}\right)$ and relative humidity. For cement-based materials, this moisture transport model develops to a time evolution of saturation model presented as a 'diffusion' approach with an apparent diffusion coefficient D_a [145, 166]:

$$\frac{\partial S_w}{\partial t} = \nabla \cdot \left(D_a \nabla S_w\right), \tag{4.6}$$

$$D_a = D_w + D_v, \tag{4.7}$$

where D_a consists of two components including diffusion coefficient of liquid water D_w and diffusion coefficient of water vapour D_v. Both of them are given as below:

$$D_w = -\frac{k k_{rw}}{\eta_w \phi} \frac{d P_c}{d S_w}, \tag{4.8}$$

$$D_v = -\left(\frac{M_v}{\rho_w R T}\right)^2 D_0 f\left(S_w, \phi\right) \frac{P_{vs} R H}{\phi} \frac{d P_c}{d S_w}. \tag{4.9}$$

It is admitted that there exists dynamic effects on capillary pressure. In the case of modelling with dynamic effects, the dynamic capillary pressure P_c^{dyn} should be applied to replace the static capillary pressure P_c in moisture transport model. Thus, the model for saturation evolution, taking into account dynamic capillarity effect, is obtained:

$$\frac{\partial S_w}{\partial t} = \nabla \cdot \left\{ D_a \left[\nabla S_w - \frac{\partial S_w}{\partial P_c} \nabla \left(\tau \frac{\partial S_w}{\partial t} \right) \right] \right\}. \tag{4.10}$$

Since the diffusion coefficient of water vapour D_v includes the parameter of $P_v = P_{vs} \cdot RH$ which is a function capillary pressure, it means that the diffusion coefficient should also be influenced by dynamic effects. Thus, D_v in D_a of above model should be substituted by $D_v{}'$, where $D_v{}' = D_v e^{\frac{M_v \tau \frac{\partial S_w}{\partial t}}{\rho_w RT}}$.

Under given a certain initial state and boundary conditions, the solution of moisture transport problem can be obtained. The moisture evaporation on the surface of porous media is greatly affected by the interaction between porous media and the surrounding environment. It is the external moisture gradient in the vicinity of the open surface of porous media which governs the moisture transport from inner to surface. The Neumann-type boundary condition, which takes this given gradient into account, is used frequently [141, 151, 157]. The specific formula is presented as

$$w = \phi S_w^0 E_v \left(P_v^o - P_v^e \right), \tag{4.11}$$

where the term w indicates the mass flux of moisture; P_v^0 and S_w^0 are vapour pressure and water saturation within the media near the surface. P_v^e is the surrounding vapour pressure. The moisture exchange between the ambient environment and the porous media is mainly governed by emissivity E_v. A value $E_v = 2.58 \times 10^{-8} kg \cdot m^{-2} \cdot s^{-1} \cdot Pa^{-1}$ is measured at room temperature with no air flow [158]. The term ϕS_w^0 represents the influence due to the decrease of wet surface when exposed to environment with low RH.

4.2.2 Dynamic viscoelastic drying shrinkage model

Based on standard macroscopic thermodynamics and dynamic effects on capillary pressure, we focus on incorporating surface energy effects and dynamic effects into drying shrinkage model of viscoelastic concrete. The porous medium, an open thermodynamic system, exchanges moisture mass with the surrounding environment. For reversible and isothermal evolutions, the Helmholtz free energy of an open system Ψ is given by the following relation:

$$\sigma_{ij} d\varepsilon_{ij} + \mu_w dm_w + \mu_g dm_g - d\Psi = 0, \tag{4.12}$$

where σ_{ij} and ε_{ij} are stress tensor and strain tensor respectively and $m_{\alpha=w,g}$ present the mass per unit of initial volume of the porous sample for liquid water and gas mixture in sequence. There exists a relation $m_\alpha = \rho_\alpha S_\alpha \phi$, where ρ_α, S_α are the density and saturation of α-component and ϕ is porosity. $\mu_{\alpha=w,a,v}$ are chemical potential per mass unit for corresponding components. The specific chemical potential μ_α gives as below:

$$\mu_\alpha = \psi_\alpha + \frac{P_\alpha}{\rho_\alpha}, \tag{4.13}$$

where ψ_α and P_α indicate the Helmholtz free energy per mass unit and pressure of the α-component. There is a relation $d\mu_\alpha = dP_\alpha/\rho_\alpha$ according to standard thermodynamics.

The free energy of solid matrix and interfaces Ψ_s is attained by eliminating the Helmholtz free energy of the fluid phases from Ψ based on the additive character of energy.

$$\Psi_s = \Psi - m_w \psi_w - m_g \psi_g. \tag{4.14}$$

By incorporating the Eqs (4.12)-(4.14) and with the help of the potential relations mentioned above, the energy balance expression with respect to the skeleton including the interfaces is given as follows:

$$\sigma_{ij} \varepsilon_{ij} + \sum_\alpha P_\alpha d\phi_\alpha - d\Psi_s = 0. \tag{4.15}$$

Since $\phi_\alpha = \phi S_\alpha$ and $d\left(\phi S_\alpha\right) = S_\alpha d\phi + \phi dS_\alpha$, the above energy balance expression evolves into

$$\sigma_{ij} d\varepsilon_{ij} + P^* d\phi - \phi P_c dS_w - d\Psi_s = 0. \tag{4.16}$$

As for partially saturated porous media with gas mixture and fluid water, the average pore pressure equals to $P^* = S_w P_w + (1 - S_w) P_g$. For reversible evolutions that energy dissipations are neglected, the Eq. (4.16) yields following state equations:

$$\sigma_{ij} = \frac{\partial \Psi_s}{\partial \varepsilon_{ij}}; P^* = \frac{\partial \Psi_s}{\partial \phi}; \phi P_c = \frac{\partial \Psi_s}{\partial S_w}. \tag{4.17}$$

In the case of non-deformable and isothermal, where $\varepsilon_{ij} = 0$, $\phi = \phi_0$, the free energy of solid matrix and interfaces Ψ_s reduce to interfacial energy $\phi_0 U$ which accounts for the energy of all interfaces including liquid water-gas mixture, liquid water-solid and gas mixture-solid interface. Thus, the above state equations turn into $P_c = \frac{\partial U}{\partial S_w}$. The interfacial energy as function of saturation S_w equals to:

$$U\left(S_w\right) = \int_{S_w}^{1} P_c\left(S\right) dS, \tag{4.18}$$

where S is the dummy variable of saturation. Since the capillary pressure is independent of skeleton deformation, this identification is applicable for deformable porous media. An integration of the last state equation in Eq. (4.17), allows to express the free energy as below:

$$\Psi_s = \psi_s\left(\varepsilon_{ij}, \phi\right) + \phi \int_{S_w}^{1} P_c\left(S\right) dS. \tag{4.19}$$

Here, free energy of the solid matrix $\psi_s\left(\varepsilon_{ij}, \phi\right)$ is expressed independently from the interfacial energy U. Substitution of Eq. (4.19) into Eq. (4.16) and taking into account the last state equation in Eq. (4.17) yields:

$$\sigma_{ij} d\varepsilon_{ij} + \pi d\phi - d\psi_s = 0, \tag{4.20}$$

where $\pi = P^* - \int_{S_w}^{1} P_c\left(S\right) dS$. As for saturated porous media with water pressure p, $S_w = 1$, $P^* = p$ and $\Psi_s = \psi_s$ are satisfied. Thus, the Eq. (4.16) reduces to

$$\sigma_{ij} d\varepsilon_{ij} + p d\phi - d\psi_s = 0. \tag{4.21}$$

Comparing Eq. (4.20) and Eq. (4.21), the pressure π serves the same role concerning the solid matrix as pressure p performs in fully saturated condition. Hence, π is defined as the equivalent pore pressure which takes into account the effects of surface stresses on the strain of the solid matrix. For the drying of cement-based materials, the pressure of gas mixture is usually assumed to keep constant at atmospheric pressure. Indeed, the atmospheric pressure is negligible compared with capillary pressure, which leads to $P^* = -S_w P_c$. As mentioned previously, the P_c is related to S_w, which is known as the capillary pressure curve. However, the experimental data $P_c - S_w$, employed for the water retention model fitting are measured in the quasi-static condition, in which, the dynamic effects on capillary pressure have been totally ignored. Since there exists dynamic capillarity effect, it leads to $P_c^{dyn} = P_g - P_w = P_c - \tau \frac{\partial S_w}{\partial t}$. If dynamic capillarity effect is considered, the average pore pressure is given as $P^* = -S_w\left(P_c - \tau \frac{\partial S_w}{\partial t}\right)$. After the discussion above, the contribution of dynamic capillarity effect leads the equivalent pore pressure to be rewritten as follows:

$$\pi = -S_w\left(P_c - \tau\frac{\partial S_w}{\partial t}\right) - \int_{S_w}^{1} P_c\left(S\right)dS. \tag{4.22}$$

The change of equivalent pore pressure determines the generation and development of shrinkage. In the absence of externally applied pressure, a model that applies viscoelasticity to predict the drying shrinkage of cement-based materials with the consideration of dynamic capillarity effect is presented as below [88]:

$$\varepsilon\left(t\right) = \int_0^t \frac{\partial\pi\left(t'\right)}{\partial t'}\left(3\left(1-2\nu_p\right)J_p\left(t-t'\right) - \frac{1}{K_s}\right)dt', \tag{4.23}$$

where the ν_p, K_s, J_p and t' present Poisson's ratio of the porous body, bulk modulus of the solid, uniaxial viscoelastic compliance of the porous body and dummy time variable, respectively. J_p can be calculated, analogous to the approach in [89], as the inverse of the uniaxial relaxation modulus of the porous body $E_p(t)$ given as:

$$E_p\left(t\right) = \left(p\cdot e^{-t/\iota} + \left(1-p\right)\right)\cdot E_0, \tag{4.24}$$

where E_0 is the instantaneous Young's modulus; p and ι are relaxation parameter and viscoelastic relaxation time, respectively.

In particular situations, the compliance provided by classic creep tests or by existing models is not precise in the studied cases [167]. If the Young's modulus of specimens is monitored directly under the tension caused by drying, part of aging viscoelastic behaviour has already been considered. When the evolution of Young's modulus $E\left(t\right)$ is measured during drying shrinkage procedure and fitted by an appropriate formula Eq. (4.25).

$$E\left(t, t_0\right) = \frac{t-t_0}{\left(t-t_0\right)+\zeta}E^{\infty}, \tag{4.25}$$

where E^{∞} and ζ are fitting parameters, some phenomena behind the viscous behaviour such as stress relaxation are incorporated. t_0 is the age at the start of experiment. Herein, since the evolution of Young's modulus versus time of the selected drying experiment has been implemented, it is not indispensible to express the viscoelastic strain with the compliance term in free shrinkage model. Thus, the free drying shrinkage can be approximated by the following model Eq (4.26). This is a deliberate approach to avoid misguiding the audience with the typical term of compliance which is associated to the imposed external stress [11].

$$\varepsilon_v\left(t\right) = \int_{t_0}^t \frac{\partial\pi\left(t'\right)}{\partial t}\left(\frac{3\left(1-2\nu_p\right)}{E\left(t'\right)} - \frac{1}{K_s}\right)dt', \tag{4.26}$$

4.3 Presentation of the experimental tests

The experimental data was obtained from Samouh et al. [11]. The self-compacting concrete (SCC) mixture specimens subjected to different ambient relative humidity conditions $RH^e = 30\%$ and 70% were used to verify the models. The proportions of the material are gathered in Table 4.1.

Table 4.1: Mixture design for the SCC

SCC	Value (kg/m^3)
Gravel (amphibolite) 10/14 (G)	290
Gravel (amphibolite) 6/10 (G)	550
Sand 0/4 (S)	780
Portland CEM I 52.5 N (C)	291
Limestone filler (A)	248
Superplastizer	2.8
Effective water content (W)	205
V_G/V_S	0.92
W/C	0.7
$W/(C+A)$	0.38
Paste volume (l)	394
Porosity	0.14
Initial RH $(\%)$	100

Cylindrical specimens were prepared to monitor the mass loss of moisture and the drying shrinkage of solid. The materials were cast in cylindrical moulds with dimension $\Phi\ 7.8 \times 28$ cm^2. Prior to experiments, all studied specimens have been sealed for curing for one-day. After the moulds have been released, all of them were removed to a climatic chamber with room temperature $T = 20°C$ and one of the studied external relative humidities 30% and 70%. A schematic view of the shrinkage experiments is shown in Fig. 4.1.

The drying shrinkage is known as the difference between the measured total shrinkage and autogenous shrinkage [168, 169]. Both total and autogenous shrinkage were measured by

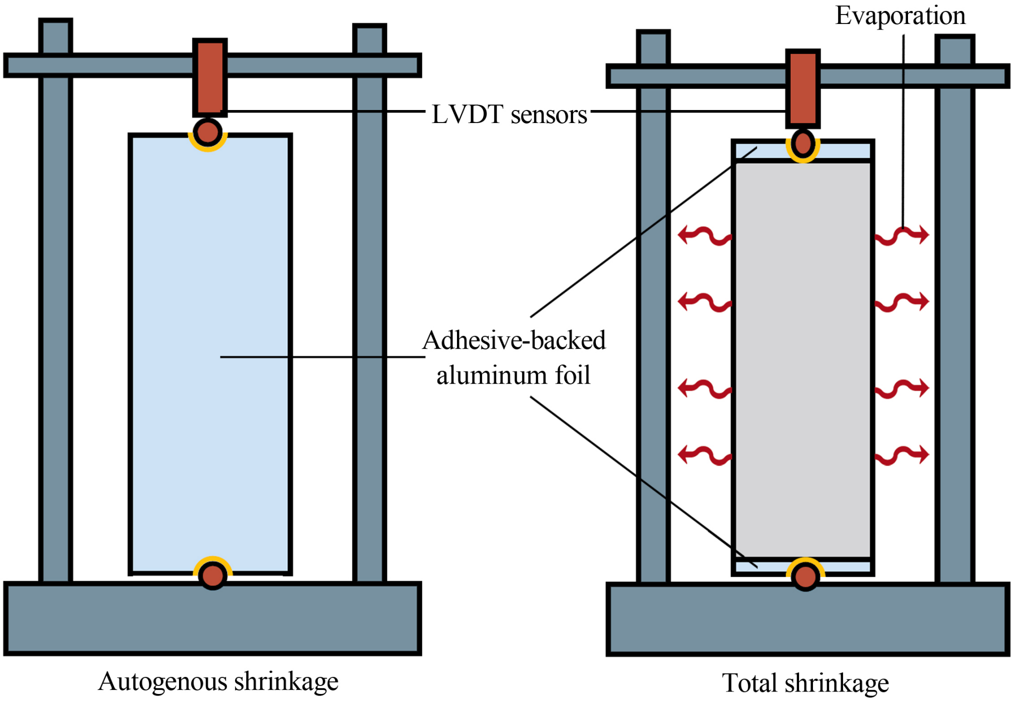

Figure 4.1: A schematic view of the shrinkage experiments (reproduced from [11])

LVDT sensors. For total shrinkage, merely the side surface was open for moisture exchanges with surrounding environment, since the top and bottom of these cylinders were sealed by adhesive-backed aluminum foil. It ensures that the moisture transport occurs in two dimensions. Given the autogenous shrinkage is induced by hydration and self-desiccation, specimens were totally sealed in order to monitor accurate autogenous shrinkage values. The mass loss values were obtained by weighing the specimens at intervals. The specific descriptions of the mass loss and shrinkage measurements were documented in reference [11].

On the other hand, the mechanical properties of SCC mixture were obtained by monitoring the specimens ($\Phi = 11 \times 22\ cm^2$) with the identical initial and boundary conditions as of these shrinkage specimens. The Poisson's ratio is $\nu^c = 0.2$ and the bulk modulus for the solid phase is $K_s = 46\ GPa$. The evolution of Young's modulus was also recorded and fitted by an appropriate model Eq. (4.25). A part of the aging viscoelastic behaviour has been considered as the Eq. (4.25) is calibrated on specimens under the tension stress induced by drying shrinkage. Hence, the values of fitting parameters for Young's modulus collected in Table 4.2 incorporate some phenomena behind the viscous behaviour like stress relaxation caused by surface microcracking [11].

Table 4.2: Fitting parameters for the Young's modulus evolution [20]

Fitting Paremeters	$RH^e = 30\%$	$RH^e = 70\%$
$E^\infty\ (GPa)$	28.2	31.8
ζ (days)	0.7094	0.7292

4.4 Presentation of the numerical simulation

In this chapter, both standard and dynamic models are used to simulate the identical drying shrinkage experiment. Standard model, in which dynamic effects on capillary pressure are neglected, can be easily achieved by removing the corresponding terms related to dynamic capillarity effect in dynamic model Eqs. (4.10) and (4.26). To solve the physical models governing the spatiotemporal evolution of saturation and drying shrinkage, appropriate algorithm has to be employed. For non-linear moisture transport model, the spatial discretization is implemented by a finite element method (FEM). An implicit approximation (Back Euler Method) is adopted in time step to guarantee the stability of the scheme. To solve the partial differential equation with high efficient, the free time steps are taken on the basis of the convergence rate. Since the generation and development of drying shrinkage is determined by the evolution of moisture transport, the spatiotemporal evolution of drying shrinkage is obtained by coupling the results of moisture transport modelling with drying shrinkage model.

4.4.1 Determination of transport coefficient and isotherm desorption curves

The first step for modelling the mass loss and drying shrinkage is to fix the hydric state of the investigated specimen. Indeed, the variation of the degree of saturation is dependent on diffusion coefficient of water vapour D_v and diffusion coefficient of liquid water D_w. The $f\left(S, \phi\right)$ in Eq. (4.9) is resistance factor, which indicates the negative effect caused by the connectivity and tortuosity of the pore network and the existence of solid and liquid phases on water vapour diffusion. Based on theoretical concepts, Millington [153] deduces an equation for granular materials given as:

$$f\left(S_w,\phi\right)=\phi^{x_d}(1-S_w)^{x_d+2}. \tag{4.27}$$

The author suggests that parameter x_d equals to 4/3 for soils. Since cementitious materials are less porous than soils, the resistance to water-vapour diffusion is more powerful in cementitious materials. According to the fitting of experimental data for concrete and mortars implemented by Thiéry et al. [170], $x_d = 2.74$ is recommended. Another important transport coefficient is permeability which determines the diffusion coefficient of liquid water as presented in Eq. (4.8). Indeed, the liquid water transports in the form of advection. Due to the lack of precise values directly obtained from experimental monitoring, the permeability is determined by inversely analyzing the kinetics of mass loss during drying experiment at a constant RH^e condition.

In addition, in order to solve the model, isothermal desorption curves, which link the water saturation to the capillary pressure and equivalent pore pressure, have to be determined for various study cases. The representative isothermal desorption curves (also called water retention curves) are hard to achieve experimentally, since the drying tests last for a long duration and the results only characterize the behaviour and property of mature concrete. For studied cases, the initial condition has significant impact on drying shrinkage since they affect the development of hydration. An appropriate relation van-Genuchten model Eq. (4.3) has been adopted to express the capillary pressure as a function of the computed internal saturation. The parameters α and m are determined preliminarily by inversely analyzing the mass loss kinetics. The specific initial values of calibrated parameters are collected in Table 4.3. The static model has been used at this step.

Table 4.3: Fitting results from inverse analysis of mass loss kinetics

RH^e	$k(m^2)$	$\alpha(MPa)$	m
30%	7.653×10^{-19}	3.21	0.308
70%	2.582×10^{-17}	0.96	0.123

As presented in Fig. 4.2(a), these calibrated parameters provide simulated mass loss curves have high agreements with corresponding experimental data for both boundary conditions.

However, as the same values of these parameters are employed to simulate the drying shrinkage, significant discrepancy is observed for condition $RH^e = 30\%$ (see Fig. 4.2(b)). Hence, further optimization of parameters is necessary.

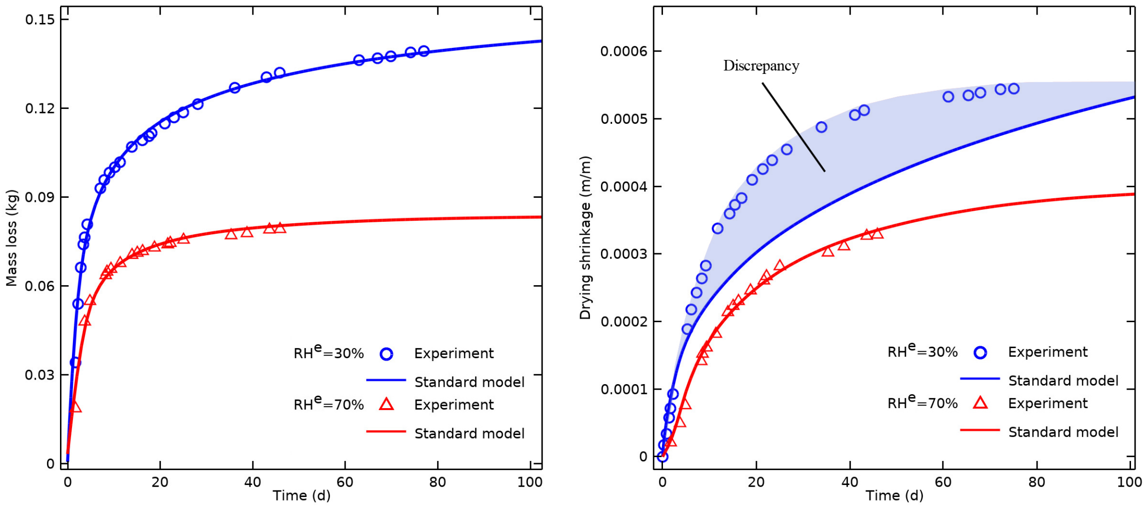

(a) Kinetics of mass loss

(b) Space average shrinkage

Figure 4.2: Comparisons of modelling results simulated by standard model with corresponding experimental results

4.4.2 Calibration of parameters for the simulation of shrinkage

The drying shrinkage experiment at condition $RH^e = 30\%$ is chosen to investigate the sensitivity of modelling results regarding the parameters k, m and α. In addition to changing the value of α, all other conditions remain consistent in each simulation. Qualitatively, parameters k and m play predominant roles for the calculation of mass loss curves, while α has very limited influence. It is verified by the phenomenon shown in Fig. 4.3(a) that the variation is negligible for the modelling results of mass loss obtained from different input α values at condition $RH^e = 30\%$. Theoretically, α determines the magnitude of the equivalent pore pressure which is the driving force of shrinkage development. The shrinkage strains simulated by various values of α are presented and compared in Fig. 4.3(b). The significant variation between them proves that α has significant impact on shrinkage. Adjusting the value of α can however improve the shape of the strains curves. Therefore, the following fitting procedure is essential. We let k and m remain constant at

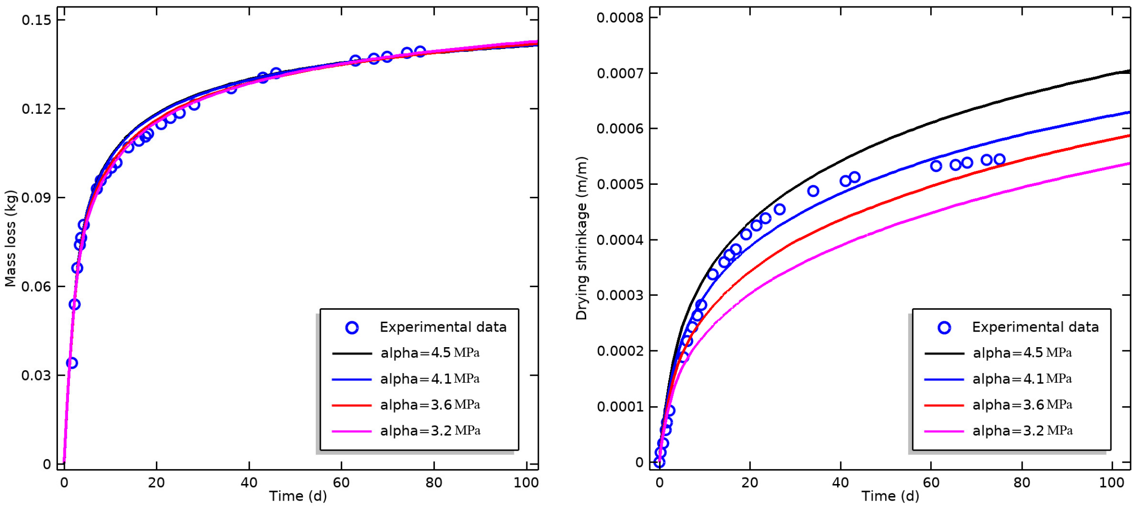

(a) Kinetics of mass loss (b) Space average shrinkage

Figure 4.3: Comparisons of modelling results obtained from different α values with experimental data at condition $RH^e = 30\%$

the values determined by inversely fitting the kinetics of mass loss, then fit the measured average strain by adjusting α again. All fitted parameters are gathered in Table 4.4.

Table 4.4: Fitting results from inverse analysis of mass loss and drying shrinkage

RH^e	$k(m^2)$	$\alpha(MPa)$	m
30%	7.653×10^{-19}	4.08	0.308
70%	2.582×10^{-17}	0.70	0.123

The fitting results obtained from different ambient relative humidity conditions are not unique. One important reason is that the hydration is dependent on the external relative humidity. When the specimens are exposed to low external relative humidity condition, the hydration is inevitably slowed down [171]. The hydration impacts the development of porous network. The better hydration condition gives finer porous network [172, 173]. Since the permeability and isotherm desorption curve are influenced by porous network, it is legitimate to observe variation in fitting results between $RH^e = 30\%$ and $RH^e = 70\%$. In Fig. 4.4 the fitted isotherm desorption curves for both boundary conditions are plotted.

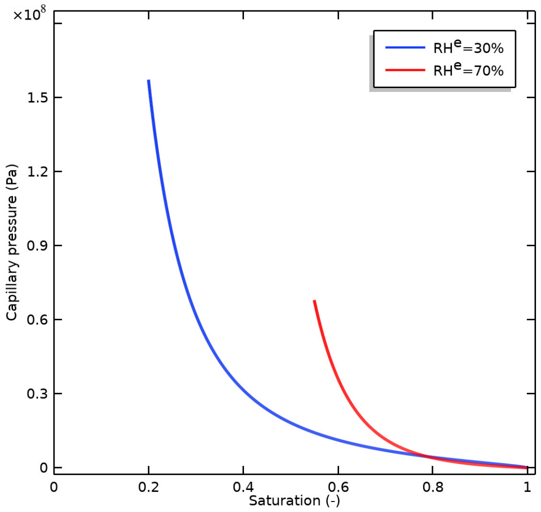

Figure 4.4: Relationship between water saturation and capillary pressure (isotherm desorption curves) for the two boundary conditions

4.5 Discussion on the final results obtained with the standard model

Modelling results of mass loss curves obtained from modelling at boundary conditions $RH^e = 70\%$ and $RH^e = 30\%$ are presented and compared with corresponding experimental data respectively in Fig. 4.5. In general, the fitting results are quite good as the values of the coefficient of determination R^2 for both curves are quite close to 1. The mass loss for the $RH^e = 30\%$ is faster and its curve is far above the one at condition $RH^e = 70\%$. One reason is that the lower external relative humidity induces higher hydraulic gradient on open surface, then resulting in faster evaporation rate. In addition, the low external relative humidity decreases the overall degree of hydration leading to poor chemically and physically restrained water. Thus, more free water is available for drying at low RH^e condition.

Similarly, simulated and measured space average strain results at conditions $RH^e = 70\%$ and $RH^e = 30\%$ are compared in Fig. 4.6. For high external relative humidity, the fitting results are quite good. Even though the result simulated at low external relative humidity shows a slight discrepancy with measured data during the drying procedure, it still provides good agreement with determination coefficient $R^2 = 0.979$. The magnitude of drying shrinkage for condition $RH^e = 30\%$ is far above the one for condition $RH^e = 70\%$. The main reasons behind the phenomenon are explained as following. The hydration is

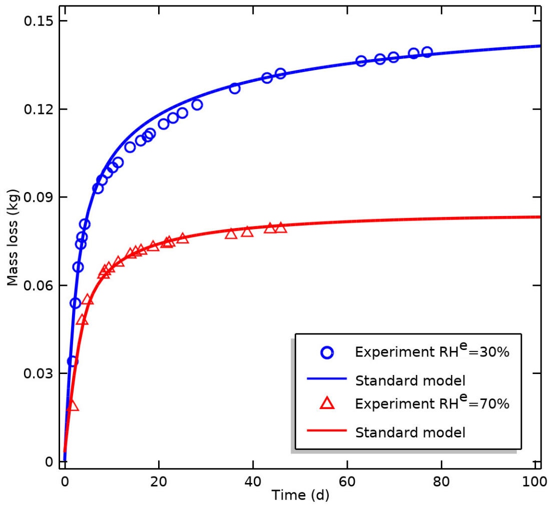

Figure 4.5: Comparisons of mass loss curves simulated by standard modelling with experimental results

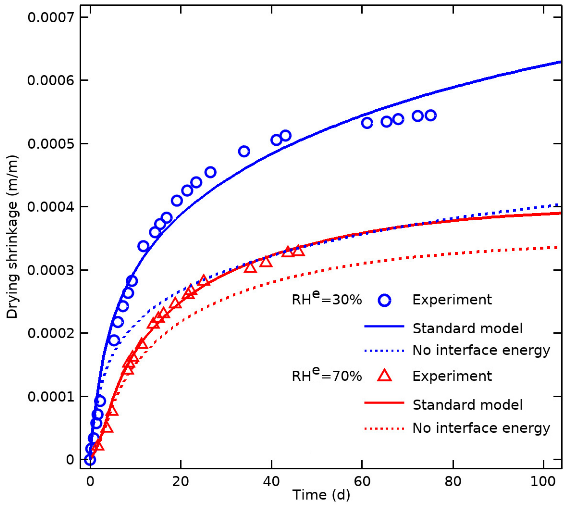

Figure 4.6: Comparisons of space average shrinkage curves simulated by standard and standard without surface energy effects modelings with experimental results

not full when the external relative humidity is too low [171]. It is well-known that not fully hydration causes a drop in Young's modulus. If identical equivalent pore pressure is imposed, the smaller the Young's modulus, the greater the shrinkage occurs. On the other hand, the characteristic of desorption isotherm curve, which is determined by porous network, also affects the evolution of shrinkage. For a given value of capillary pressure, the corresponding water saturation is relative low concerning low ambient relative humidity condition $RH^e = 30\%$ as presented in Fig. 4.4. Indeed, the limited hydration creates coarser porous network resulting in a faster reduction of water saturation. Besides, as supported by

Young-Laplace equation, the smaller pore radius results in larger capillary pressure. Hence, for $RH^e = 30\%$ condition, the water desorption reaches more rapidly in the finer pores leading to larger capillary pressure and interface energy variations, but the water saturation is smaller.

By solving the moisture transport model Eq. (4.5), the spatiotemporal evolution of water saturation is provided for both RH^e conditions. The evolution of capillary pressure, which is related to saturation, can be deduced on the basis of van Genuchten model Eq. (4.3). Then, the internal pore pressures $P_c \cdot S_w$ are obtained by the product of the capillary pressure and the water saturation. The pressures caused by surface energy effects are obtained by Eq. (4.18). The equivalent pore pressure π is equal to the addition of internal pore pressure and interfacial energy pressure. The space average of internal pore pressure and the equivalent pore pressure for these two external conditions are plotted and compared in Fig. 4.7. The curves of internal pore pressure are close for both boundary conditions. For $RH^e = 30\%$, however, the capillary pressure is higher but the degree of saturation is lower, and the opposite for $RH^e = 70\%$. Moreover, as the external relative humidity decreases, the variation between equivalent pore pressure and internal pore pressure increases. A rational explanation is that the contribution of interface energy pressure for equivalent pore pressure at condition $RH^e = 70\%$ is not as great as the one at condition $RH^e = 30\%$. It is consistent with documented literature [158] that the interface energy pressure becomes significant for lower relative humidity. Neglecting the contribution of interface energy pressure for drying shrinkage, the modelling of the shrinkage strain curves is obviously smaller than the measured results (see Fig. 4.6), especially for low RH^e condition.

In general, the standard modelling almost reproduces the experimental evolution of mass loss and drying shrinkage accurately. The above discussions also verify the significant influence of ambient relative humidity on hydration and then on pore network, permeability and desorption isotherm curves. In addition, the contribution of surface energy effects on shrinkage should be appreciated especially for relative low RH^e condition.

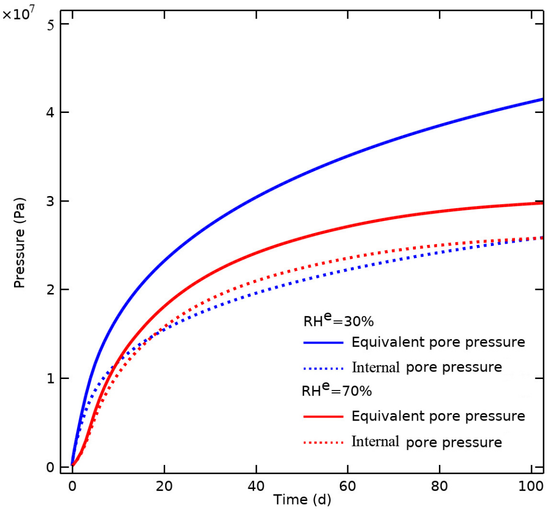

Figure 4.7: Comparison of internal pore pressure with equivalent pore pressure

4.6 Exploration of the dynamic model

4.6.1 Motivation of dynamic model

As mentioned previously, in the standard modelling the fitting results for mass loss kinetics and drying shrinkage at condition $RH^e = 30\%$ are not as good as those at condition $RH^e = 70\%$ (see Fig. 4.5 and 4.6). This phenomenon arouses our suspicions that the standard model may be limited to accurately predict the mass loss and drying shrinkage when high hydric gradient exists between the external environment and the specimen. Furthermore, when the parameters α, m and k, used in standard modelling, are merely adjusted by mass loss fitting, the simulated mass loss kinetics have high agreements with the corresponding measured data for both boundary conditions as presented in Fig. 4.2(a). Theoretically, as for a good governing model, these calibrated parameters could also give good fitting results for the shrinkage strain too. However, it is only available for condition $RH^e = 70\%$. As for condition $RH^e = 30\%$, when these parameters calibrated from mass loss fitting are used to calculate the deformation, the shrinkage modelling curve is far below the measured one (see Fig. 4.2(b)). Significant discrepancy indicated as light blue area is observed. Thus, when the inverse analysis method is used to validate a drying shrinkage model, both of moisture transport and drying shrinkage have to be verified. To the authors' best knowledge, the underestimation of strain for low RH^e condition may be due to the neglect of dynamic capillarity effect. According to Eq. (4.26), the increased capillary pressure could result in additional shrinkage. It inspires us to use the dynamic model to reproduce the drying shrinkage at condition $RH^e = 30\%$.

4.6.2 Determination of the parameters of the dynamic model

The existing studies on dynamic effects are relevant to quite permeable porous media, such as sand and soil. It is significant to extend the dynamic effects studies to cement-based materials with low permeability. In order to implement the dynamic model to simulate the drying procedure for condition $RH^e = 30\%$, dynamic coefficient should be determined. The dynamic coefficient τ is generally formulated as a function of liquid water saturation. Considerable attention has been paid to the dependency of this coefficient τ on the saturation. Simple equations, such as exponential law and power law, were used. However, they are empirically based. A deliberate method is proposed. No specific form of τ-S_w relationship is assigned since a given form eliminates other possibilities. The τ is indirectly determined to provide the modeled space average shrinkage equal to the measured one. The detailed fitting method is presented as following.

First, we give the possible relationship between dynamic and static capillary pressure. For the same mechanical properties, the drying shrinkage is almost proportional to capillary pressure according to Eq. (4.26). It prompts us to adopt the ratio between shrinkage curves to indicate the ratio of corresponding capillary pressures. For condition $RH^e = 30\%$, the ratio of measured shrinkage strains to the one simulated by standard modelling is obtained and plotted in Fig. 4.8.

A number of possible relationships with the general form $f(t)$ have been used to fit these data points including power law, exponential law and high-order polynomial. The fitting is optimized by applying a least squares Marquardt-Levenberg algorithm. In particular, the exponential function Eq. (4.28) is selected due to its better fit to the ratio data.

$$f(t) = \sum_{i=1}^{N} a_i \cdot e^{b_i \cdot t} + c. \tag{4.28}$$

When N reaches to 2, the determination coefficient R^2 is close to 1 indicating good fitting

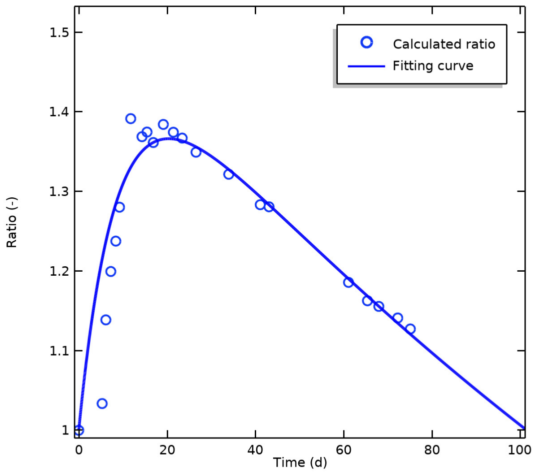

Figure 4.8: Ratio of measured space average shrinkage to the one simulated by standard model

(see Fig. 4.8). However, the above discussion merely gives the potential form of $f(t)$. Further parameter optimization is implemented to improve the fitting of shrinkage strain and mass loss. The fitted parameters are collected in Table 4.5. Until now, the expected relation $P_c^{dyn} = f(t) \cdot P_c$ is obtained.

Table 4.5: Fitting results from inverse analysis of drying shrinkage

Parameters	a_1	a_2	b_1	b_2	c
Fitting value	1.551	4.324×10^{-3}	0.551	-0.114	0.08

Second, the relationship between dynamic coefficient and water saturation is determined. Eq (1) reveals that τ is the slope of the curve when $P_c^{dyn} - P_c$ is plotted versus $\partial S_w/\partial t$. For this calculation, we have to pick up static capillary pressure, dynamic capillary pressure, and the change rate of saturation, all at a given saturation for a definite spatial position. For any given water saturation value corresponding to a certain time, the discrepancy, induced by dynamic effects, between dynamic and static capillary pressure is quantified by $P_c^{dyn} - P_c = (f(t) - 1) \cdot P_c$, where the static capillary pressure is determined by existing $P_c - S_w$ relationship. The corresponding change rate of saturation $\partial S_w/\partial t$ is also available. For any given water saturation, $\partial S_w/\partial t$ and $P_c^{dyn} - P_c$ are substituted in Eq (1). Local-scale values of τ are calculated according to local values of pressures and saturations. While, up-scale values of τ are obtained on the basis of average pressures and saturation values. The resulting local-scale τ of different positions ($r = 1, 2, 3\ cm$) are plotted versus saturation and compared with column-scaled one in Fig. 4.9. In general, τ values increase almost log-linearly as saturation decreases during drying. Similar phenomenon for τ is found in a series of drainage experiments with the same sand type by Zhuang et al. [10]. The magnitudes of the up-scale dynamic coefficients are comparable with the local ones. This is in agreement with the conclusion of Camps-Roach et al. [91] and Bottero et al. [90] from drainage experiments performed in quite permeable materials. It seems that the scale dependency of dynamic coefficient is insignificant. However, the dependency of τ on the scale has been mentioned in numerical studies by Manthey et al. [113] and in a pore scale modelling by Dahle et al. [36]. Consequently, it is also hard to reach a consensus on the scale-dependence of τ for cement-based materials based on only one given SCC mixture. More investigations on various cements, mortars and concretes are needed.

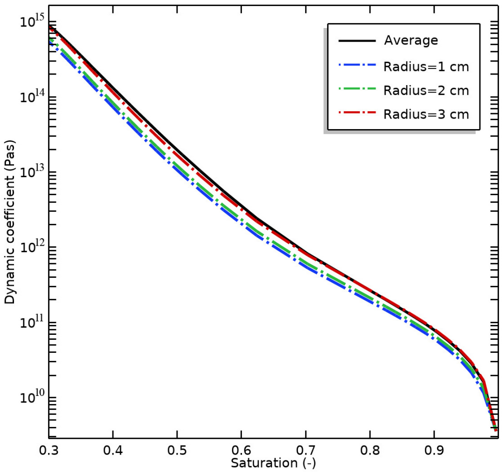

Figure 4.9: Evolution of dynamic coefficient versus saturation

As evident from the previous literature [174], the τ ranges from $3 \times 10^4\ Pa \cdot s$ to 1×10^{10} $Pa \cdot s$ for most soils which are regarded as quite permeable porous media compared with cementitious materials. Stauffer [93] has proposed an empirical equation to calculate τ, which indicates that the value of τ is inversely proportional to the intrinsic permeability. This is also supported experimentally by Camps-Roach et al. [91] who obtain a larger dynamic coefficient for finer sand. Thus, for weakly permeable cement-based material study, τ values are expected to be greater than that of soils. The τ values are found to vary between $0.5 \times 10^{10}\ Pa \cdot s$ and $10^{15}\ Pa \cdot s$ following the expectation.

4.6.3 Results analysis

In Fig. 4.10 the simulated curves obtained from the dynamic modelling at condition $RH^e = 30\%$ are plotted and compared with the experimental measurements.

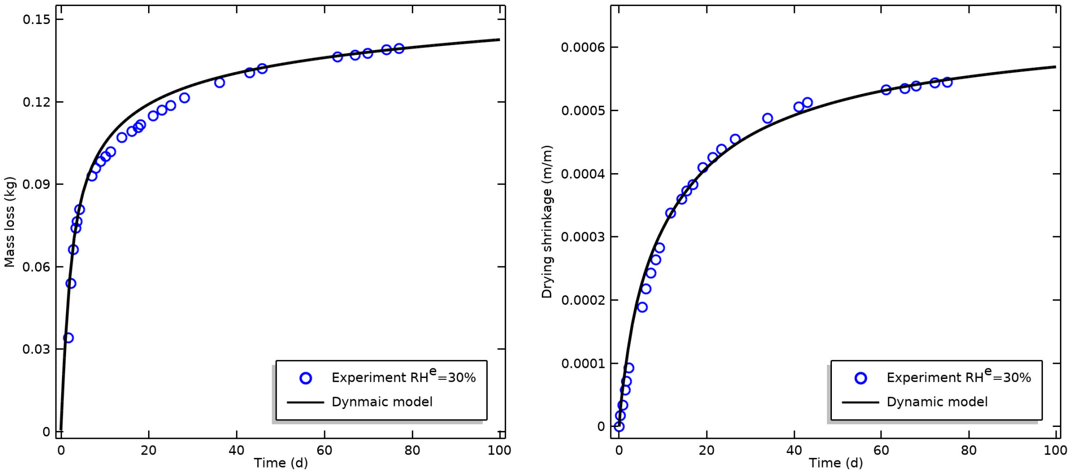

(a) Kinetics of mass loss (b) Space average shrinkage

Figure 4.10: Comparisons of simulation results obtained from dynamic model with experimental results for condition $RH^e = 30\%$

The modelling mass loss (see Fig. 4.10(a)) and shrinkage strains (see Fig. 4.10(b)) merely display a slight discrepancy with the corresponding experimental data. The fitting results are quite good, especially for the shrinkage strains, whose coefficient of determination R^2 even reaches to 0.999. Next, we focus on discussion of shrinkage. Undoubtedly, compared with the case that the parameters α, m and k used in standard modelling are merely adjusted by mass loss fitting (see Fig. 4.2(b), drying at $RH^e = 30\%$), the performance of dynamic model is obviously better. Furthermore, compared with the case that the parameters used in standard modelling are adjusted by mass loss and shrinkage strains fittings, in which the predicted shrinkage strains curves show non-negligible discrepancy (see Fig. 4.6, drying at $RH^e = 30\%$) with a relative lower value of determination coefficient $R^2 = 0.979$, the dynamic model still gives better fitting results. Based on the verification by the experimental data, it can be concluded that dynamic model is apparently more appropriate than standard model to simulate drying shrinkage of cement-based materials under low RH^e conditions. One important reason is that dynamic model could take into account dynamic effects on capillary pressure when high hydric gradient are imposed on specimen.

The specific spatiotemporal evolution of water saturation and shrinkage obtained for dynamic modelling are plotted in Fig. 4.11 and Fig. 4.12 respectively. As presented in Fig. 4.11, the water saturation decreases rapidly at initial stage since there exists a significant hydric gradient between surrounding and specimen. As time goes by, the drying rate decreases gradually. In addition, for a given time, the closer to the open surface of specimen, the more significant the desaturation is. Given the low saturation results in high capillary pressure, which enhances the generation and development of drying shrinkage, the maximum shrinkage always occurs in the vicinity of open surface (see Fig. 4.12). Thus the cracking risk increases there.

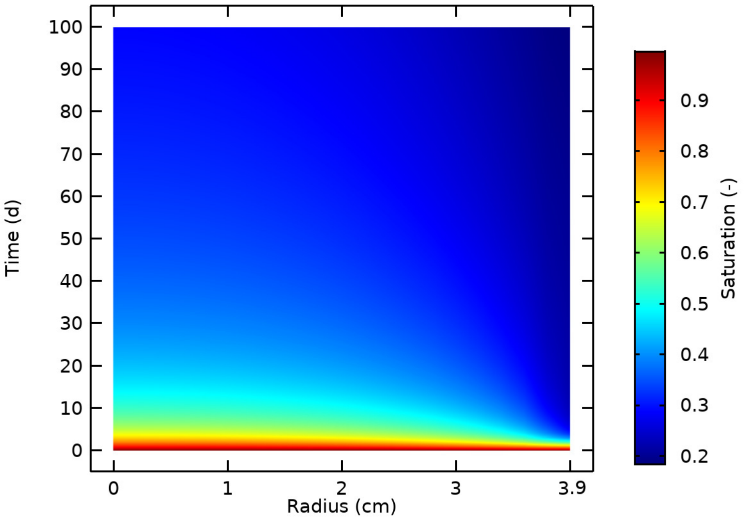

Figure 4.11: Spatiotemporal evolution of the water saturation for dynamic modelling at condition $RH^e = 30\%$

4.7 Concluding remarks

The dynamic model has been used for the drying shrinkage problem of concrete subjected to two external relative humidities 30% and 70%. Based on the experimental verifications and comparisons for different simulation conditions, the conclusions can be drawn as follows:

1) The external relative humidity governs the progress of hydration and then determines the generation of porous network. The parameters of van Genuchten model and transport coefficient are fixed by inverse analysis method to give exact descriptions

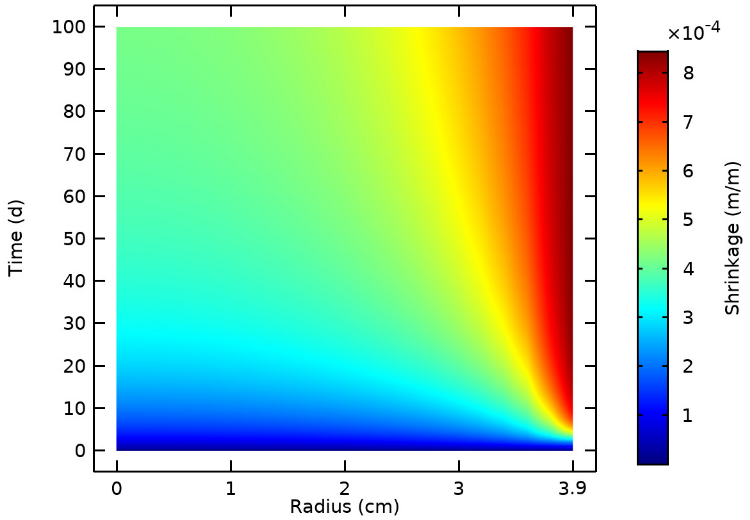

Figure 4.12: Spatiotemporal evolution of the shrinkage for dynamic modelling at condition $RH^e = 30\%$

of experimental mass loss and shrinkage evolutions. The observed variation in fixed parameters of two studied cases proves the significant influence of the hydration-drying coupling. The concrete is an aging viscoelastic material which is continuous in interaction with its ambient relative humidity. The ambient relative humidity mainly determines development of concrete properties especially during the early ages when the hydration has not completed yet.

2) Modelling results obtained from standard model have good agreements with experimental data for high external relative humidity condition $RH^e = 70\%$. However, the fitting results for $RH^e = 30\%$ is not as good as the ones for $RH^e = 70\%$. It indicates that the standard model may be limited to predict the drying shrinkage when high hydric gradient is imposed.

3) Standard model with interface energy considered is more appropriate than the model without taking into account interface energy to simulate the drying shrinkage. The contribution of interfacial energy on equivalent pore pressure is found to significantly increase as the saturation decreases. The pressure induced by interface energy plays important role in generation and development of drying shrinkage, especially for low relative humidity condition.

4) The proposed dynamic model implementing the dynamic capillarity effect into modelling of drying and shrinkage has high applicability. Comparisons with measured

space average strain and mass loss for concrete at condition $RH^e = 30\%$ show that modelling taking dynamic effects into account explicitly provides better results than standard modelling. It is principally because dynamic model can predict a $P_c - S_w$ relation closer to real conditions of the material. Dynamic model could be recommended for modelling of drying shrinkage, especially the surface directly exposed to a low relative humidity condition.

Chapter 5

General conclusions and perspectives

5.1 Conclusions

The main objective of this thesis is to investigate the applicability and validity of dynamic capillarity effect for fluid-solid interaction modeling of unsaturated porous materials. This section highlights the main contributions of this thesis. which are presented in the sequence of chapters.

1) We first present an original mathematical model for the modeling of fast drainage and shrinkage for quite permeable porous materials. The model is on the basis of dynamic capillarity effect theory. The main novelty is that the contribution of dynamic effects is considered not only for the unsaturated water-air flow but also for the generation of solid deformation. The model with and without the dynamic effects on capillary pressure are called'dynamic model' and 'standard model' respectively. Two different models, the standard coupled model and the dynamic coupled model, are employed and compared in terms of their ability to reproduce the experimental data of fast drainage from a sand box. In addition, an inverse analysis method on the basis of Levenberg–Marquardt algorithm is used to investigate the evolution of dynamic pressure coefficient. It is an innovative and deliberate method compared with traditional experiment method. As expected, numerical results, i.e. capillary pressure and average saturation, provided by dynamic model have high agreement

with corresponding experimental data. On the other hand, the standard model without dynamic effects gives results that are at odds with the observations. Moreover, we theoretically prove that the dynamic effects on capillary pressure, which are always neglected with respect to solid deformation, have the potential to cause unexpected destroy. Thus, this coupled model has profound significance for predicting the durability of porous materials.

2) On the basis of the first model, a more advanced model for predicting moisture transport and drying shrinkage of weakly permeable porous materials has been constructed. It implements the dynamic capillarity effect into liquid-water advection, water vapour diffusion and then drying shrinkage of porous body. The proposed model is discretized in space by finite element method and in time by backward Euler method. Both of coupled model with dynamic terms and coupled model without dynamic terms are implemented to simulate a documented drying experiment for cement paste specimens exposed to two different ambient relative humidity conditions. The inverse analysis method mentioned earlier is used again. Experimental data verification on mass loss kinetics indicates that dynamic model provides higher fitting results than the standard model. In addition, the performance of dynamic capillarity effect on moisture transport-solid deformation interaction has been analysed. The comparison of dynamic modeling with non dynamic modeling reveals that dynamic capillarity effect has non-negligible influence on solid deformation and effective permeability. However, the negative effect of solid deformation on moisture transport seems to be neglected in this case. All investigations allow concluding that dynamic effects on capillary pressure should be taken into account to quantify moisture transport for fast drying of cement-based materials.

3) On the basis of the second model, we propose a dynamic drying and shrinkage model for viscoelastic cement-based materials according to thermodynamic principles. The moisture transport model with the consideration dynamic capillarity effect is written as a diffusion form. Compared with the second model, the shrinkage model is optimized by taking into account the contribution of pressure caused by interfacial energy on drying shrinkage. A drying experiment for SCC specimens subjected to two external relative humidities 30% and 70% has been used as a example to verify the

proposed dynamic model. Up to RH^e=70% condition, the traditional standard model predict the mass loss kinetics and space average shrinkage experiments accurately. However, as the RH^e decreases to low value 30%, only dynamic model provide modeling results have good agreements with corresponding experimental data. In addition, we observe that the proportion of interfacial energy in equivalent pore pressure is found to be greater as the saturation continues to decrease. Since equivalent pore pressure is the driving force for shrinkage, the pressure induced by interface energy plays more important role in generation and development of drying shrinkage. Thus, modeling taking dynamic capillarity effect and pressure of interfacial energy into account should be strongly recommended for modeling of drying and shrinkage, especially when open surface directly exposed to a low relative humidity condition.

5.2 Perspectives

Although some efforts have been made on fluid-solid interaction model with the consideration of dynamic capillarity effect for porous materials. More investigations should be implemented to further develop the dynamic model. There are several perspectives, which are suggested for the future research.

1) Taking into account the pressure variation of gas mixture for dynamic moisture transport model. In this thesis, the derivation of dynamic moisture transport model is on the basis of assumption that the pressure of gas mixture in porous materials is constant and equals to atmospheric pressure. It is efficient to deal with the drying and drainage cases studied in this thesis. However, in the case of wetting or drying induced by increasing the gas pressure, these dynamic moisture transport models seems to be limited. In order to improve the applicability of dynamic transport model, it should be further developed by considering the variation of gas mixture pressure.

2) Since hysteresis exists for capillary pressure-water saturation (or relative humidity-water saturation) relationship during wetting and drying cycles, studies are suggested to improve the existing hysteresis models of moisture transport according to the theory and principle of dynamic capillarity effect.

3) Associating the dynamic effects with temperature field is a research interest. Since high temperature not only induces temperature stress filed but also accelerate the water evaporation resulting in fast drying, it may cause stronger dynamic capillarity effect. Additional solid deformation caused by temperature stress field and dynamic capillarity effect increases the cracking risk. Hence, it is significant to corporate dynamic capillarity effect with high temperature field to predict the durability and sustainability of cement-based materials under the heat of fire.

Appendix

Appendices

On the basis of the principle of virtual work and Green's theorem, the weak form of the equilibrium equation (2.32) is given as follows:

$$-\int\limits_{\Omega} \partial\varepsilon^{\mathbf{T}} \cdot \sigma_{ij} \cdot d\Omega + \int\limits_{\Gamma_t} \partial\mathbf{U}^{\mathbf{T}} \cdot \mathbf{t} \cdot d\Gamma + \int\limits_{\Omega} \partial\mathbf{U}^{\mathbf{T}} \cdot \rho \cdot \mathbf{b} d\Omega = 0, \tag{A.1}$$

where $\partial\mathrm{U}$ is arbitrary infinitesimal displacement. $\partial\varepsilon = \mathbf{L} \cdot \partial\mathrm{U}$ is the infinitesimal strain corresponding to $\partial\mathrm{U}$ with $\mathbf{L}$ the differential operator. Γ_t is natural boundary, i.e. the boundary condition is imposed as traction for displacement field: $\mathbf{t} = \sigma_{ij}\mathbf{n}$. Here, the outward unit normal vector to the boundary surface is denoted by $\mathbf{n}$. Moreover, after substitution of effective stress principle and the constitutive relationship into above equation and elimination of the common arbitrary factor $\partial\mathrm{U}^{\mathbf{T}}$ the algebraic form of the governing equation for skeleton deformation is obtained if the following definitions are employed:

$$\mathbf{B} = \mathbf{L} \cdot \mathbf{N}^{\mathbf{u}}, \tag{A.2}$$

$$\mathbf{C_{sw}} = \int\limits_{\Omega} \mathbf{B}^{\mathbf{T}} \cdot b \cdot S_w \cdot \mathbf{m} \cdot \mathbf{N}^{\mathbf{P}} \cdot d\Omega, \tag{A.3}$$

$$\mathbf{C_{dyn}} = \int\limits_{\Omega} \mathbf{B}^{\mathbf{T}} \cdot b \cdot S_w \cdot \tau \frac{\partial S_w}{\partial p_c} \cdot \mathbf{m} \cdot \mathbf{N}^{\mathbf{P}} \cdot d\Omega, \tag{A.4}$$

$$\mathbf{f_u} = \int\limits_{\Omega} \mathbf{N}^{\mathbf{u},\mathbf{T}} \cdot \rho \cdot \mathbf{b} d\Omega + \int\limits_{\Gamma_t} \mathbf{N}^{\mathbf{u},\mathbf{T}} \cdot \mathbf{t} \cdot d\Gamma, \tag{A.5}$$

where $\mathbf{m}$ indicates a vector equivalent to Kronecker δ_{ij}. The following relation exists: $\int\limits_{\Omega} \mathbf{B}^{\mathbf{T}}\sigma' d\Omega = \int\limits_{\Omega} \mathbf{B}^{\mathbf{T}}\mathbf{D}\mathbf{B} d\Omega \mathbf{u} = \mathbf{K}\mathbf{u}$, where $\mathbf{D}$ is the constitutive matrix of the material and $\mathbf{K}$ the global stiffness matrix. On the other hand, in order to implement efficient numerical process, the governing equation for moisture transport (3.18) can be transformed to the following form:

$$-\phi\frac{\partial S_w}{\partial P_c}\cdot\frac{\partial P_w}{\partial t}+\nabla\cdot\left[\left(-\frac{kk_{rw}}{\eta_w}-\frac{M_wM_vD_0fP_v^{dyn}}{\left(RT\rho_w\right)^2}\right)\nabla\left(P_w+\tau\frac{\partial S_w}{\partial t}\right)\right]+S_w\frac{\partial\phi}{\partial t}=0. \tag{A.6}$$

By introducing the finite element approximation $p_w = p_w\left(t\right) = \mathbf{N}^p\mathbf{p_w}\left(t\right)$ and using the Galerkin method, the weak form of moisture transport governing equation is obtained. After application of the Green's theorem and imposition of the boundary conditions, the weak form is given as below:

$$\begin{aligned}
&\int\limits_{\Omega}\mathbf{N^{p,T}}\cdot\left(-\phi\frac{\partial S_w}{\partial P_c}\right)\mathbf{N^p}\\
&+\nabla\mathbf{N^{p,T}}\cdot\left(\frac{kk_{rw}}{\eta_w}+\frac{M_wM_vD_0fP_v^{dyn}}{\left(RT\rho_w\right)^2}\right)\nabla\left(-\tau\frac{\partial S_w}{\partial P_c}\mathbf{N^p}\right)d\Omega\cdot\dot{\mathbf{p}}_\mathbf{w}\\
&+\int\limits_{\Omega}\nabla\mathbf{N^{p,T}}\cdot\left(\frac{kk_{rw}}{\eta_w}+\frac{M_wM_vD_0fP_v^{dyn}}{\left(RT\rho_w\right)^2}\right)\cdot\nabla\mathbf{N^p}d\Omega\cdot\mathbf{p_w}\\
&+\int\limits_{\Omega}\mathbf{N^{p,T}}\cdot S_w\cdot\frac{\partial\phi}{\partial\varepsilon_v}\cdot\mathbf{m^T}\cdot\mathbf{B}\cdot d\Omega\dot{\mathbf{u}}\\
&+\int\limits_{\Gamma}\mathbf{N^{p,T}}\cdot\mathbf{q_\Gamma}d\Gamma=0.
\end{aligned}\tag{A.7}$$

where $\mathbf{q_\Gamma} = \left(-\frac{kk_{rw}}{\eta_w}-\frac{M_wM_vD_0fP_v^{dyn}}{\left(RT\rho_w\right)^2}\right)\cdot\nabla\left(P_w+\tau\frac{\partial S_w}{\partial t}\right)\cdot\mathbf{n}$ is the Neumann boundary conditions on Γ. Thus, the algebraic equation of moisture transport (3.21) in space is obtained as the following definitions are employed:

$$\mathbf{C_{ws}}=\int\limits_{\Omega}\mathbf{N^{p,T}}\cdot S_w\cdot\frac{\partial\phi}{\partial\varepsilon_v}\cdot\mathbf{m^T}\cdot\mathbf{B}\cdot d\Omega, \tag{A.8}$$

$$\mathbf{P_{ww}}=\int\limits_{\Omega}\mathbf{N^{p,T}}\cdot\left(-\phi\frac{\partial S_w}{\partial P_c}\right)\mathbf{N^p}+\nabla\mathbf{N^{p,T}}\cdot\left(\frac{kk_{rw}}{\eta_w}+\frac{M_wM_vD_0fP_v^{dyn}}{\left(RT\rho_w\right)^2}\right)\nabla\left(-\tau\frac{\partial S_w}{\partial P_c}\mathbf{N^p}\right)d\Omega, \tag{A.9}$$

$$\mathbf{H_{ww}}=\int\limits_{\Omega}\nabla\mathbf{N^{p,T}}\cdot\left(\frac{kk_{rw}}{\eta_w}+\frac{M_wM_vD_0fP_v^{dyn}}{\left(RT\rho_w\right)^2}\right)\cdot\nabla\mathbf{N^p}d\Omega, \tag{A.10}$$

$$\mathbf{f_w}=-\int\limits_{\Gamma}\mathbf{N^{p,T}}\cdot\mathbf{q_\Gamma}d\Gamma, \tag{A.11}$$

Finally, the full discretisation in time by considering the Euler implicit scheme allows the algebraic equations (3.20) and (3.21) reach to equations (A.12) and (A.13) respectively:

$$\mathbf{K}\mathbf{u}^{n+1} - \mathbf{C}_{\mathbf{dyn}}^{n+1}\frac{\mathbf{p}_{\mathbf{w}}^{n+1} - \mathbf{p}_{\mathbf{w}}^{n}}{\delta t_n} + \mathbf{C}_{\mathbf{sw}}^{n+1}\mathbf{p}_{\mathbf{w}}^{n+1} = \mathbf{f}_{\mathbf{u}}^{n+1}, \tag{A.12}$$

$$\mathbf{C}_{\mathbf{ws}}^{n+1}\frac{\mathbf{u}^{n+1} - \mathbf{u}^{n}}{\delta t_n} + \mathbf{P}_{\mathbf{ww}}^{n+1}\frac{\mathbf{p}_{\mathbf{w}}^{n+1} - \mathbf{p}_{\mathbf{w}}^{n}}{\delta t_n} + \mathbf{H}_{\mathbf{ww}}^{n+1}\mathbf{p}_{\mathbf{w}}^{n+1} = \mathbf{f}_{\mathbf{w}}^{n+1}, \tag{A.13}$$

where superscript $n+1$ indicates that the nonlinear system is written at time $t_{n+1} = t_n + \delta t_n$ with δt_n the time increment. For given initial conditions $\mathbf{u}^0$ and $\mathbf{p}_{\mathbf{w}}^{\mathbf{0}}$, the solution of the nonlinear system $(\mathbf{p}_{\mathbf{w}}^{n+1}, \mathbf{u}^{n+1})$ is computed for all $n = 0, \cdots, N-1$. This system is solved by Newton-Raphson algorithm.

Résumé étendu en français

1. Motivation

Les matériaux poreux sont constitués d'une matrice solide avec des pores qui peuvent être entièrement ou partiellement remplis de fluides. L'étude de l'écoulement des fluides dans les matériaux poreux déformants est importante pour divers domaines de la science et de l'ingénierie, tels que le génie géotechnique et le génie géophysique, l'ingénierie des structures et l'agriculture. Les matériaux poreux du sable et du sol aux matériaux à base de ciment sont largement utilisés dans la pratique de l'ingénierie. Bien qu'une attention sérieuse ait été accordée pour améliorer notre compréhension du comportement mécanique de l'écoulement de fluide dans les matériaux poreux, le développement de modèles de gouvernance plus physiques et pratiques pour la prédiction de la durabilité est toujours une question ouverte.

Par-ailleurs les matériaux poreux sont toujours soumis à des processus de dégradation biologique, physique ou chimique. En effet, le transport de la molécule d'eau joue un rôle important dans durabilité des matériaux poreux. Par exemple, l'eau liquide peut transporter des ions chlorure, modifier le comportement mécanique, provoquer des dommages par gel-dégel et induire une pression interstitielle négative entraînant un retrait. Afin de fournir une prédiction précise de la durabilité des matériaux poreux, il est très important de comprendre le comportement de l'humidité dans les matériaux poreux et son influence sur la déformation du solide poreux.

Dans cette thèse, nous nous concentrons strictement sur la perte d'humidité et le retrait des matériaux poreux. La perte d'humidité se produit toujours à l'interface des matériaux poreux et de l'environnement lorsque la pression de l'eau aux limites ou l'humidité relative externe diminue. Pour les matériaux à forte perméabilité, ce processus est appelé drainage. Concernant les matériaux à faible perméabilité, on parle de séchage. Lorsque les matériaux poreux deviennent insaturés, la pression capillaire de tension négative apparaît et est imposée sur la paroi des pores. C'est également la force motrice du retrait de séchage et peut augmenter le risque de fissuration et causer des dommages. La pression capillaire est étroitement liée à la saturation en eau, qui est principalement déterminée par le mouvement de l'humidité. Puis le retrait au séchage à son tour a une influence sur le réseau de pores puis sur l'écoulement du fluide. Ainsi, le drainage (séchage) est un phénomène complexe et doit être bien compris.

La modélisation du transport d'humidité et du retrait au séchage des matériaux poreux est étudiée depuis des décennies. La courbe de rétention d'eau donne la relation entre la saturation en eau et la pression capillaire, ce qui est un complément essentiel pour résoudre le problème de transport d'humidité. Cependant, au début, la plupart des modèles de transport d'humidité utilisaient une approche simple, qui adoptait la même courbe de rétention d'eau obtenue à la condition d'équilibre pour le processus de séchage dynamique; ainsi, les effets dynamiques du phénomène physique existant sur la pression capillaire pour un transport rapide de l'humidité ont été négligés. Les effets dynamiques sur la pression capillaire ont été reconnus comme une caractéristique non négligeable du comportement à l'humidité des matériaux poreux, tels que les sables et les sols. Des études récentes ont indiqué que cette approche simplifiée fournit difficilement une prédiction précise et il a été suggéré de prendre en compte les effets dynamiques sur la pression capillaire.

2. Objectifs

À l'échelle microscopique dans les pores, les équations dynamiques du fluide (par exemple Navier-Stokes) sont appliquées pour simuler l'écoulement du fluide. À l'échelle macroscopique, la loi de Darcy est utilisée. Entre ces deux échelles, auxquelles les pores ne sont pas explicitement représentés dans le valcul numérique, mais leur comportement a une influence importante sur le comportement total du milieu poreux, il est suggéré d'ajouter un paramètre dans les équations macroscopiques pour considérer les effets microscopiques dans les pores. De cette manière, le coefficient dynamique, au sens de la dynamique des fluides, est introduit dans l'équation de pression capillaire.

L'objectif global de cette thèse est d'optimiser le modèle d'interaction fluide-solide en tenant compte des effets dynamiques sur la pression capillaire, puis de prédire un comportement plus précis du transport de l'humidité et de la déformation solide pour les matériaux poreux. Dans cette thèse, les modèles avec et sans effets dynamiques sur la pression capillaire sont appelés respectivement modèle dynamique et modèle standard. À cette fin, la thèse se concentrera sur les objectifs spécifiques suivants et un aperçu des modèles utilisés pour divers matériaux poreux est présenté dans la figure below:

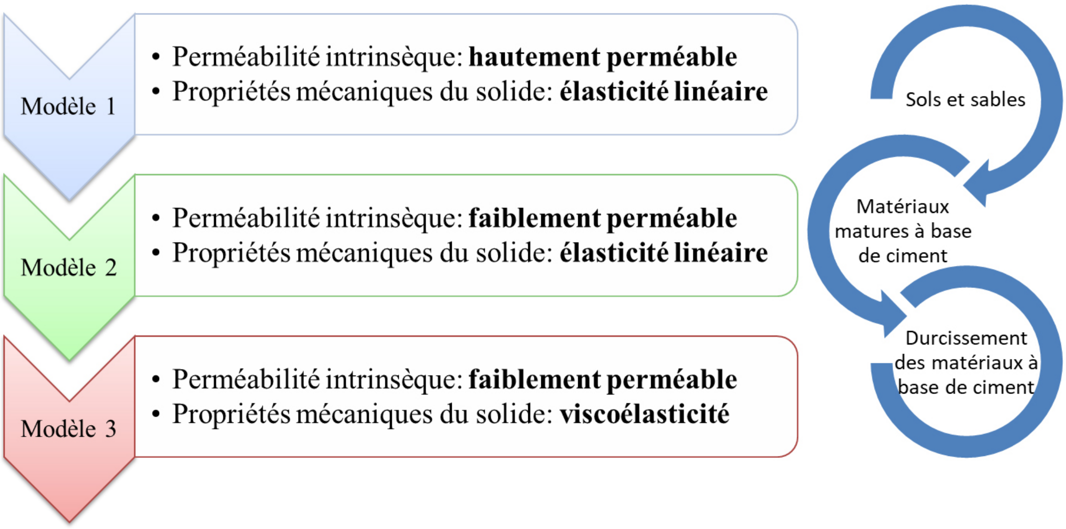

Un aperçu des modèles utilisés pour divers matériaux poreux

Tout d'abord, nous nous concentrons sur le développement de modèles pour les matériaux poreux à perméabilité relativement élevée, tels que le sable et certains types de sol. Étant donné que les études sur les effets dynamiques sur la pression capillaire sont limitées au flux insaturé et que son influence possible sur la déformation des structures poreuses est totalement négligée, il est crucial de construire un modèle couplé entre écoulement eau-air insaturé et déformation pour les matériaux poreux. Dans ce cas, le transport d'humidité ne dépend que de l'advection d'eau et la diffusion de vapeur est totalement négligée.

Deuxièmement, l'effet de capillarité dynamique pour les matériaux poreux faiblement perméables est discuté. Considérant que le transport de l'humidité est plus compliqué pour les matériaux poreux à faible perméabilité, tels que le béton et la pâte de ciment, un modèle de transport d'humidité prenant en compte les effets dynamiques sur la pression capillaire pour l'advection d'eau et la diffusion de vapeur est dérivé et sert ensuite de partie importante pour les modèles d'interaction fluide-solide.

Troisièmement, le milieu poreux faiblement perméable est encore discuté. Mais, le comportement mécanique est supposé être viscoélastique et la déformation solide provoquée par l'énergie interfaciale est également prise en compte. Dans ce cas, les effets dynamiques sur la pression capillaire sont considérés non seulement pour le transport d'humidité, mais également pour la libération d'énergie interfaciale selon la thermodynamique. Ce modèle est applicable pour le durcissement de matériaux à base de ciment exposés à des conditions d'humidité relative ambiante faible.

Cette thèse élabore les objectifs et s'organise de la manière suivante:

Le chapitre 1 passe en revue les théories et les modèles de base du transport de l'humidité et de la déformation solide pour les matériaux poreux. Ensuite, les effets dynamiques sur la pression capillaire sont présentés et expliqués en détail.

Le chapitre 2 présente un modèle entièrement couplé prenant en compte l'effet de capillarité dynamique pour l'écoulement d'eau-air insaturé et le retrait dans des matériaux poreux hautement perméables. Le modèle dynamique est validé par rapport à l'expérience documentée sur l'étude de l'effet de capillarité dynamique dans un échantillon de sable insaturé. Ensuite, d'autres discussions sur l'application de ce modèle dynamique dans la résolution des problèmes d'interaction liquide-solide dans des conditions de drainage rapide sont mises en œuvre.

Le chapitre 3 présente un modèle dynamique avancé pour décrire le transport de l'humidité (consistant en l'advection d'eau et la diffusion de vapeur) et le retrait au séchage d'un matériau à base de ciment à faible perméabilité. Une expérience de séchage d'échantillons de pâte de ciment exposés à différentes conditions d'humidité relative ambiante a été analysée avec des modèles dynamiques et standard pour démontrer que le modèle dynamique peut être appliqué avec succès pour prédire le transport de l'humidité.

Le chapitre 4 développe un modèle dynamique en tenant compte de l'effet de capillarité dynamique et de l'énergie interfaciale pour le retrait au séchage des matériaux viscoélastiques à base de ciment. Une expérience de séchage documentée d'échantillons de béton autocompactant (SCC) est utilisée comme exemple pour vérifier ce modèle dynamique. Les approches de modélisation standard et dynamique sont étudiées par des comparaisons avec des données expérimentales documentées, y compris la perte de masse et le rétrécissement moyen de l'espace pour la vérification.

Enfin, une conclusion générale résume la contribution principale de cette thèse, puis les futures orientations de recherche potentielles sont discutées. Pour plus de clarté, nous redéfinissons les modèles et les équations de champ dans chaque chapitre et nous pouvons considérer que les chapitres sont indépendants.

3. Discussion des résultats

3.1) Nous présentons d'abord un modèle mathématique original pour la modélisation du drainage rapide et du retrait pour des matériaux poreux assez perméables. Le modèle est basé sur la théorie de l'effet de capillarité dynamique. La principale nouveauté est que la contribution des effets dynamiques est considérée non seulement pour le flux eau-air insaturé mais aussi pour la génération de déformation solide. Le modèle avec et sans effets dynamiques sur la pression capillaire est appelé respectivement modèle dynamique et modèle standard. Deux modèles différents, le modèle couplé standard et le modèle couplé dynamique, sont utilisés et comparés en termes de leur capacité à reproduire les données expérimentales de drainage rapide à partir d'un bac à sable. De plus, une méthode d'analyse inverse basée sur l'algorithme de Levenberg – Marquardt est utilisée pour étudier l'évolution du coefficient de pression dynamique. C'est une méthode innovante et délibérée par rapport à la méthode expérimentale traditionnelle. Comme prévu, les résultats numériques, c'est-à-dire la pression capillaire et la saturation moyenne, fournis par le modèle dynamique ont un accord élevé avec les données expérimentales correspondantes. En revanche, le modèle standard sans effets dynamiques donne des résultats en contradiction avec les observations. De plus, nous prouvons théoriquement que les effets dynamiques sur la pression capillaire, qui sont toujours négligés par rapport à la déformation solide, ont le potentiel de provoquer une destruction inattendue. Ainsi, ce modèle couplé a une signification profonde pour prédire la durabilité des matériaux poreux.

3.2) Sur la base du premier modèle, un modèle plus avancé pour prédire le transport de l'humidité et le retrait au séchage des matériaux poreux faiblement perméables a été construit. Il met en œuvre l'effet de capillarité dynamique dans l'advection liquide-eau, la diffusion de vapeur d'eau et ensuite le retrait de séchage du corps poreux.

Le modèle proposé est discrétisé dans l'espace par la méthode des éléments finis et dans le temps par la méthode d'Euler rétrograde. Le modèle couplé avec des termes dynamiques et le modèle couplé sans termes dynamiques sont mis en œuvre pour simuler une expérience de séchage documentée pour des échantillons de pâte de ciment exposés à deux conditions d'humidité relative ambiante différentes. La méthode d'analyse inverse mentionnée précédemment est à nouveau utilisée. La vérification des données expérimentales sur la cinétique de perte de masse indique que le modèle dynamique fournit des résultats d'ajustement plus élevés que le modèle standard. En outre, la performance de l'effet de capillarité dynamique sur l'interaction transport de l'humidité-déformation solide a été analysée. La comparaison de la modélisation dynamique avec la modélisation non dynamique révèle que l'effet de capillarité dynamique a une influence non négligeable sur la déformation solide et la perméabilité effective. Cependant, l'effet négatif de la déformation solide sur le transport de l'humidité semble être négligé dans ce cas. Toutes les études permettent de conclure que les effets dynamiques sur la pression capillaire doivent être pris en compte pour quantifier le transport de l'humidité pour un séchage rapide des matériaux à base de ciment.

3.3) Sur la base du deuxième modèle, nous proposons un modèle dynamique de séchage et de retrait pour les matériaux viscoélastiques à base de ciment selon des principes thermodynamiques. Le modèle de transport d'humidité avec la prise en compte de l'effet de capillarité dynamique est écrit comme une forme de diffusion. Par rapport au deuxième modèle, le modèle de retrait est optimisé en prenant en compte la contribution de la pression provoquée par l'énergie interfaciale sur le retrait au séchage. Une expérience de séchage pour des échantillons de CSC soumis à deux humidités relatives externes 30% et 70% a été utilisée comme exemple pour vérifier le modèle dynamique proposé. Jusqu'à $RH^e = 70\%$ condition, le modèle standard traditionnel prévoit avec précision les expériences de cinétique de perte de masse et de retrait moyen spatial. Cependant, comme le RH^e diminue à une valeur faible de $30\ \%$, seul le modèle dynamique fournit des résultats de modélisation qui ont de bons accords avec les données expérimentales correspondantes. De plus, on observe que la proportion d'énergie interfaciale en pression interstitielle équivalente se révèle plus grande à mesure que la saturation continue de diminuer. Etant donné qu'une pression interstitielle équivalente est la force motrice du retrait, la pression induite par l'énergie d'interface joue un rôle plus important dans la génération et le développement du retrait au séchage. Ainsi, la modélisation prenant en compte l'effet de capillarité dynamique et la pression de l'énergie interfaciale doit être fortement recommandée pour la modélisation du séchage et du retrait, en particulier lorsque la surface ouverte est directement exposée à une condition de faible humidité relative.

4. Conclusion

Le modèle dynamique proposé mettant en œuvre l'effet de capillarité dynamique dans la modélisation du séchage et du retrait a une applicabilité élevée. La modélisation prenant en compte explicitement les effets dynamiques donne de meilleurs résultats que la modélisation standard. C'est principalement parce que le modèle dynamique permet de prédire une relation entre saturation et pression capillaire plus proche des conditions réelles du matériau. Un modèle dynamique pourrait être recommandé pour la modélisation du retrait au séchage, en particulier la surface directement exposée à une condition d'humidité relative faible.

References

[1] J. Bear and Y. Bachmat, *Introduction to modeling of transport phenomena in porous media*, vol. 4. Springer Science & Business Media, 2012.

[2] A. Szymkiewicz, *Modelling water flow in unsaturated porous media: accounting for nonlinear permeability and material heterogeneity*. Springer Science & Business Media, 2012.

[3] R. F. Feldman and P. J. Sereda, "A model for hydrated portland cement paste as deduced from sorption-length change and mechanical properties," *Materials and Structures*, vol. 1, no. 6, pp. 509–520, 1968.

[4] S. Airaksinen, "Role of excipients in moisture sorption and physical stability of solid pharmaceutical formulations," 2005.

[5] F. Benboudjema, *Modélisation des déformations différées du béton sous sollicitations biaxiales. Application aux enceintes de confinement de bâtiments réacteurs des centrales nucléaires*. Thesis, Université de Marne la Vallée, 2002.

[6] Y. Xi, Z. P. Bažant, L. Molina, and H. M. Jennings, "Moisture diffusion in cementitious materials moisture capacity and diffusivity," *Advanced Cement Based Materials*, vol. 1, no. 6, pp. 258–266, 1994.

[7] L. Wu, N. Farzadnia, C. Shi, Z. Zhang, and H. Wang, "Autogenous shrinkage of high performance concrete: A review," *Construction and Building Materials*, vol. 149, pp. 62–75, 2017.

[8] J. H. M. Visser, "Extensile hydraulic fracturing of (saturated) porous materials," 1999.

[9] L. Zhuang, *Advanced theories of water redistribution and infiltration in porous media: Experimental studies and modeling*. Thesis, UU Dept. of Earth Sciences, 2017.

[10] L. Zhuang, S. M. Hassanizadeh, C. Z. Qin, and A. de Waal, "Experimental investigation of hysteretic dynamic capillarity effect in unsaturated flow," *Water*

Resources Research, vol. 53, no. 11, pp. 9078–9088, 2017.

[11] H. Samouh, E. Rozière, and A. Loukili, "Experimental and numerical study of the relative humidity effect on drying shrinkage and cracking of self-consolidating concrete," *Cement and Concrete Research*, vol. 115, pp. 519–529, 2019.

[12] C. De Sa, *Etude hydro-mécanique et thermo-mécanique du béton. Influence des gradients et des incompatibilités de déformation*. Thesis, 2007.

[13] I. Soroka, *Portland cement paste and concrete*. Macmillan International Higher Education, 1979.

[14] U. Angst, B. Elsener, C. K. Larsen, and Ø. Vennesland, "Critical chloride content in reinforced concrete—a review," *Cement and Concrete Research*, vol. 39, no. 12, pp. 1122–1138, 2009.

[15] S. Muthulingam and B. Rao, "Non-uniform corrosion states of rebar in concrete under chloride environment," *Corrosion Science*, vol. 93, pp. 267–282, 2015.

[16] F. Wittmann, "On the action of capillary pressure in fresh concrete," *Cement and Concrete Research*, vol. 6, no. 1, pp. 49–56, 1976.

[17] P. S. Huyakorn, *Computational methods in subsurface flow*. academic press, 2012.

[18] G. Topp, A. Klute, and D. Peters, "Comparison of water content-pressure head data obtained by equilibrium, steady-state, and unsteady-state methods 1," *Soil Science Society of America Journal*, vol. 31, no. 3, pp. 312–314, 1967.

[19] D. Smiles, G. Vachaud, and M. Vauclin, "A test of the uniqueness of the soil moisture characteristic during transient, nonhysteretic flow of water in a rigid soil 1," *Soil Science Society of America Journal*, vol. 35, no. 4, pp. 534–539, 1971.

[20] H. W. Brown, "Capillary pressure investigations," *Journal of Petroleum Technology*, vol. 3, no. 03, pp. 67–74, 1951.

[21] S. M. Hassanizadeh and W. G. Gray, "Thermodynamic basis of capillary pressure in porous media," *Water Resources Research*, vol. 29, no. 10, pp. 3389–3405, 1993.

[22] S. M. Hassanizadeh, M. A. Celia, and H. K. Dahle, "Dynamic effect in the capillary pressure–saturation relationship and its impacts on unsaturated flow," *Vadose Zone Journal*, vol. 1, no. 1, pp. 38–57, 2002.

[23] D. B. Das and M. Mirzaei, "Dynamic effects in capillary pressure relationships for two-phase flow in porous media: Experiments and numerical analyses," *AIChE Journal*, vol. 58, no. 12, pp. 3891–3903, 2012.

[24] R. Fučík, J. Mikyška, T. Sakaki, M. Beneš, and T. H. Illangasekare, “Significance of dynamic effect in capillarity during drainage experiments in layered porous media,” *Vadose Zone Journal*, vol. 9, no. 3, pp. 697–708, 2010.

[25] X. Cao and I. Pop, “Degenerate two-phase porous media flow model with dynamic capillarity,” *Journal of Differential Equations*, vol. 260, no. 3, pp. 2418–2456, 2016.

[26] G. F. Pinder and M. A. Celia, *Subsurface hydrology*. John Wiley & Sons, 2006.

[27] G. De Schutter and L. . Taerwe, “Degree of hydration-based description of mechanical properties of early age concrete,” *Materials and Structures*, vol. 29, no. 6, p. 335, 1996.

[28] M. Mainguy, O. Coussy, and V. Baroghel-Bouny, “Role of air pressure in drying of weakly permeable materials,” *Journal of Engineering Mechanics*, vol. 127, no. 6, pp. 582–592, 2001.

[29] J. Bear and A. H.-D. Cheng, *Modeling groundwater flow and contaminant transport*, vol. 23. Springer Science & Business Media, 2010.

[30] N. Lu and W. J. Likos, *Unsaturated soil mechanics*. Wiley, 2004.

[31] D. Or, J. M. Wraith, and A. Warrick, “Soil water content and water potential relationships,” *Soil physics companion*, vol. 1, pp. 49–84, 2002.

[32] G. F. Pinder and W. G. Gray, *Essentials of multiphase flow and transport in porous media*. John Wiley & Sons, 2008.

[33] M. Kutílek, D. R. Nielsen, *et al.*, *Soil hydrology: texbook for students of soil science, agriculture, forestry, geoecology, hydrology, geomorphology and other related disciplines.* Catena Verlag, 1994.

[34] L. K. Abidoye and D. B. Das, “Scale dependent dynamic capillary pressure effect for two-phase flow in porous media,” *Advances in Water Resources*, vol. 74, pp. 212–230, 2014.

[35] S. Schneider, D. Mallants, and D. Jacques, “Determining hydraulic properties of concrete and mortar by inverse modelling,” *MRS Online Proceedings Library Archive*, vol. 1475, 2012.

[36] H. K. Dahle, M. A. Celia, and S. M. Hassanizadeh, “Bundle-of-tubes model for calculating dynamic effects in the capillary-pressure-saturation relationship,” *Transport in Porous media*, vol. 58, no. 1-2, pp. 5–22, 2005.

[37] V. Baroghel-Bouny, “Water vapour sorption experiments on hardened cementitious

materials: Part i: Essential tool for analysis of hygral behaviour and its relation to pore structure," *Cement and Concrete Research*, vol. 37, no. 3, pp. 414–437, 2007.

[38] R. M. Espinosa and L. Franke, "Inkbottle pore-method: prediction of hygroscopic water content in hardened cement paste at variable climatic conditions," *Cement and Concrete Research*, vol. 36, no. 10, pp. 1954–1968, 2006.

[39] H. Ranaivomanana, J. Verdier, A. Sellier, and X. Bourbon, "Toward a better comprehension and modeling of hysteresis cycles in the water sorption–desorption process for cement based materials," *Cement and Concrete Research*, vol. 41, no. 8, pp. 817–827, 2011.

[40] K. S. Sing, "Reporting physisorption data for gas/solid systems with special reference to the determination of surface area and porosity (recommendations 1984)," *Pure applied chemistry*, vol. 57, no. 4, pp. 603–619, 1985.

[41] I. Langmuir, "The constitution and fundamental properties of solids and liquids. part i. solids," *Journal of the American Chemical Society*, vol. 38, no. 11, pp. 2221–2295, 1916.

[42] S. Brunauer, P. H. Emmett, and E. Teller, "Adsorption of gases in multimolecular layers," *Journal of the American Chemical Society*, vol. 60, no. 2, pp. 309–319, 1938.

[43] R. Dent, "A multilayer theory for gas sorption: Part i: sorption of a single gas," *Textile Research Journal*, vol. 47, no. 2, pp. 145–152, 1977.

[44] A. Kumar, S. Ketel, K. Vance, T. Oey, N. Neithalath, and G. Sant, "Water vapor sorption in cementitious materials—measurement, modeling and interpretation," *Transport in Porous Media*, vol. 103, no. 1, pp. 69–98, 2014.

[45] V. Baroghel-Bouny, M. Thiéry, and X. Wang, "Modelling of isothermal coupled moisture–ion transport in cementitious materials," *Cement and Concrete Research*, vol. 41, no. 8, pp. 828–841, 2011.

[46] V. Baroghel-Bouny, X. Wang, M. Thiery, M. Saillio, and F. Barberon, "Prediction of chloride binding isotherms of cementitious materials by analytical model or numerical inverse analysis," *Cement and Concrete Research*, vol. 42, no. 9, pp. 1207–1224, 2012.

[47] M. Iwamatsu and K. Horii, "Capillary condensation and adhesion of two wetter surfaces," *Journal of colloida interface science*, vol. 182, no. 2, pp. 400–406, 1996.

[48] M. Tuller and D. Or, "Hydraulic conductivity of variably saturated porous media:

Film and corner flow in angular pore space," *Water Resources Research*, vol. 37, no. 5, pp. 1257–1276, 2001.

[49] E. A. Mason, M. EA, and M. AP, "Gas transportin porous media: The dusty-gas model," 1983.

[50] K. Higashi, H. Ito, and J. Oishi, "Surface diffusion phenomena in gaseous diffusion. i. surface diffusion of pure gas," *Nippon Genshiryoku Gakkaishi*, vol. 5, 1963.

[51] E. Buckingham, "Studies on the movement of soil moisture," *US Dept. Agic. Bur. Soils Bull*, vol. 38, 1907.

[52] L. A. Richards, "Capillary conduction of liquids through porous mediums," *Physics*, vol. 1, no. 5, pp. 318–333, 1931.

[53] J. Philip and D. De Vries, "Moisture movement in porous materials under temperature gradients," *Eos, Transactions American Geophysical Union*, vol. 38, no. 2, pp. 222–232, 1957.

[54] Z. Bažant and L. Najjar, "Nonlinear water diffusion in nonsaturated concrete," *Matériaux et Construction*, vol. 5, no. 1, pp. 3–20, 1972.

[55] J.-F. Daian, "Condensation and isothermal water transfer in cement mortar part i—pore size distribution, equilibrium water condensation and imbibition," *Transport in Porous Media*, vol. 3, no. 6, pp. 563–589, 1988.

[56] H. Janssen, B. Blocken, and J. Carmeliet, "Conservative modelling of the moisture and heat transfer in building components under atmospheric excitation," *International Journal of Heat Mass Transfer*, vol. 50, no. 5-6, pp. 1128–1140, 2007.

[57] L.-O. Nilsson, "Long-term moisture transport in high performance concrete," *Materials and Structures*, vol. 35, no. 10, pp. 641–649, 2002.

[58] O. Coussy, *Mechanics and physics of porous solids*. John Wiley & Sons, 2011.

[59] C. Li, K. Li, and Z. Chen, "Numerical analysis of moisture influential depth in concrete during drying-wetting cycles," *Tsinghua Science and Technology*, vol. 13, no. 5, pp. 696–701, 2008.

[60] K. Li, C. Li, and Z. Chen, "Influential depth of moisture transport in concrete subject to drying–wetting cycles," *Cement and Concrete Composites*, vol. 31, no. 10, pp. 693–698, 2009.

[61] O. Coussy, *Poromechanics*. John Wiley & Sons, 2004.

[62] O. Coussy, *Mechanics of porous continua*. Wiley, 1995.

[63] A. Hamami, P. Turcry, and A. Aït-Mokhtar, “Influence of mix proportions on microstructure and gas permeability of cement pastes and mortars,” *Cement and Concrete Research*, vol. 42, no. 2, pp. 490–498, 2012.

[64] H. Loosveldt, Z. Lafhaj, and F. Skoczylas, “Experimental study of gas and liquid permeability of a mortar,” *Cement and Concrete Research*, vol. 32, no. 9, pp. 1357–1363, 2002.

[65] M. Cunningham, “The moisture performance of framed structures—a mathematical model,” *Building and Environment*, vol. 23, no. 2, pp. 123–135, 1988.

[66] H. Janssen and S. Roels, “Qualitative and quantitative assessment of interior moisture buffering by enclosures,” *Energy and Buildings*, vol. 41, no. 4, pp. 382–394, 2009.

[67] H.-J. Steeman, A. Janssens, J. Carmeliet, and M. De Paepe, “Modelling indoor air and hygrothermal wall interaction in building simulation: Comparison between cfd and a well-mixed zonal model,” *Building and Environment*, vol. 44, no. 3, pp. 572–583, 2009.

[68] M. Woloszyn, T. Kalamees, M. O. Abadie, M. Steeman, and A. S. Kalagasidis, “The effect of combining a relative-humidity-sensitive ventilation system with the moisture-buffering capacity of materials on indoor climate and energy efficiency of buildings,” *Building and Environment*, vol. 44, no. 3, pp. 515–524, 2009.

[69] J. Woods, J. Winkler, and D. Christensen, “Evaluation of the effective moisture penetration depth model for estimating moisture buffering in buildings,” report, National Renewable Energy Lab.(NREL), Golden, CO (United States), 2013.

[70] M. J. Cunningham, “Effective penetration depth and effective resistance in moisture transfer,” *Building and Environment*, vol. 27, no. 3, pp. 379–386, 1992.

[71] M. J. Cunningham, “Moisture diffusion due to periodic moisture and temperature boundary conditions—an approximate steady analytical solution with non-constant diffusion coefficients,” *Building and Environment*, vol. 27, no. 3, pp. 367–377, 1992.

[72] M. Wyrzykowski, P. Lura, F. Pesavento, and D. Gawin, “Modeling of internal curing in maturing mortar,” *Cement and Concrete Research*, vol. 41, no. 12, pp. 1349–1356, 2011.

[73] P.-C. Aïtcin and R. J. Flatt, *Science and technology of concrete admixtures*. Woodhead Publishing, 2015.

[74] J. W. Bullard, H. M. Jennings, R. A. Livingston, A. Nonat, G. W. Scherer, J. S.

Schweitzer, K. L. Scrivener, and J. J. Thomas, “Mechanisms of cement hydration,” *Cement and Concrete Research*, vol. 41, no. 12, pp. 1208–1223, 2011.

[75] P. Mounanga, A. Khelidj, A. Loukili, and V. Baroghel-Bouny, “Predicting ca (oh) 2 content and chemical shrinkage of hydrating cement pastes using analytical approach,” *Cement and Concrete Research*, vol. 34, no. 2, pp. 255–265, 2004.

[76] R. K. D. OBE, J. de Brito, R. V. Silva, and C. Q. Lye, *Sustainable construction materials: recycled aggregates*. Woodhead Publishing, 2019.

[77] B. A. Schrefler, C. E. Majorana, G. A. Khoury, and D. Gawin, “Thermo-hydro-mechanical modelling of high performance concrete at high temperatures,” *Engineering Computations*, 2002.

[78] K. Kovler and S. Zhutovsky, “Overview and future trends of shrinkage research,” *Materials and Structures*, vol. 39, no. 9, p. 827, 2006.

[79] C. Ferraris and F. H. Wittmann, “Shrinkage mechanisms of hardened cement paste,” *Cement and Concrete Research*, vol. 17, no. 3, pp. 453–464, 1987.

[80] F. Wittmann, “Surface tension skrinkage and strength of hardened cement paste,” *Materials and Structures*, vol. 1, no. 6, pp. 547–552, 1968.

[81] F. H. Wittmann, *Creep and shrinkage mechanisms*, pp. 129–161. Wiley, New York, 1982.

[82] M. Biot and D. Willis, “The elastic coefficients of the theory of consolidation,” *J. appl. Mech*, vol. 24, pp. 594–601, 1957.

[83] K. Terzaghi, *Theoretical soil mechanics*. Chapman And Hall, Limited.; London, 1951.

[84] A. W. Bishop and G. Blight, “Some aspects of effective stress in saturated and partly saturated soils,” *Geotechnique*, vol. 13, no. 3, pp. 177–197, 1963.

[85] O. Coussy, P. Dangla, T. Lassabatère, and V. Baroghel-Bouny, “The equivalent pore pressure and the swelling and shrinkage of cement-based materials,” *Materials and Structures*, vol. 37, no. 1, pp. 15–20, 2004.

[86] I. Vlahinić, H. M. Jennings, and J. J. Thomas, “A constitutive model for drying of a partially saturated porous material,” *Mechanics of Materials*, vol. 41, no. 3, pp. 319–328, 2009.

[87] C. Hua, P. Acker, and A. Ehrlacher, “Analyses and models of the autogenous shrinkage of hardening cement paste: I. modelling at macroscopic scale,” *Cement*

and Concrete Research, vol. 25, no. 7, pp. 1457–1468, 1995.

[88] Z. C. Grasley and C. K. Leung, "Desiccation shrinkage of cementitious materials as an aging, poroviscoelastic response," *Cement and Concrete Research*, vol. 41, no. 1, pp. 77–89, 2011.

[89] A. Hajibabaee, Z. Grasley, and M. Ley, "Mechanisms of dimensional instability caused by differential drying in wet cured cement paste," *Cement and Concrete Research*, vol. 79, pp. 151–158, 2016.

[90] S. Bottero, S. M. Hassanizadeh, P. Kleingeld, and T. Heimovaara, "Nonequilibrium capillarity effects in two-phase flow through porous media at different scales," *Water Resources Research*, vol. 47, no. 10, 2011.

[91] G. Camps-Roach, D. M. O'Carroll, T. A. Newson, T. Sakaki, and T. H. Illangasekare, "Experimental investigation of dynamic effects in capillary pressure: Grain size dependency and upscaling," *Water Resources Research*, vol. 46, no. 8, 2010.

[92] F.-M. Kalaydjian, "Dynamic capillary pressure curve for water/oil displacement in porous media: Theory vs. experiment," in *SPE Annual Technical Conference and Exhibition*, Society of Petroleum Engineers, 1992.

[93] F. Stauffer, "Time dependence of the relations between capillary pressure, water content and conductivity during drainage of porous media," in *IAHR symposium on scale effects in porous media, Thessaloniki, Greece*, vol. 29, pp. 3–35, 1978.

[94] G. Barenblatt and A. Gil'Man, "Nonequilibrium counterflow capillary impregnation," *Journal of Engineering Physics*, vol. 52, no. 3, pp. 335–339, 1987.

[95] S. M. Hassanizadeh and W. G. Gray, "Mechanics and thermodynamics of multiphase flow in porous media including interphase boundaries," *Advances in Water Resources*, vol. 13, no. 4, pp. 169–186, 1990.

[96] M. Hilpert, "Velocity-dependent capillary pressure in theory for variably-saturated liquid infiltration into porous media," *Geophysical Research Letters*, vol. 39, no. 6, 2012.

[97] A. Y. Beliaev and S. Hassanizadeh, "A theoretical model of hysteresis and dynamic effects in the capillary relation for two-phase flow in porous media," *Transport in Porous Media*, vol. 43, no. 3, pp. 487–510, 2001.

[98] S. P. Friedman, "Dynamic contact angle explanation of flow rate-dependent saturation-pressure relationships during transient liquid flow in unsaturated porous

media," *Journal of adhesion science and technology*, vol. 13, no. 12, pp. 1495–1518, 1999.

[99] D. Weitz, J. Stokes, R. Ball, and A. Kushnick, "Dynamic capillary pressure in porous media: Origin of the viscous-fingering length scale," *Physical review letters*, vol. 59, no. 26, p. 2967, 1987.

[100] G. Barenblatt, T. W. Patzek, and D. Silin, "The mathematical model of nonequilibrium effects in water-oil displacement," *SPE journal*, vol. 8, no. 04, pp. 409–416, 2003.

[101] D. Wildenschild, J. Hopmans, and J. Simunek, "Flow rate dependence of soil hydraulic characteristics," *Soil Science Society of America Journal*, vol. 65, no. 1, pp. 35–48, 2001.

[102] D. Wildenschild, J. Hopmans, M. Rivers, and A. Kent, "Quantitative analysis of flow processes in a sand using synchrotron-based x-ray microtomography," *Vadose Zone Journal*, vol. 4, no. 1, pp. 112–126, 2005.

[103] A. Bourgeat and M. Panfilov, "Effective two-phase flow through highly heterogeneous porous media: Capillary nonequilibrium effects," *Computational Geosciences*, vol. 2, no. 3, pp. 191–215, 1998.

[104] P. M. Adler and H. Brenner, "Multiphase flow in porous media," *Annual review of fluid mechanics*, vol. 20, no. 1, pp. 35–59, 1988.

[105] E. Dussan, "On the spreading of liquids on solid surfaces: static and dynamic contact lines," *Annual Review of Fluid Mechanics*, vol. 11, no. 1, pp. 371–400, 1979.

[106] R. L. Hoffman, "A study of the advancing interface. i. interface shape in liquid—gas systems," *Journal of colloid and interface science*, vol. 50, no. 2, pp. 228–241, 1975.

[107] E. Diamantopoulos and W. Durner, "Dynamic nonequilibrium of water flow in porous media: A review," *Vadose Zone Journal*, vol. 11, no. 3, 2012.

[108] V. Joekar-Niasar and S. Hassanizadeh, "Specific interfacial area: The missing state variable in two-phase flow equations?," *Water Resources Research*, vol. 47, no. 5, 2011.

[109] T. Sakaki, D. M. O'Carroll, and T. H. Illangasekare, "Direct quantification of dynamic effects in capillary pressure for drainage–wetting cycles," *Vadose Zone Journal*, vol. 9, no. 2, pp. 424–437, 2010.

[110] W. Lo, C. Yang, S. Hsu, C. Chen, C. Yeh, and M. Hilpert, "The dynamic response of

the water retention curve in unsaturated soils during drainage to acoustic excitations," *Water Resources Research*, vol. 53, no. 1, pp. 712–725, 2017.

[111] L. Hou, L. Chen, and T. C. Kibbey, "Dynamic capillary effects in a small-volume unsaturated porous medium: Implications of sensor response and gas pressure gradients for understanding system dependencies," *Water Resources Research*, vol. 48, no. 11, 2012.

[112] G. Goel and D. M. O'Carroll, "Experimental investigation of nonequilibrium capillarity effects: Fluid viscosity effects," *Water Resources Research*, vol. 47, no. 9, 2011.

[113] S. Manthey, S. M. Hassanizadeh, and R. Helmig, *Macro-scale dynamic effects in homogeneous and heterogeneous porous media*, pp. 121–145. Springer, 2005.

[114] D. Smith, G. Scherer, and J. Anderson, "Shrinkage during drying of silica gel," *Journal of Non-Crystalline Solids*, vol. 188, no. 3, pp. 191–206, 1995.

[115] E. Holt and M. Leivo, "Cracking risks associated with early age shrinkage," *Cement Concrete Composites*, vol. 26, no. 5, pp. 521–530, 2004.

[116] A. Elzeftawy and R. Mansell, "Hydraulic conductivity calculations for unsaturated steady-state and transient-state flow in sand 1," *Soil Science Society of America Journal*, vol. 39, no. 4, pp. 599–603, 1975.

[117] G. Vachaud, M. Vauclin, and M. Wakil, "A study of the uniqueness of the soil moisture characteristic during desorption by vertical drainage 1," *Soil Science Society of America Journal*, vol. 36, no. 3, pp. 531–532, 1972.

[118] S. M. Hassanizadeh, "Advanced theories of two-phase flow in porous media," *Handbook of porous media*, pp. 47–62, 2015.

[119] K. K. Aligizaki, *Pore structure of cement-based materials: testing, interpretation and requirements*. CRC Press, 2014.

[120] G. Goel, L. K. Abidoye, B. R. Chahar, and D. B. Das, "Scale dependency of dynamic relative permeability–satuartion curves in relation with fluid viscosity and dynamic capillary pressure effect," *Environmental Fluid Mechanics*, vol. 16, no. 5, pp. 945–963, 2016.

[121] C.-Z. Qin, B. Guo, M. Celia, and R. Wu, "Dynamic pore-network modeling of air-water flow through thin porous layers," *Chemical Engineering Science*, 2019.

[122] A. Mikelić, "A global existence result for the equations describing unsaturated flow

in porous media with dynamic capillary pressure," *Journal of Differential Equations*, vol. 248, no. 6, pp. 1561–1577, 2010.

[123] K. Bouadjila, A. Mokrane, A. S. Saad, and M. Saad, "Numerical analysis of a finite volume scheme for two incompressible phase flow with dynamic capillary pressure," *Computers Mathematics with Applications*, vol. 75, no. 10, pp. 3614–3631, 2018.

[124] B. Shahbodagh-Khan, N. Khalili, and G. A. Esgandani, "A numerical model for nonlinear large deformation dynamic analysis of unsaturated porous media including hydraulic hysteresis," *Computers and Geotechnics*, vol. 69, pp. 411–423, 2015.

[125] A. Zhou, S. Wu, J. Li, and D. Sheng, "Including degree of capillary saturation into constitutive modelling of unsaturated soils," *Computers and Geotechnics*, vol. 95, pp. 82–98, 2018.

[126] P. C. Carman, "Permeability of saturated sands, soils and clays," *The Journal of Agricultural Science*, vol. 29, no. 2, pp. 262–273, 1939.

[127] X. Wang and U. Nackenhorst, "A coupled bio-chemo-hydraulic model to predict porosity and permeability reduction during microbially induced calcite precipitation," *Advances in Water Resources*, p. 103563, 2020.

[128] V. Genuchten and M. Th, "A closed-form equation for predicting the hydraulic conductivity of unsaturated soils 1," *Soil science society of America journal*, vol. 44, no. 5, pp. 892–898, 1980.

[129] A. T. Corey, "Mechanic of heterogeneous fluids in porous media," *Soil Science*, vol. 125, no. 5, p. 331, 1978.

[130] M. Peszynska and S.-Y. Yi, "Numerical methods for unsaturated flow with dynamic capillary pressure in heterogeneous porous media," *Numer. Anal. Model*, vol. 5, pp. 126–149, 2008.

[131] H. J. Morel-Seytoux, P. D. Meyer, M. Nachabe, J. Tourna, M. v. Genuchten, and R. J. Lenhard, "Parameter equivalence for the brooks-corey and van genuchten soil characteristics: Preserving the effective capillary drive," *Water Resources Research*, vol. 32, no. 5, pp. 1251–1258, 1996.

[132] C. Berentsen, S. Hassanizadeh, A. Bezuijen, and O. Oung, "Modelling of two-phase flow in porous media including non-equilibrium capillary pressure effects," in *Proceedings of the XVI International Conference on Computational Methods in Water Resources*, pp. 1–11, Tech. Univ. of Denmark Copenhagen, Denmark, 2006.

[133] S. Bottero, *Advances in the theory of capillarity in porous media*. Wöhrmann Print Service, 2009.

[134] P. Zhang, F. Wittmann, M. Haist, H. Müller, P. Vontobel, and T. Zhao, “Water penetration into micro-cracks in reinforced concrete,” *Restoration of Buildings Monuments*, vol. 20, no. 2, pp. 85–94, 2014.

[135] J.-K. Kim and C.-S. Lee, “Prediction of differential drying shrinkage in concrete,” *Cement and Concrete Research*, vol. 28, no. 7, pp. 985–994, 1998.

[136] S. A. Altoubat and D. A. Lange, “Creep, shrinkage, and cracking of restrained concrete at early age,” *ACI Materials Journal*, vol. 98, no. 4, pp. 323–331, 2001.

[137] S. Ghourchian, M. Wyrzykowski, and P. Lura, “A poromechanics model for plastic shrinkage of fresh cementitious materials,” *Cement and Concrete Research*, vol. 109, pp. 120–132, 2018.

[138] F. Grondin, M. Bouasker, P. Mounanga, A. Khelidj, and A. Perronnet, “Physico-chemical deformations of solidifying cementitious systems: multiscale modelling,” *Materials and Structures*, vol. 43, no. 1-2, pp. 151–165, 2010.

[139] Y. Li and J. Li, “Capillary tension theory for prediction of early autogenous shrinkage of self-consolidating concrete,” *Construction and Building Materials*, vol. 53, pp. 511–516, 2014.

[140] J. Carette, F. Benboudjema, G. Nahas, K. Abahri, A. Darquennes, and R. Bennacer, “Concrete drying: effects of boundary conditions and specimen shape,” *Service Life of Cement-Based Materials and Structures*, p. 385, 2016.

[141] Z. Zhang, M. Thiery, and V. Baroghel-Bouny, “Numerical modelling of moisture transfers with hysteresis within cementitious materials: Verification and investigation of the effects of repeated wetting–drying boundary conditions,” *Cement and Concrete Research*, vol. 68, pp. 10–23, 2015.

[142] R. Day and J. Illston, “The effect of rate of drying on the drying/wetting behaviour of hardened cement paste,” *Cement and Concrete Research*, vol. 13, no. 1, pp. 7–17, 1983.

[143] R. Helmig, A. Weiss, and B. I. Wohlmuth, “Dynamic capillary effects in heterogeneous porous media,” *Computational Geosciences*, vol. 11, no. 3, pp. 261–274, 2007.

[144] J. Carmeliet and S. Roels, “Determination of the isothermal moisture transport

properties of porous building materials," *Journal of Thermal Envelope Building Science*, vol. 24, no. 3, pp. 183–210, 2001.

[145] M. A. Celia, E. T. Bouloutas, and R. L. Zarba, "A general mass-conservative numerical solution for the unsaturated flow equation," *Water Resources Research*, vol. 26, no. 7, pp. 1483–1496, 1990.

[146] J.-F. Daian, "Condensation and isothermal water transfer in cement mortar: Part ii-transient condensation of water vapor," *Transport in Porous Media*, vol. 4, no. 1, pp. 1–16, 1989.

[147] H. Samouh, E. Rozière, and A. Loukili, "The differential drying shrinkage effect on the concrete surface damage: Experimental and numerical study," *Cement and Concrete Research*, vol. 102, pp. 212–224, 2017.

[148] J. Carette, F. Soleilhet, F. Benboudjema, X. Ma, G. Nahas, K. Abahri, A. Darquennes, and R. Bennacer, "Identifying the mechanisms of concrete drying: An experimental-numerical approach," *Construction and Building Materials*, vol. 230, p. 117001, 2020.

[149] X. Ma, J. Carette, F. Benboudjema, and R. Bennacer, "Optimization of experiment methodology based on identification of parameters in concrete drying," *Construction and Building Materials*, vol. 256, p. 119421, 2020.

[150] Z. Zhang, M. Thiéry, and V. Baroghel-Bouny, "Analysis of moisture transport in cementitious materials and modelling of drying-wetting cycles," in *International Conference: Numerical Modeling Strategies for Sustainable Concrete Structures* (T. F. A. o. C. E. (AFGC), ed.), The French Association of Civil Engineering (AFGC), 2012.

[151] Z. Zhang, M. Thiery, and V. Baroghel-Bouny, "Investigation of moisture transport properties of cementitious materials," *Cement and Concrete Research*, vol. 89, pp. 257–268, 2016.

[152] B. Bary and A. Sellier, "Coupled moisture—carbon dioxide–calcium transfer model for carbonation of concrete," *Cement and Concrete Research*, vol. 34, no. 10, pp. 1859–1872, 2004.

[153] R. Millington, "Gas diffusion in porous media," *Science*, vol. 130, no. 3367, pp. 100–102, 1959.

[154] M. Thiery, V. Baroghel-Bouny, N. Bourneton, G. Villain, and C. Stéfani,

"Modélisation du séchage des bétons: analyse des différents modes de transfert hydrique," *Revue européenne de génie civil*, vol. 11, no. 5, pp. 541–577, 2007.

[155] H. Ranaivomanana, J. Verdier, A. Sellier, and X. Bourbon, "Prediction of relative permeabilities and water vapor diffusion reduction factor for cement-based materials," *Cement and Concrete Research*, vol. 48, pp. 53–63, 2013.

[156] S. Zamani, R. Kowalczyk, and P. McDonald, "The relative humidity dependence of the permeability of cement paste measured using garfield nmr profiling," *Cement and Concrete Research*, vol. 57, pp. 88–94, 2014.

[157] S. Dal Pont, F. Meftah, and B. Schrefler, "Modeling concrete under severe conditions as a multiphase material," *Nuclear Engineering Design*, vol. 241, no. 3, pp. 562–572, 2011.

[158] M. Azenha, K. Maekawa, T. Ishida, and R. Faria, "Drying induced moisture losses from mortar to the environment. part ii: numerical implementation," *Materials and Structures*, vol. 40, no. 8, pp. 813–825, 2007.

[159] M. D. Nguyen, *Modélisation des couplages entre hydratation et dessiccation des matériaux cimentaires à l'issue du décoffrage*. Thesis, 2009.

[160] C.-J. Haecker, E. Garboczi, J. Bullard, R. Bohn, Z. Sun, S. Shah, and T. Voigt, "Modeling the linear elastic properties of portland cement paste," *Cement and Concrete Research*, vol. 35, no. 10, pp. 1948–1960, 2005.

[161] M. Mirzaei and D. B. Das, "Dynamic effects in capillary pressure–saturations relationships for two-phase flow in 3d porous media: Implications of micro-heterogeneities," *Chemical engineering science*, vol. 62, no. 7, pp. 1927–1947, 2007.

[162] Z. Bažant, "Thermodynamics of hindered adsorption and its implications for hardened cement paste and concrete," *Cement and Concrete Research*, vol. 2, no. 1, pp. 1–16, 1972.

[163] R. Jaafri, H. Samouh, E. Roziere, S. Y. Alam, V. Wisniewski, and A. Loukili, "Experimental and numerical analysis of curling behavior of natural hydraulic lime-cement based mortars," *Cement and Concrete Research*, vol. 117, pp. 1–15, 2019.

[164] F. Benboudjema, F. Meftah, and J.-M. Torrenti, "Interaction between drying, shrinkage, creep and cracking phenomena in concrete," *Engineering structures*, vol. 27, no. 2, pp. 239–250, 2005.

[165] Z. Zhang, M. Thiéry, and V. Baroghel-Bouny, "A review and statistical study

of existing hysteresis models for cementitious materials," *Cement and Concrete Research*, vol. 57, pp. 44–60, 2014.

[166] V. Baroghel-Bouny, "Water vapour sorption experiments on hardened cementitious materials. part ii: Essential tool for assessment of transport properties and for durability prediction," *Cement and Concrete Research*, vol. 37, no. 3, pp. 438–454, 2007.

[167] P. K. Mehta and P. J. Monteiro, *Concrete microstructure, properties and materials*. 2017.

[168] V. Baroghel-Bouny and J. Godin, "Experimental study on drying shrinkage of ordinary and high-performance cementitious materials," in *Pro 17: International Rilem Workshop on Shrinkage of Concrete*, pp. 215–232, 2000.

[169] H. Samouh, E. Rozière, V. Wisniewski, and A. Loukili, "Consequences of longer sealed curing on drying shrinkage, cracking and carbonation of concrete," *Cement and Concrete Research*, vol. 95, pp. 117–131, 2017.

[170] M. Thiery, P. Belin, V. Baroghel-Bouny, and M. D. Nguyen, "Modeling of isothermal drying process in cementitious materials: analysis of the moisture transfer and proposal of simplified approaches," in *Thermo-Hydromechanical and Chemical Coupling in Geomaterials and Applications: Proceedings of the 3rd International Symposium GeoProc'2008*, pp. 571–579, Wiley Online Library, 2013.

[171] A. Loukili, A. Khelidj, and P. Richard, "Hydration kinetics, change of relative humidity, and autogenous shrinkage of ultra-high-strength concrete," *Cement and Concrete Research*, vol. 29, no. 4, pp. 577–584, 1999.

[172] A. Darquennes, E. Roziere, M. Khokhar, P. Turcry, A. Loukili, and F. Grondin, "Long-term deformations and cracking risk of concrete with high content of mineral additions," *Materials and Structures*, vol. 45, no. 11, pp. 1705–1716, 2012.

[173] L. Granger, J.-M. Torrenti, and P. Acker, "Thoughts about drying shrinkage: Scale effects and modelling," *Materials and Structures*, vol. 30, no. 2, p. 96, 1997.

[174] M. Mirzaei and D. B. Das, "Dynamic effects in capillary pressure–saturations relationships for two-phase flow in 3d porous media: Implications of micro-heterogeneities," *Chemical Engineering Science*, vol. 62, no. 7, pp. 1927–1947, 2007.

Titre : Modélisation des effets dynamiques en pression capillaire en couplage avec déformation sur la dessiccation des matériaux poreux

Mots clés : Effets dynamiques; Pression capillaire; Mécanique poreuse; Simulation numérique

Résumé : La durabilité des infrastructures constituées de matériaux poreux, tels que le sol, le sable et les matériaux cimentaires, est étroitement liée aux conditions environnementales. La plupart des mécanismes de détérioration sont régis par l'état d'humidité des matériaux poreux. En effet, l'état d'humidité détermine la répartition de la pression capillaire qui est une force importante pour la déformation solide et pourrait augmenter le risque de fissuration. Cependant, la plupart des modèles d'interaction fluide-solide utilisés pour prédire le transport de l'humidité et de la déformation solide ont ignoré le phénomène physique existant, qui est les effets dynamiques sur la pression capillaire. Cette thèse vise à améliorer le modèle d'interaction fluide-solide avec la prise en compte de cet effet de capillarité dynamique. Trois modèles dynamiques correspondant à différents types de matériaux poreux ont été développés. Le premier modèle est disponible pour les matériaux poreux à perméabilité relativement élevée, tels que le sable et le sol. Le deuxième modèle est utilisé pour les matériaux à base de ciments matures à faible perméabilité. Le troisième modèle est développé pour les matériaux cimentaires durcissant exposés à des conditions d'humidité relative extrêmement faibles. Chaque modèle dynamique, et le modèle non dynamique correspondant, ont été utilisés pour simuler des expériences de séchage (drainage) documentées pour le sable, la pâte de ciment mature et le béton durcissant, respectivement. En comparant avec des données expérimentales, les simulations numériques montrent que la modélisation avec effets dynamiques donne de meilleurs résultats que la modélisation non dynamique. Toutes les comparaisons et investigations ont renforcé la nécessité de considérer l'effet de la capillarité dynamique pour prédire le transport d'humidité et la déformation solide pour un séchage rapide (drainage) des matériaux poreux.

Title : Modelling of the dynamic effects in capillary pressure in coupling with deformation on the desiccation of porous materials

Keywords : Dynamic effects; Capillary pressure; Porous mechanics; Numerical simulation

Abstract : The durability of infrastructure made of porous materials such as soil, sand and cement-based materials is closely related to the environmental conditions. Most of the mechanisms of deterioration are governed by moisture state in porous materials. Indeed, the moisture state determines the distribution of capillary pressure which is an important driving force for solid deformation and could increase cracking risk. However, most of fluid-solid interaction models used to predict moisture transport and solid deformation have ignored the existing physical phenomenon dynamic effects on capillary pressure. This thesis aims to refine the fluid-solid interaction model with the consideration of this dynamic capillarity effect. Three dynamic models corresponding to various types of porous materials have been developed. The first model is available for porous materials with relative high permeability such as sand and soil. The second model is used for mature cement-based materials with low permeability. The third model is developed for hardening cement-based materials exposed to extremely low relative humidity condition. Each dynamic model and corresponding non-dynamic model have been implemented to simulate documented drying (drainage) experiments for sand, mature cement paste and hardening concrete, respectively. Compared with experimental data, the numerical simulations show that modeling with dynamic effects gives better results than non-dynamic modeling. All comparisons and investigations enhanced the necessity of considering dynamic capillarity effect to predict the moisture transport and solid deformation for fast drying (drainage) of porous materials.